SC

THE SCINTILLATING FIBER OPTICS DETECTOR AND ITS APPLICATION

THESIS SUBMITTED TO

THE SCHOOL OF GRADUATE STUDIES

IN PARTIAL FULFILLMENT OF THE REQUIREMENTS

FOR THE DEGREE OF

PH.D. IN PHYSICS

By

Saad Naji Faik

University of Ottawa

ISBN 0-315-53780-9

To Joce

Introduction

In the seventies, the discovery of charm and beauty particles with lifetimes in the range of 10^{-12}–10^{-13} s opened the field for new types of detectors oriented toward vertex detection. To search for charm or beauty-particle decays, produced by interactions of high energy hadrons, a high resolution detector is needed. The popular detectors at that time were: the bubble chamber, the multiwire proportional chamber (MWPC), and the spark chamber [1]. None of these detectors could localize an event to better than $\sim$ 1 mm and therefore could not resolve the charm particle decay.

As nuclear emulsion is the highest resolution detector for observing very short lifetimes (down to 10^{-15} s), an electronic detection system is needed to select events, locate them within the emulsion and provide information about decay products. In 1981 we pursued the idea of building such detector. It was very difficult to satisfy the above criteria with the technology available at that time. Drift chambers, for example, fell short of the position resolution required for beam tagging and charm and beauty decay vertex resolution by approximately a factor of 10. Even worse, they could not achieve track pair resolution better than about 2 mm, so that tracks more closely spaced than this are indistinguishable. Since projected angles between tracks of $\leq$1.0 mrad occur with appreciable probability in hadron interactions of 350 to 800 Gev, it is impossible to place drift chambers close to the emulsion target without incurring unacceptable reconstruction losses. Yet high resolution detectors

close to the emulsion target are essential if secondary vertices are to be reconsructed.

Two main approaches were considered. The first was a silicon microstrip vertex detector ([2–5] and references therein). The second was a fine grained hodoscope formed from thin sheets of fast scintillating material such as NE102. Since, at that time, the development of the silicon strip detector was at least one order of magnitude more expensive than the scintillating detector, we opted for the second type of detector . Detailed studies of thin film plastic scintillators with respect to detection efficiency and energy resolution, indicated the possibility of constructing a thin film detector that meets the requirements of sensitivity and spatial resolution.

The detector developed consisted of thin scintillating strips, coupled to an imaging device and silicon diode arrays. It was tested in an experiment at the Lawrence Berkeley Laboratory using Ar^{40} beam with 1.8 Gev/nucleon, on an emulsion target. The aim of the experiment was to study the performance of the detector in reconstructing the events of interactions and localizing its vertices within the target. A series of mishaps, during the course of the experiment, affected the outcome. Although we had an excellent exposure in the emulsion, the test failed to show the actual performance of the detector within normal working conditions.

The rapid progress in manufacturing coherent fiber optics and associated optoelectronics technology, renewed our interest in appling scintillating fiber technology to the problem of charged particle tracking and electromagnetic calorimetry. They offer an attractive way of constructing a compact position detector with good track reconstruction efficiency and adequate spatial resolution.

Although plastic fibers feature fast fluorescence time and high quantum efficiency, they can not be drawn into small fibers. Therefore, they are mainly used in calorimeters and large tracking chambers. On the other hand glass fibers have the advantage of being able to be drawn into very fine segments which makes them suitable for constructing micro-vertex detectors. To date, cerium doped glass is the

most commonly used among the scintillating glass fibers because of its fast response time (~100 ns). Its main disadvantage is the poor quantum efficiency caused by the internal absorption of the emitted light within the fibers. Alternatively, terbium doped glass has better quantum efficiency but it has a long decay time (3–5 ms).

We were fortunate enough to get some help from industry which are interested in our work. Their expertise and financial support enabled us to construct a portable and flexible prototype of a scintillating fiber optics detector which could have interesting application near accelerators in studying beam topology. The prototype consisted of thin wafers of terbium-doped scintillating glass fibers, coupled to a double-stage imaging system and to a CCD video camera. The detector was tested at TRIUMF with a 400 Mev/c pion beam in order to find its optimum working conditions and to establish the feasibility of using it as a vertex detector, or as a tracking system. The results show a high detection efficiency for minimum ionizing particles and adequate spatial resolution that makes the detector suitable for particle tracking and vertex detection.

In a test run experiment at Brookhaven National Laboratory, the detector was used to study the interactions of O^{16} nuclei with thin targets of aluminum, copper, and iron at 14.6 Gev/nucleon. Also, the mean free path and the interaction cross-section in each target was measured. The main advantage of the detector was the instantaneous visual images of the beam particles and their interactions with the different targets and within the detector itself. The results indicate that the detector can be used as a tracking system and as an active target in fixed target experiments with low interaction rates.

Acknowledgements

I would like to sincerely thank my supervisor, Prof. Jacques Hebert, for his guidance and generosity throughout the course of this thesis.

I wish to thank Schott Fiber Optics for supplying us with many samples of the scintillating fibers, and Mr. Stan Patten for for the helpful discussions about the MCP devices.

I also want to thank Dr. G. Krebs and Dr. F. Lothrop for their assistance at Berkeley, Dr. Y. Blackmore and Mr. D. Ottawell for the great help and assistance at TRIUMF, Dr. D. Beavis for his help at Brookhaven.

I would like to acknowledge several other persons for useful discussions, including Dr. C. J. D. Hebert, Dr. P. Bernard, and Dr. C. Fortier.

I wish to thank Mr. B. Hart and the staff of the physics workshop for the lengthy work spent on building the different parts of the detector. The financial support of I. P. P. is gratefully acknowledged.

Contents

List of Tables

List of Figures

Chapter 1

Multistrip Scintillating Detector

1.1 Introduction

The invention of the detector based on a thin scintillating foil (the thin film detector) [6] was of interest to experimental physicists around the mid seventies. The device proved to be very useful for registering the tracks of the heavy charged particles. Its most interesting feature is the thickness (50–100 microns), which is one or two orders of magnitude smaller than in the case of the available silicon dE/dX detector.It is also characterized by fast time response, good signal-to-noise ratio, and simplicity of fabrication. Although it suffers from poor energy resolution, the results of some experiments [7,8] indicated the possibility of achieving an output pulse proportional to the energy loss ΔE in the thin scintillating foil. This was attributed to the unusually smooth surface of the scintillator and/or to the properties of the photomultiplier tube. These results become even more interesting if we consider the fact that crystals of typical size and crystals of several cubic millimeters give approximately the same decrease of the overall energy resolution of the scintillating counter (the intrinsic energy resolution of the scintillator) [9], which is confirmed to be present in the case of plastic scintillator [10].

To study the heavy particles production and decay in high energy interactions , a high resolution detector is needed to select events, locate their vertices, and provide information about decay products. Based on the previous studies of thin foil detectors and taking into consideration the different characteristics of thin plastic scintillators, it is hoped that a thin-film detector constructed from thin scintillator strips will meet with the demands for a fast, efficient, and high resolution detector.

1.2 Characteristics and performance

The previous studies on thin scintillating foils included tests on its timing properties [11-16] and on its response to different particles [6,7,17,18]. Our experiment included tests done on different thicknesses and sizes of NE102 plastic scintillator in order to study its properties and to establish the correct way to build a thin film detector.

1.2.1 Uniformity of the signal across the scintillator

To find the uniformity of the signal produced by particles striking the scintillator in various places, the set-up and the coordinate system shown in figure (1) were used. In order to obtain an accurate measurement for the position of the radioactive source (Sr^{90} of 1 μCu) with respect to the scintillator , the source was mounted on a microscope stage with an **x-y** movement.

Figure(2) shows the counting rate as a function of **x** (across the scintillator) for a 425 microns sheet of area $(4.6 \times 5)cm^2$; the curves drawn show the counting rate expected if the sensitivity of the scintillator is constant all the way out to the edge. Instead of dropping off suddenly at the edges, the counting rate is expected to fall off as shown due to the finite size of the source. The plateau level is determined by

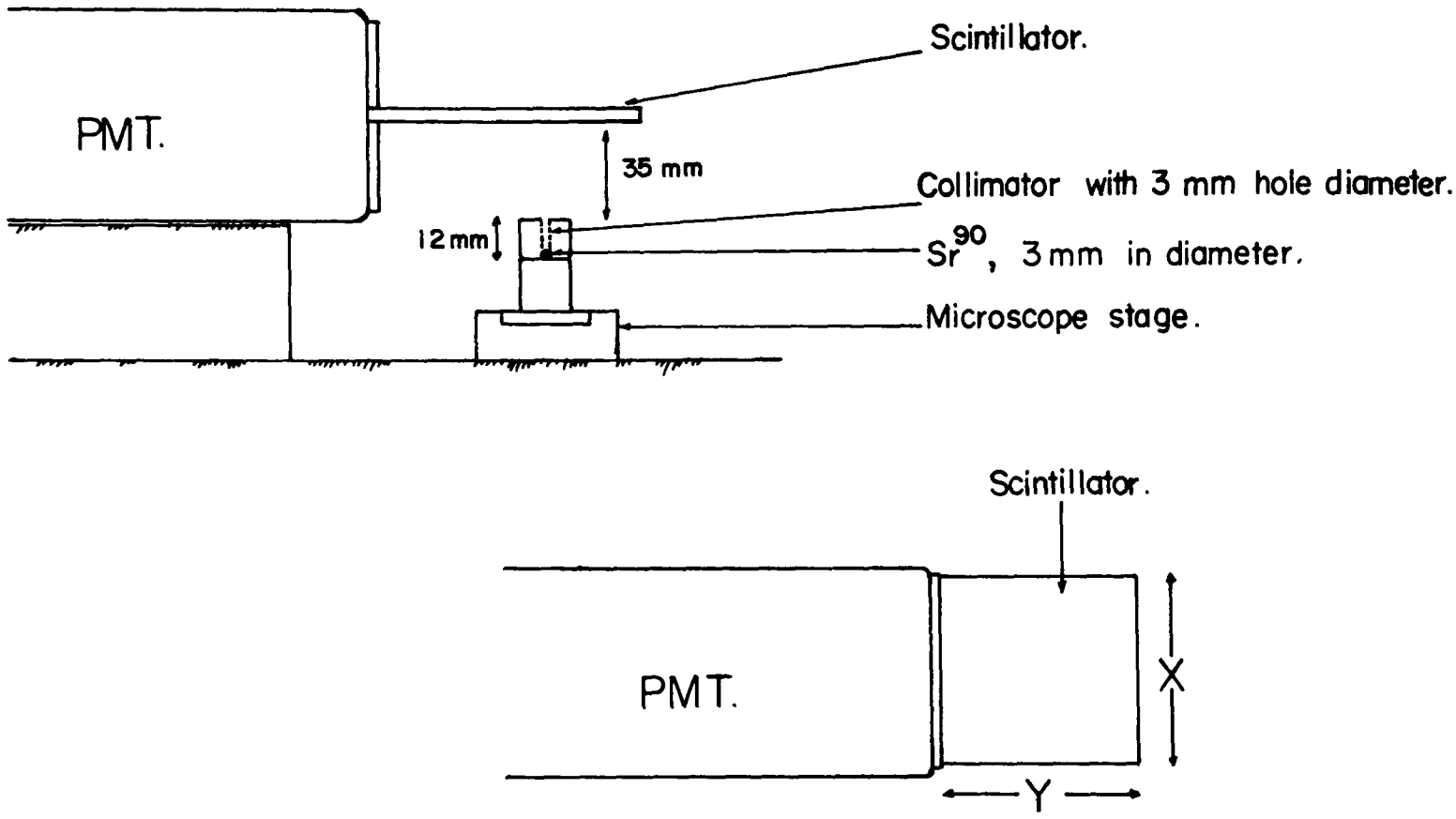

FIGURE (1)

The set-up used to measure the uniformity of the signals across the thin scintillator.

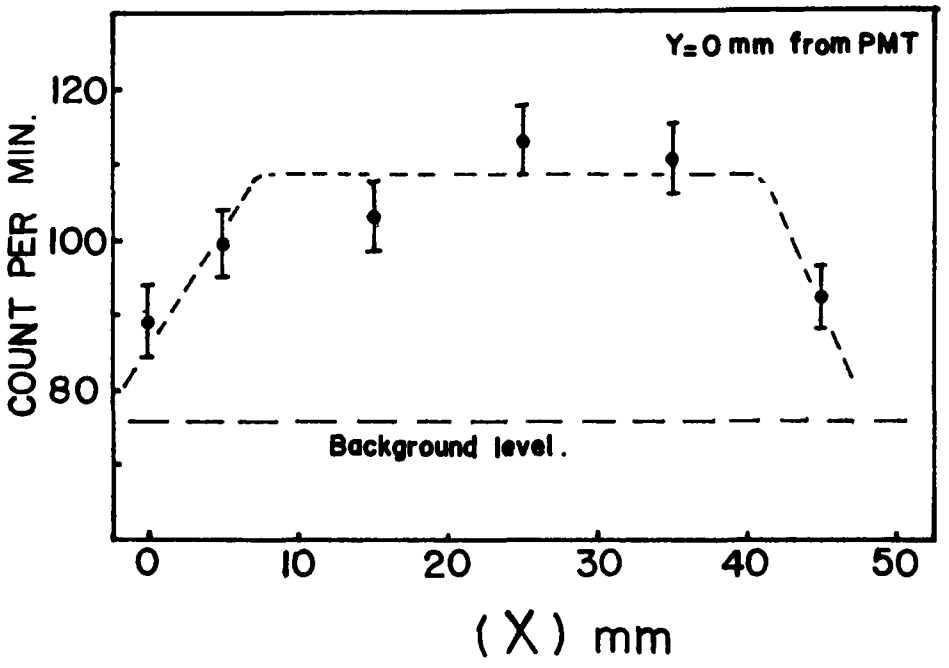

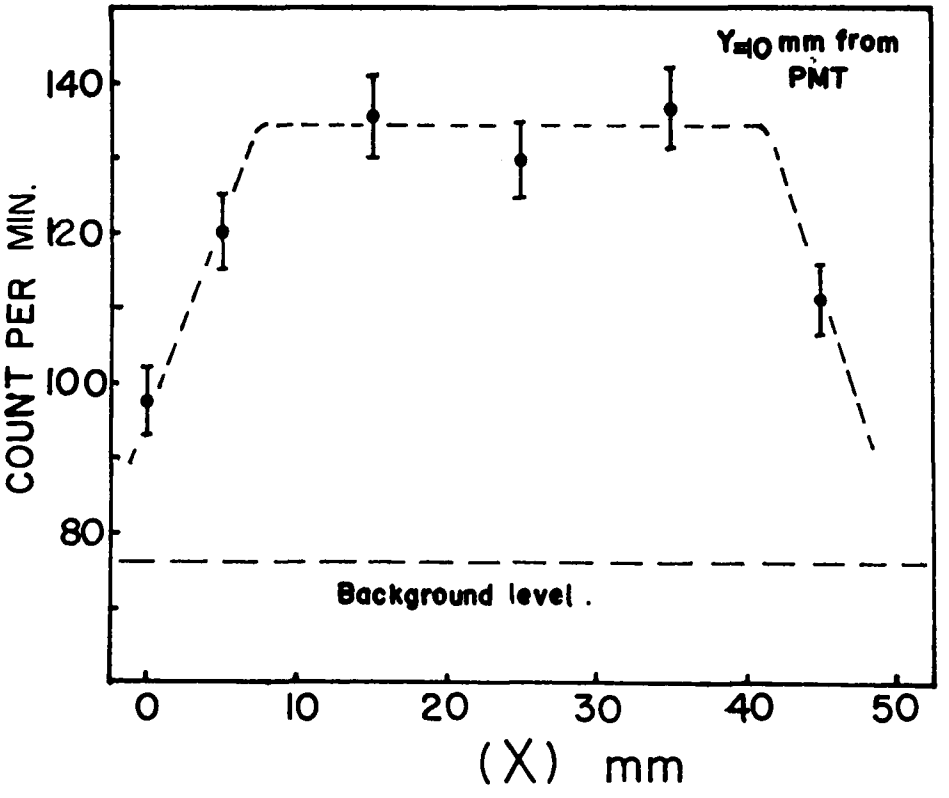

FIGURE (2)

The scintillation response of one 425 μ sheet, (46 mm x 50 mm), as a function of (X).

taking the average of the central points. Due to the low energy of the electrons, the fluctuations in the thickness of the tape shielding the scintillator were important. This contributes to the distance of the experimental points from the curve. The error bars shown take only statistical fluctuations into consideration. From fig. 1, it can be seen that the response is fairly constant across the scintillator.

Fig. 3 shows the response as a function of (y) . The response is seen to decrease as the distance from the photomultiplier increases. The curve shown represents the counting rate expected if the response varied linearly with the distance from the photomutiplier. The points do not fit the curve well, either because the variation is not exactly linear or because of the variation in the thickness of the tape. However it is fairly certain that the response is dependent on the distance from the photomultiplier.

Fig. 4 shows the counting rate as a function of (y) for a long thin strip of 425 micron. Here again, the curve represents a linear variation in the response, which describes the data fairly accurately. The results for two 425 micron scintillators are shown in figures 5 and 6, which indicate that the efficiency is fairly constant across the whole surface of the scintillator. These results indicate that even if the scintillator were 100% efficient, there would be important variations in the strength of the signal as the distance from the photomultiplier is varied. This would not pose too much of a problem in high energy events where most of the shower particles are emitted at small angles to the beam direction, and their distance from the photomultiplier would remain relatively constant.

1.2.2 Detection efficiency

To obtain a high probability of detecting secondary decays, the thin scintillator must be highly efficient. To test the efficiency of the thin scintillator, the set-up

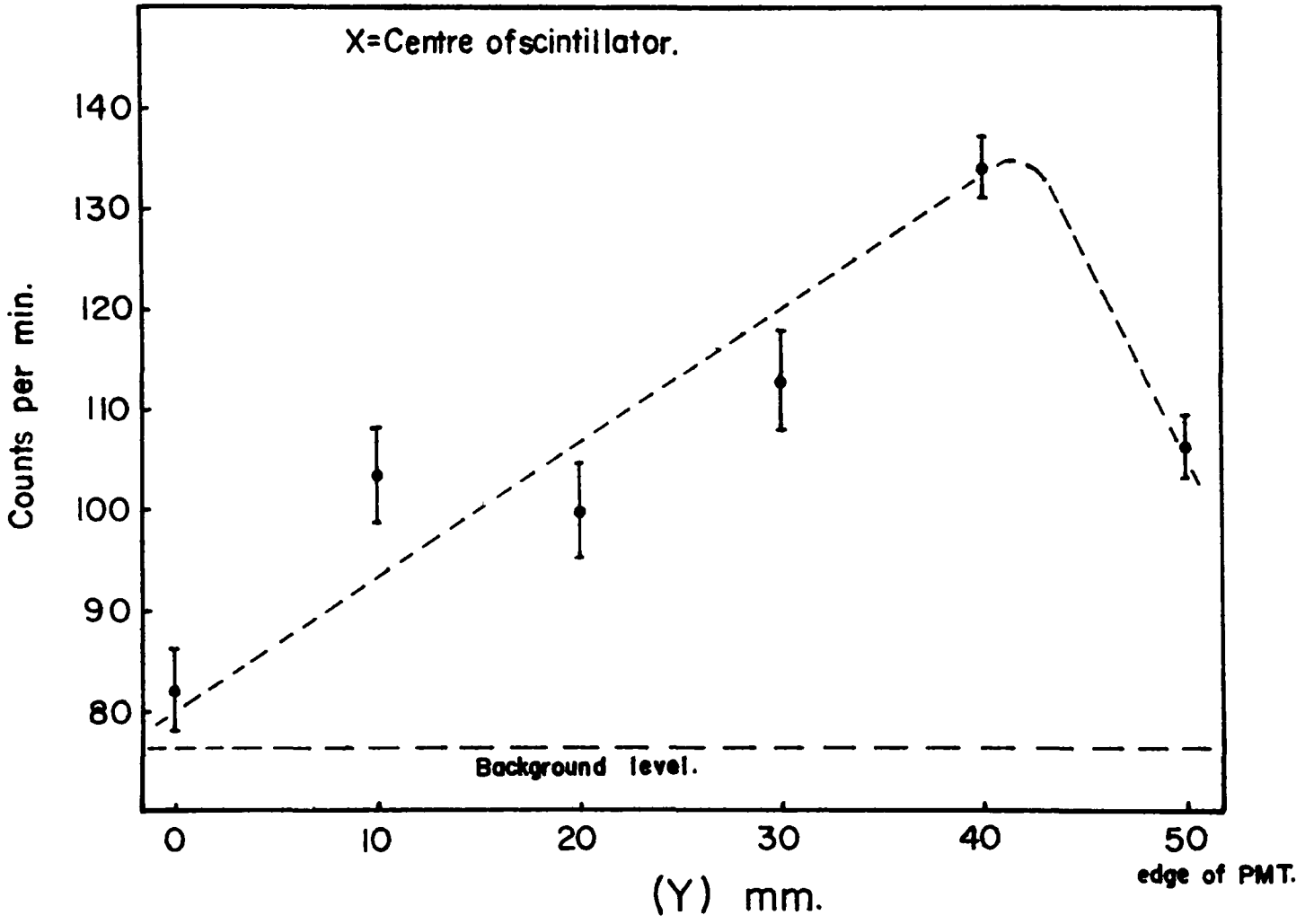

FIGURE (3)

The scintillation response of one 425 μ sheet, (46 mm x 50 mm), as a function of (Y).

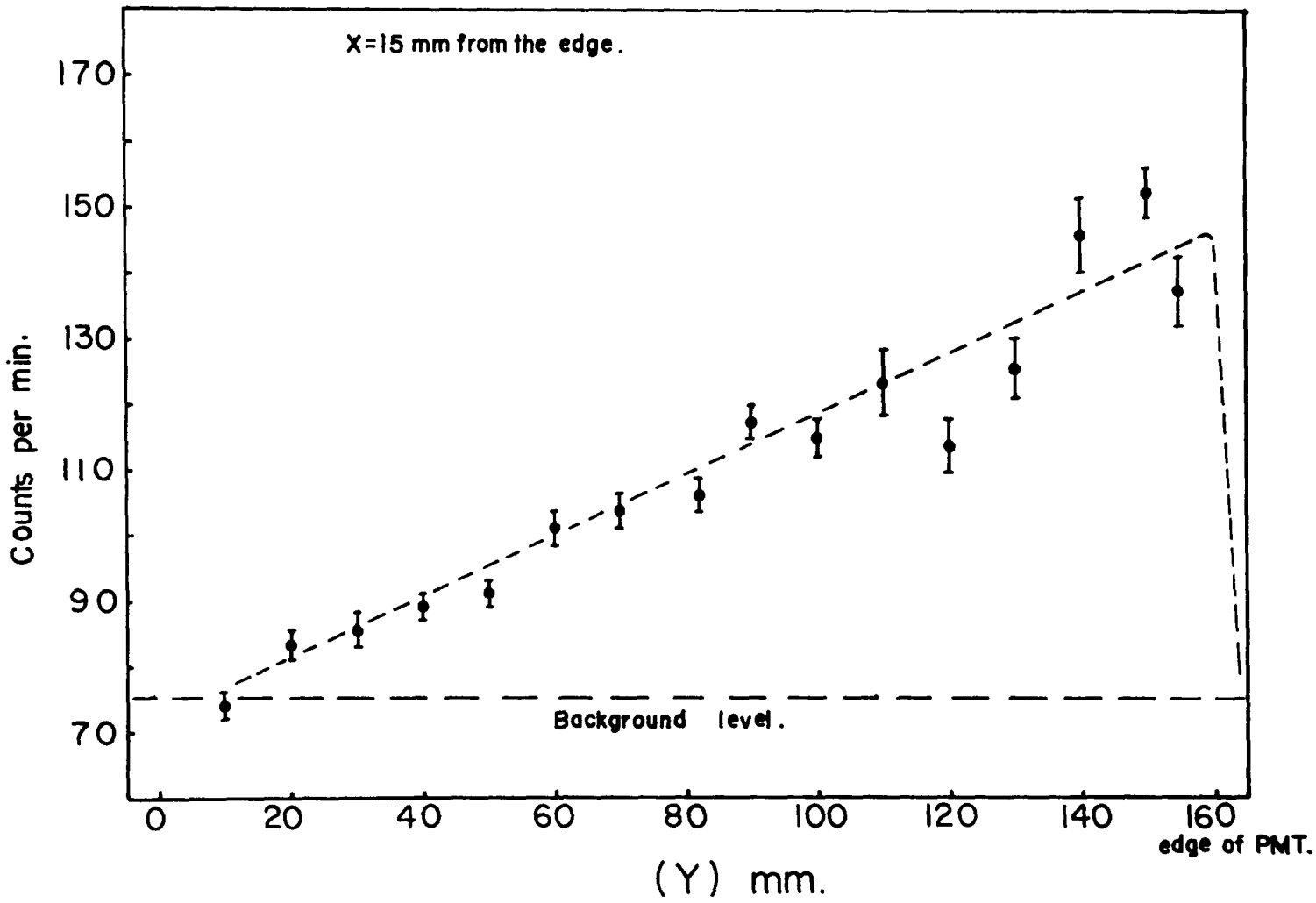

FIGURE (4)

The scintillation response of one 425 μ (30 mm x 153 mm), as a function of (Y).

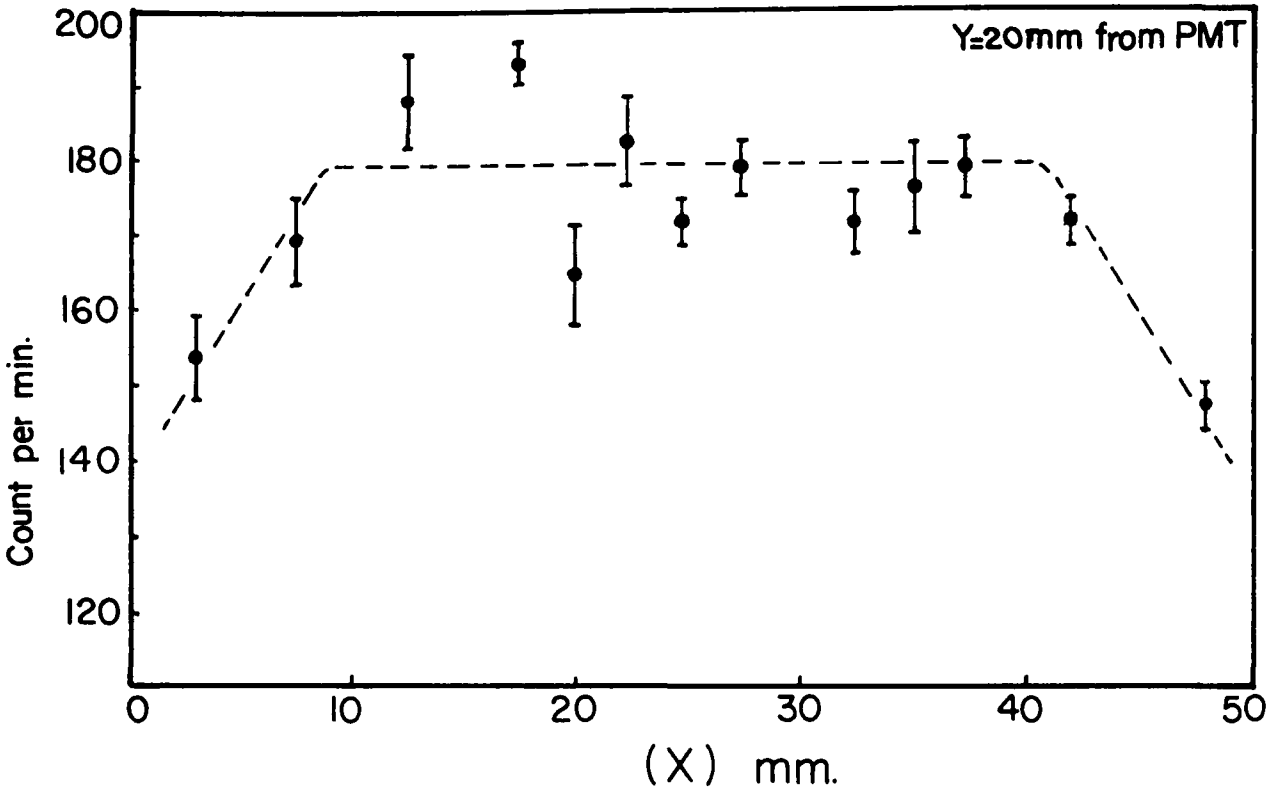

FIGURE (5)

The scintillation response of two 425 μ sheets, 5 cm x 5 cm, as a function of (X).

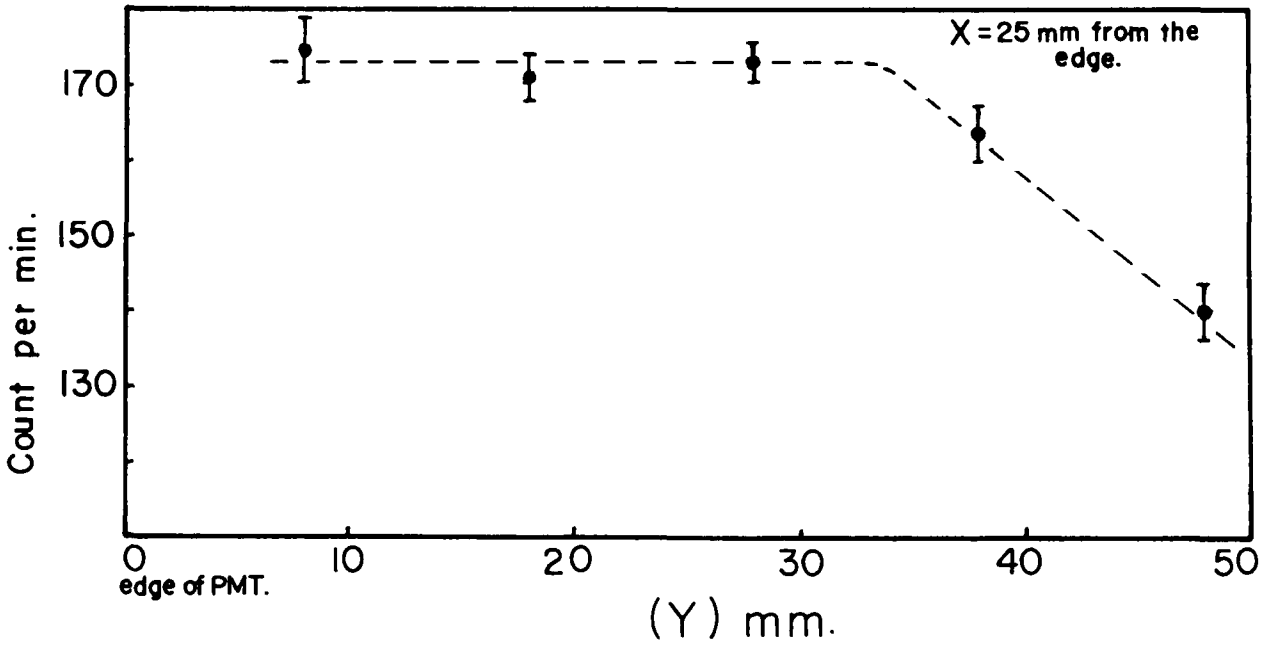

FIGURE (6)

The scintillation response of two 425 μ sheets, 5 cm x 5 cm, as a of (Y).

in fig. 7 was used. The photomultiplier used was a Philips 56-AVP (14 stages), and the applied voltage was varied from 2200 V to 2400 V. A count is recorded if a signal is received from all three scintillators simultaneously. The number of counts expected if all the scintillators were 100% efficient was estimated to be 123 per hour (see appendix A). It was found that one 275 micron sheet is 100% efficient within experimental error. Similar experiments have achieved compatible results [8,18]. The results of the efficiency tests are shown in table (1) and fig. 8.

Different ways of mounting and shielding the scintillator were tried. The best method found is shown in fig. 9. It was found to be very important to minimize the amount of light absorbing materials in contact with the scintillator. For example, using an emulsion between the scintillators results in a strong decrease in the efficiency since $AgBr$ absorbs blue light. Thus the scintillator and the emulsion target will have to be wrapped separately.

Fig. 10 shows the counting rate as a function of the coupling angle of one 125 micron sheet with respect to the photomultiplier tube window. The sheet was coupled directly to the tube by a silicon grease. The points do not fit the central line, either because the collection efficiency is dependent on the coupling angle or because of the coupling itself. Clipping the corners of the scintillator did not show any effect in improving the collecting efficiency of the scintillator. It reduced the counting rate correspondingly with the removed area. The direction of the photomultiplier tube with respect to the earth's magnetic field shows a great effect on the detecting efficiency, so a magnetic shield must be used with the tube to minimize this effect. Different designs of lucite frames, shown in fig. 11, were used as lightpipes to collect the signals from the edges of the scintillator, aiming to improve the detecting efficiency and the energy resolution of the film scintillator. The results are shown in table (2). It was found that the signals from the lucite frames, induced by Cerenkov effect, are comparable with the signals from 100 to

Table 1: The Detection Efficiency of the Thin Scintillators.

Description of scintillator set-up	count per hour		
	2200 V	2300 V	2400 V
two 425 micron sheets, (5 cm x 5 cm)			111 ± 7
one 275 micron sheet, (5 cm x 5 cm)		86 ± 9.2	118 ± 8.9
two 275 micron sheets, (5 cm x 5 cm)	88 ± 6.2		115 ± 7.4
two 275 micron sheets, (5 cm x 5 cm), with 1 mm thick emulsion in between	44 ± 1.4		74 ± 3.9
one 125 micron sheet, (5 cm x 5 cm)			65 ± 6.6
two 125 micron sheets, (5 cm x 5 cm)			93 ± 6.8
two 125 micron sheets, (5 cm x 5 cm). same condition as above with increasing the cavity width of the styrofoam shielding from 1 - 4 cm		100 ± 5	108 ± 7
two 125 micron sheets, (5 cm x 5 cm). same as above with 2 cm cavity			86 ± 6.5
three 125 microns sheets, (5 cm x 5 cm) with 3 cm cavity	86 ± 6.5		
four 125 micron sheets, (5 cm x 5 cm) with 3 cm cavity	90 ± 5.5		
six 125 micron sheets, (5 cm x 5 cm) same as above with two time gain.			120 ± 2.4

Number of counts correspond to 100% efficiency = 123 counts/hour.

Coincidence due to random background noise = 4 ± 0.7 counts/hour.

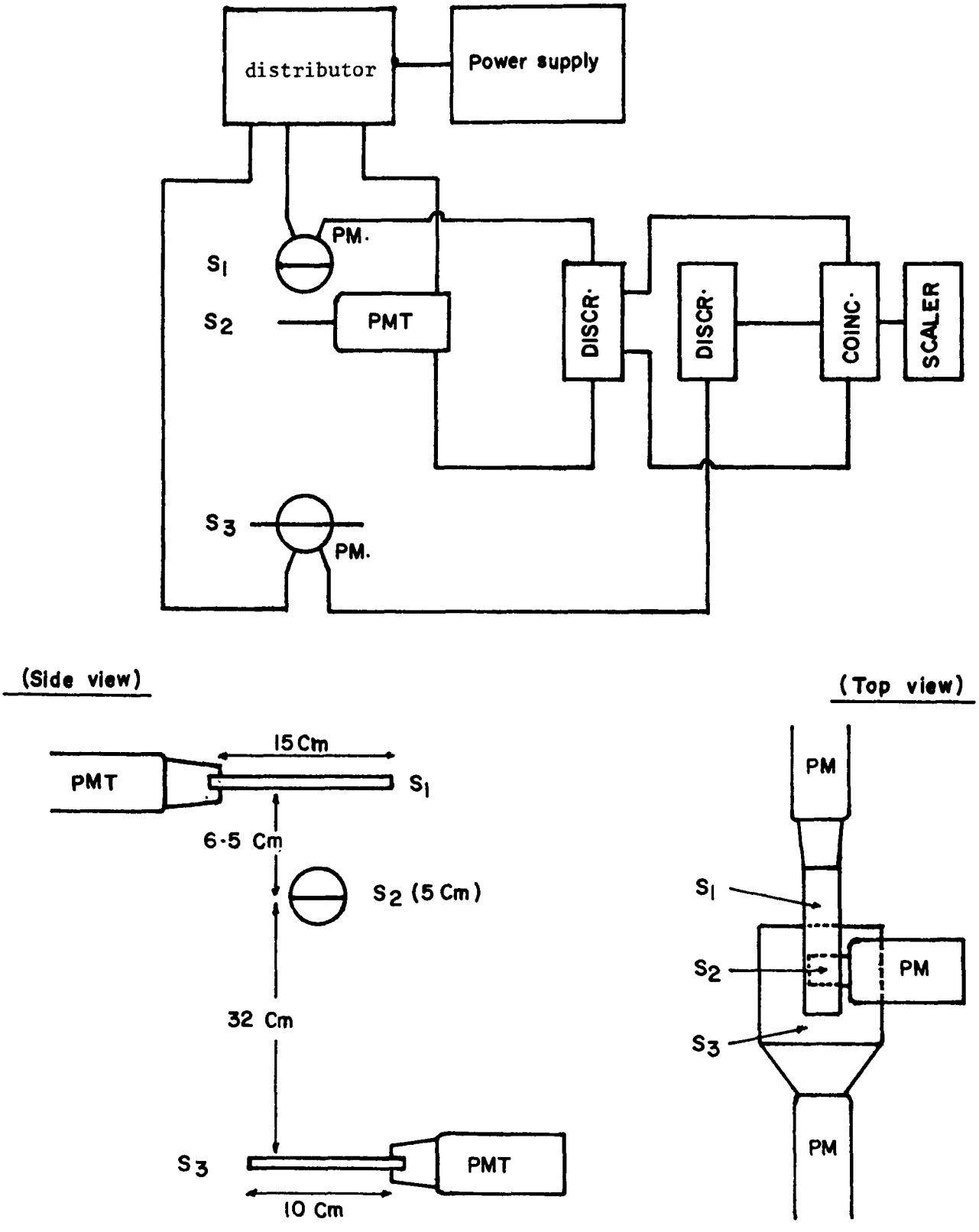

FIGURE (7)

The set-up used to measure the detection efficiency of the thin scintillators.

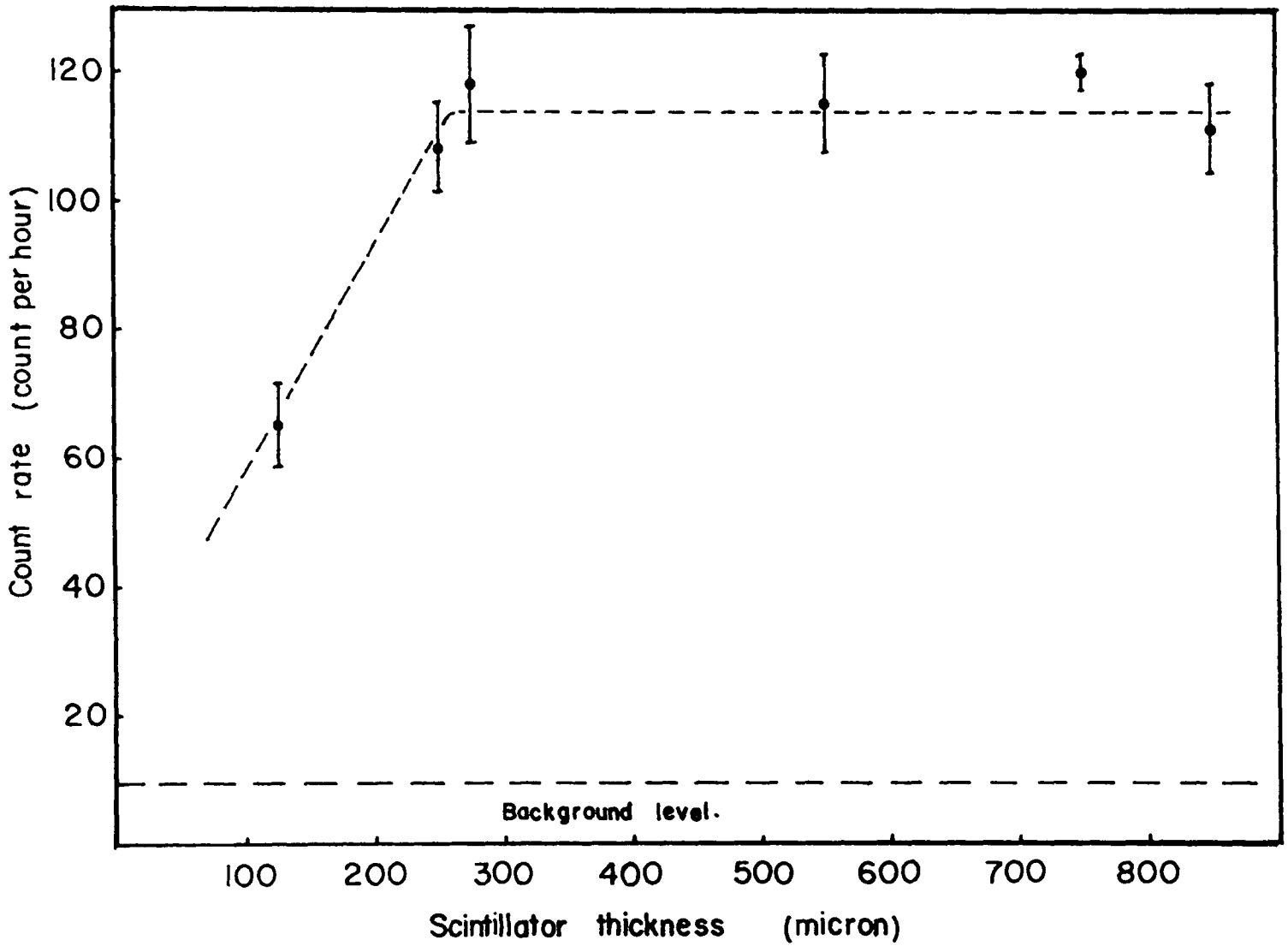

FIGURE (8)

The scintillator efficiency relative to its thickness.

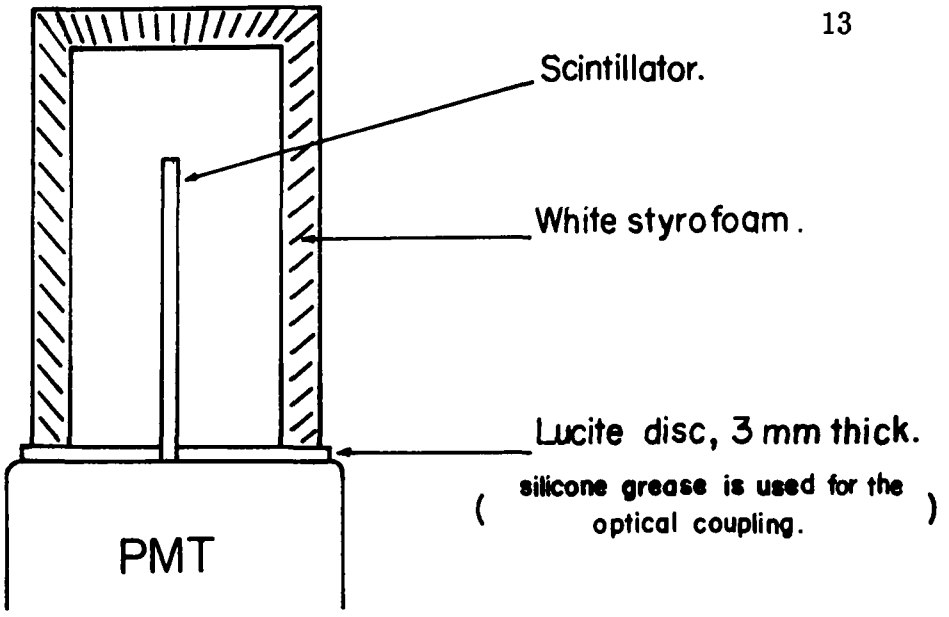

FIGURE (9)

Mounting and shielding of the thin scintillators.

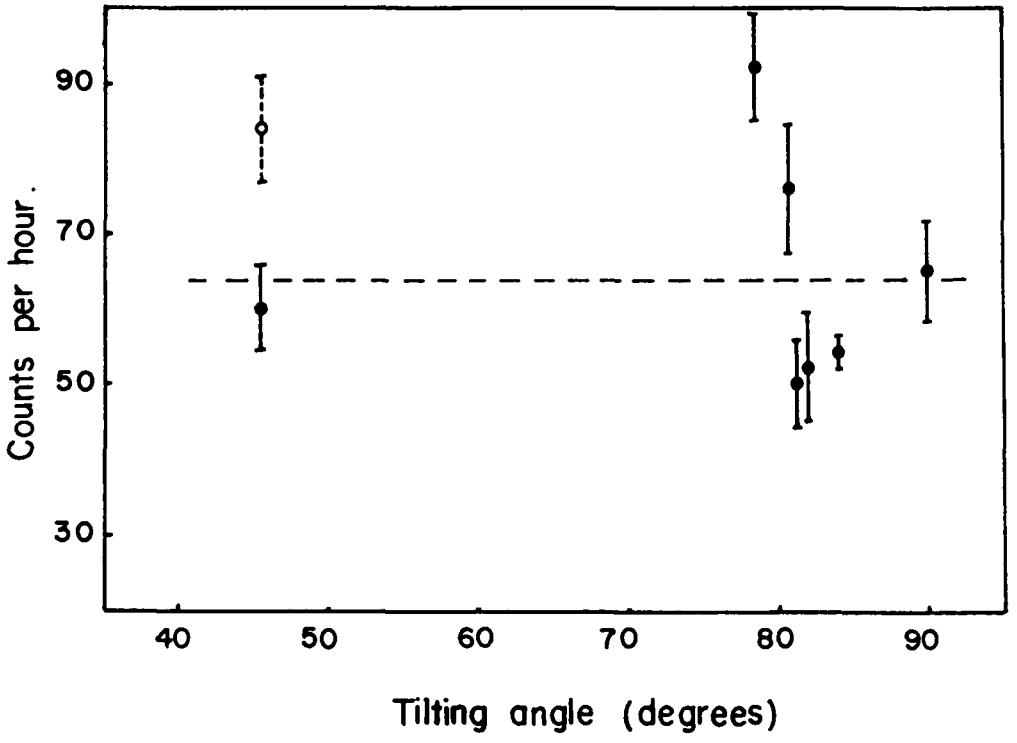

FIGURE (10)

The count rate as a function of the tilting angle for one 125 μ sheet, 5 cm x 5 cm, with respect to the PMT window.

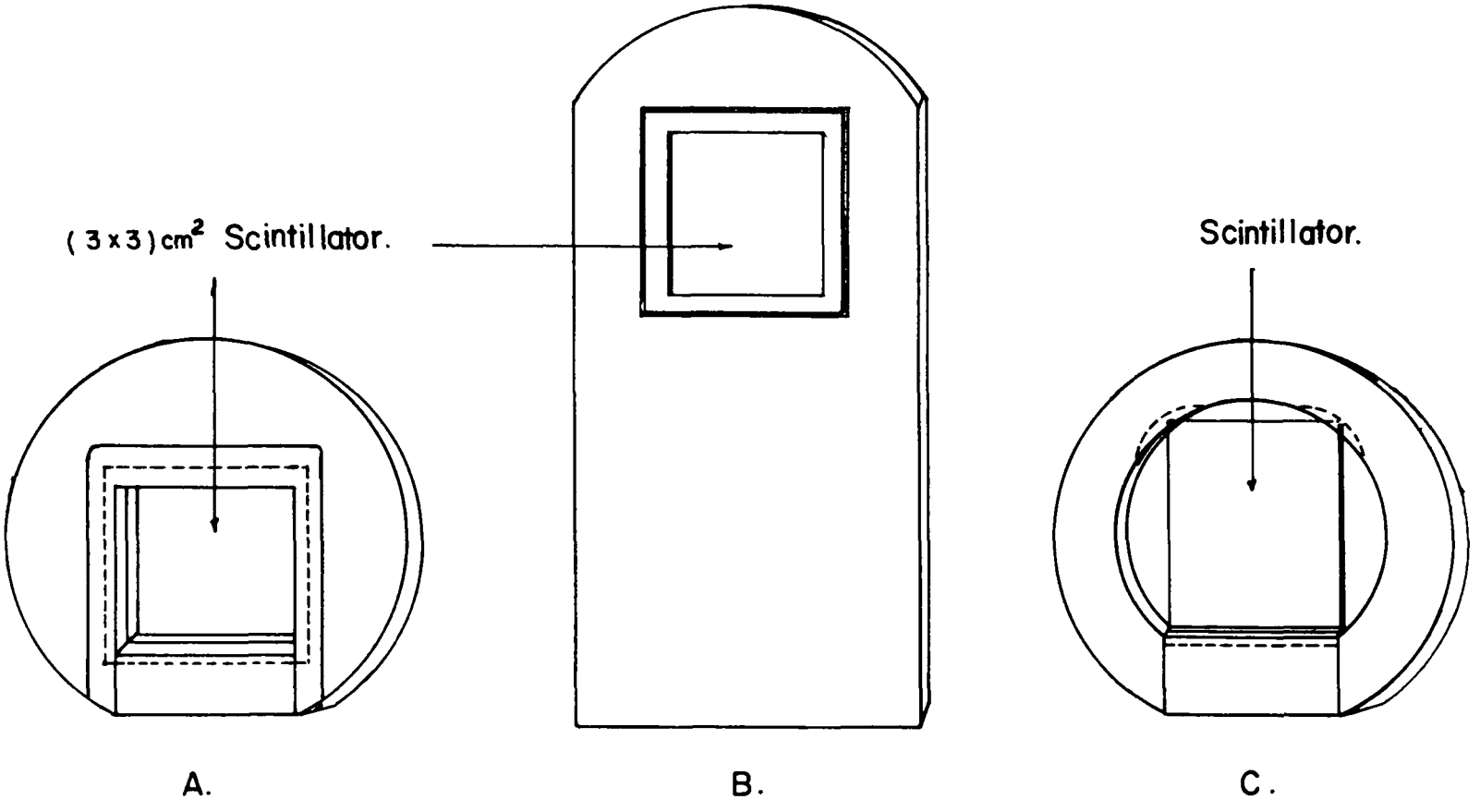

FIGURE (11)

Different lucite designs used to improve the collecting efficiency of the scintillating light.

200 micron of scintillator thickness. This indicates that the lucite support is not a practical feature for successful operation of the thin film detector.

These results indicate that the minimum scintillator thickness needed for 100% efficiency (with minimum ionization particles) is approximately 250 micron.

1.2.3 Pulse height distribution

The pulse amplitude distribution is a fundamental property of the detector output which is routinely used to deduce information about the incident radiation or the operation of the detector itself. The size of the signal from a given particle must not fluctuate too much in a random fashion from one scintillator to another. Random fluctuations could then be mistaken for decays. To measure the size of the signal from the scintillator, the set-up shown in fig. 12 was used. The signal from the photomultiplier is amplified by a factor of two and then split in two halves, one going to the coincidence circuit and the other to the storage scope (after it is delayed to match with the trigger signal) for the readout. The scope (Hewlett Packard 1744A) is triggered externally by a pulse from the coincidence circuit each time there is a coincidence signal. The three photomultipliers were operated at 2300 V with a discrimination level of 100 mV. Fig. 13 and 14 show the pulse distribution from one sheet and three sheets of 125 microns. As expected, the peak position (corresponding to the amplitude of the induced signal) is proportional to the thickness of the film scintillator.

It is clear that the signal from one sheet of 125 microns is comparable to the regular noise signal (fig. 15) of the photomultiplier. The measurements of the pulse signals show that 10% of total signals were over one volt. This is possibly due to the space charge effect between the last dynode (of the photomultiplier) and anode where the number of electrons is greatest.

Fig. 16 and 17 show the signal distribution from four 75 micron and nine 75

Table 2: The Effect of the Coupling Method on the Detection Efficiency of the Thin Scintillators.

Description of scintillator set-up	Count per hour
	2400 V
one 125 micron, (3 cm x 3 cm), coupled by lucite light pipe of (3 x 1 x 0.3) cm^3	38 ± 1.4
same as above with white paper (25 micron thick) covering the scintillator	22.5 ± 3.3
same as above with using aluminum foil (35 micron thick) instead)	24 ± 4.2
as above with saran-wrap covering the scintillator	30 ± 3.2
two 125 micron sheets, (3 cm x 3 cm), coupled by lucite light pipe of (3 x 1 x 0.3) cm^3 and covered by saran-wrap	46 ± 2.8
same as above with a piece of black plastic (100 thick) cover the scintillator	31 ± 3.1
one 125 micron, (3 cm x 3 cm), held by lucite from in a horse-shoe shape	43 ± 3.2
as above with aluminum foil covering the scintillator	36 ± 1.5
same as above with cigarette foil covering the scintillator	31 ± 3.2
two 125 micron sheets, (3 cm x 3 cm), separated by white paper (25 μ) and hold by white paper (25 μ) and hold by lucite frame covered with aluminum foil	46 ± 3.7
three 125 micron sheets, (3 cm x 3 cm), set same as above	58 ± 7.6
no scintillator, just the lucite frame coupled to the photomultiplier tube (background noise)	9 ± 1.1

Number of counts corresponding to 100% efficiency = 72 counts/hr

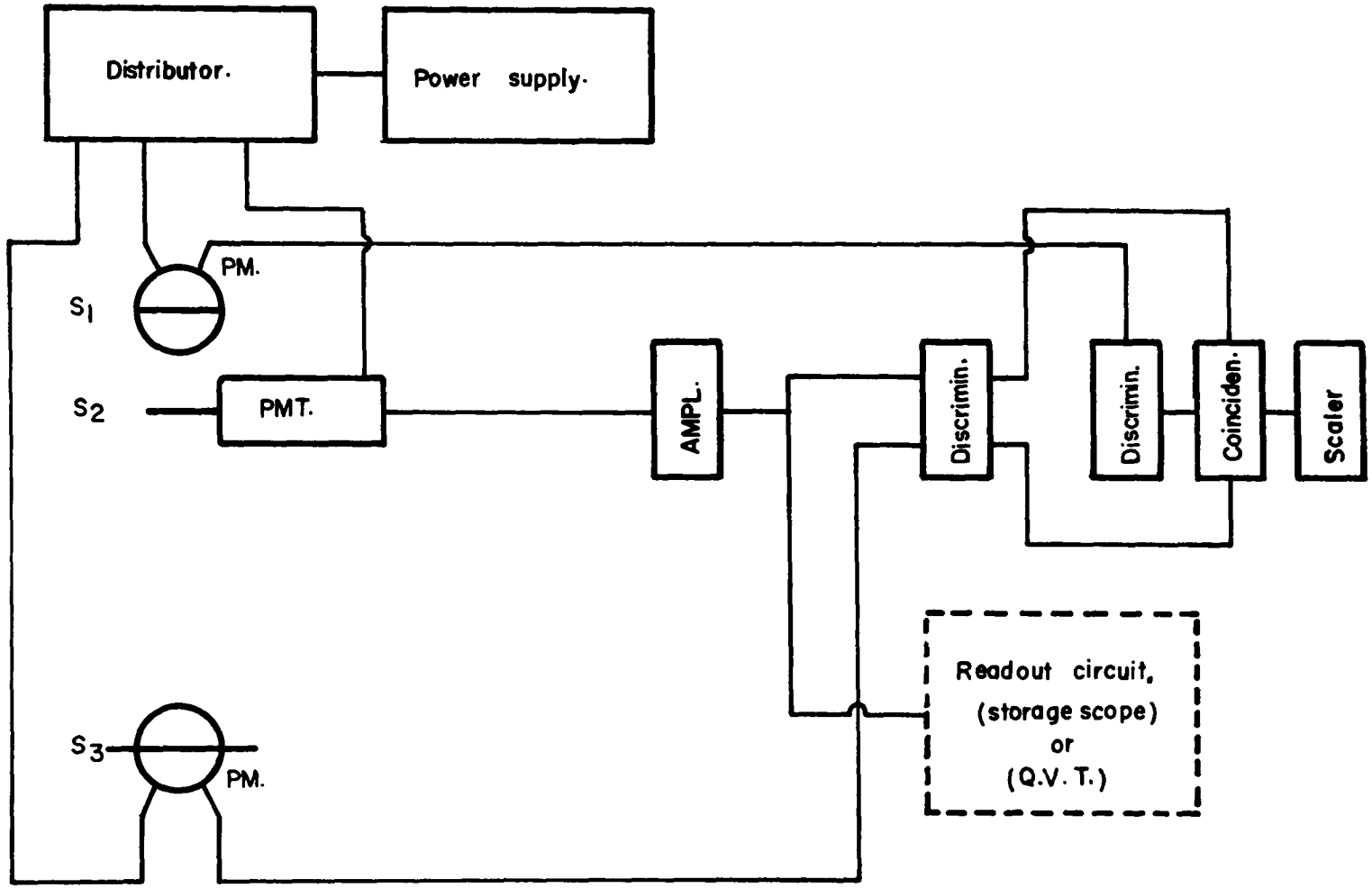

FIGURE (12)

The set-up used to measure the pulse height distribution and energy resolution.

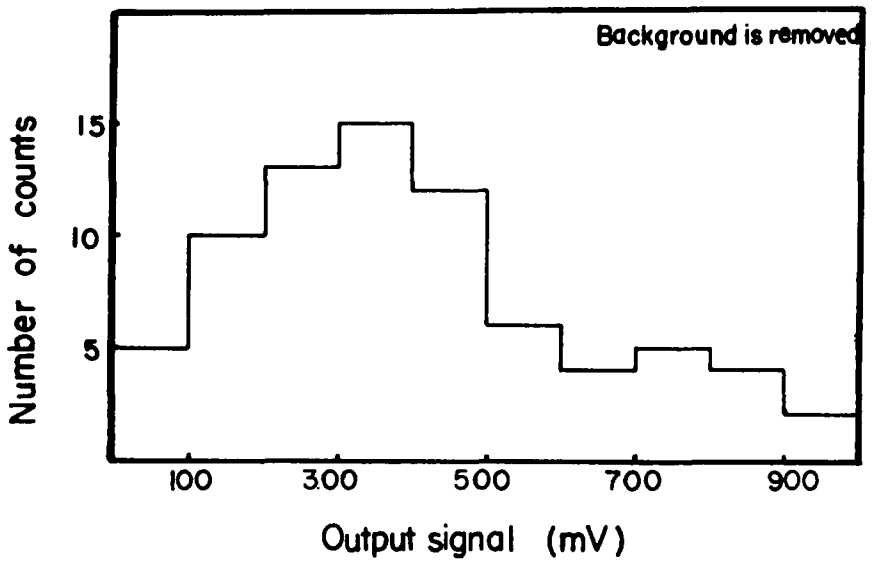

FIGURE (13)

Signal distribution for three 125 μ sheets of (3 cm x 3 cm), with 3-fold coincidence.

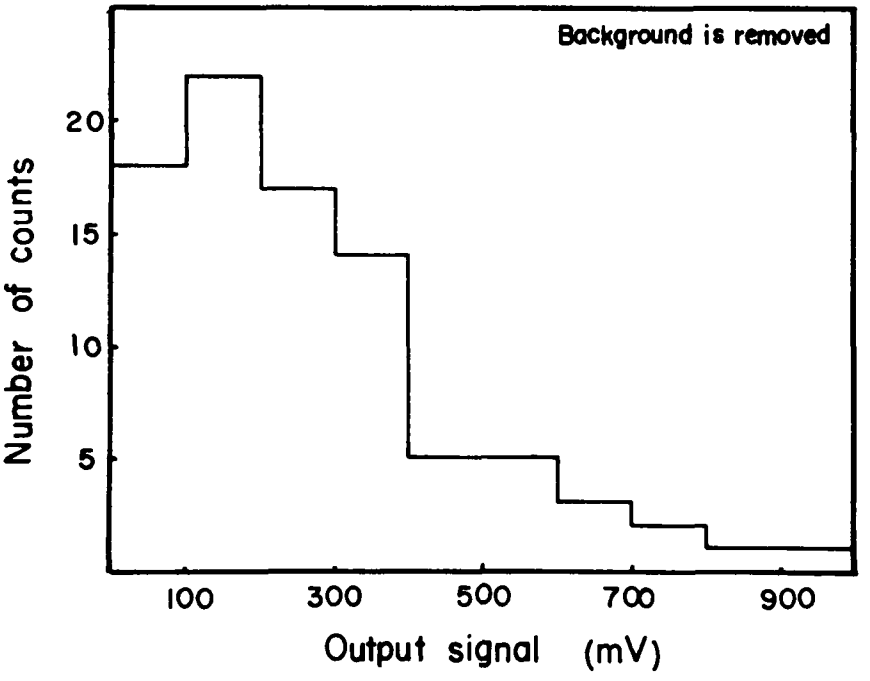

FIGURE (14)

Signal distribution for one 125 μ sheet of (3 cm x 3 cm), with 3-fold coincidence.

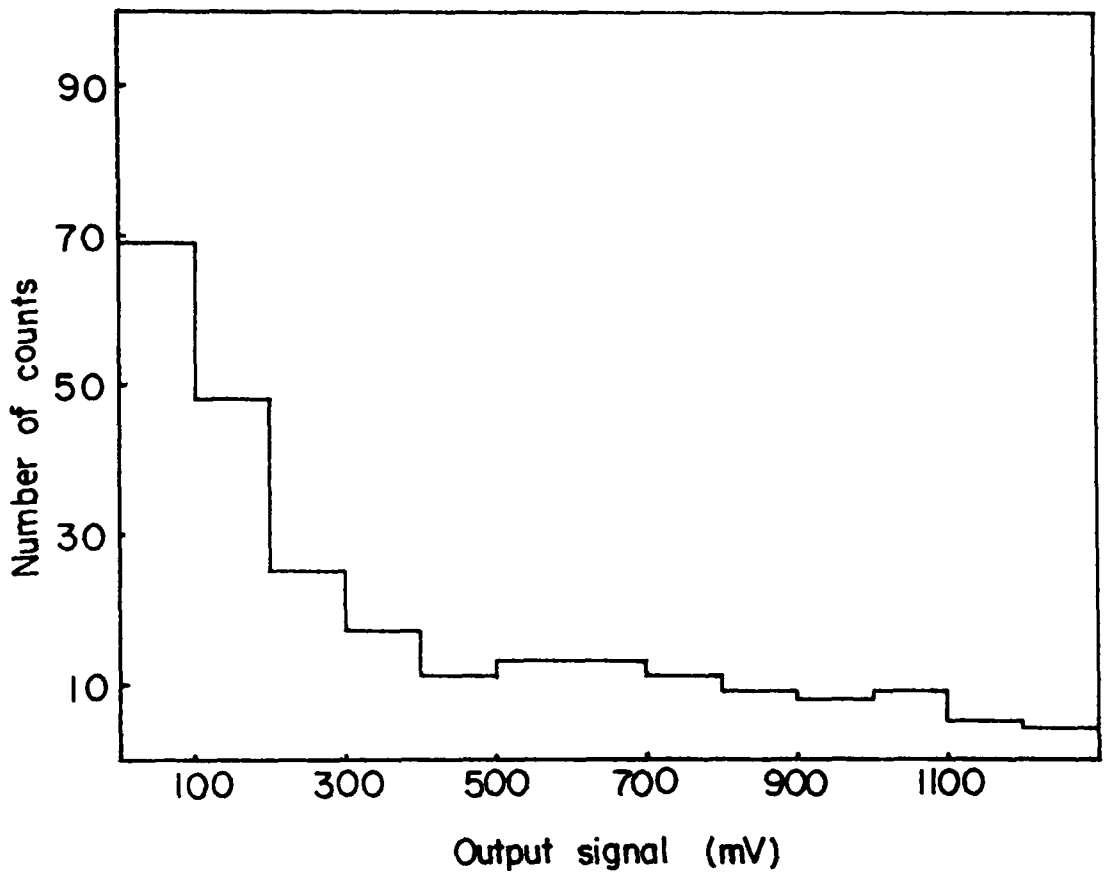

FIGURE (15)

The signal distribution for the photomultiplier tube noise.

micron sheets. For such thickness of scintillator, one would expect to have a bigger signal than with the three 125 micron sheets. It is fairly clear that the signal is small and comparable to the noise level of the photomultiplier tube. This could be related to the irregularity in the surface of the scintillator material (especially for 75 microns thick) and to the absorption caused by the grease layers that separate the scintillators. Bad optical coupling could be one of the reasons too.

1.2.4 Energy resolution

It was well known that scintillators possess poor energy resolution, and therefore the spectra has relatively broad peaks. Many factors contribute to the resolution loss, but the most significant ones are dependent on the scintillator material itself and to the characteristics of the photomutiplier tube. The variance introduced by the photomultiplier tube can be a significant contribution. Uniformity of photoelectron collection from the photocathode is an important factor, as is the statistical fluctuation in the electron multiplication.

Fig. 12 shows the set-up used to measure the energy resolution of thin scintillator sheets. A multichannel analyzer is used for the readout of the output signals. The signal distribution for 125 μ, two 125 μ, and three 125 micron sheets are shown in fig. 18. It is obvious that the resolution is very poor, since the number of photons that reaches the photocathode is very small. The figure shows a weak signal for the 125 μ sheet that is comparable to the noise signal of the photomultiplier tube (this confirms the result found before). The distribution, for two 125 μ and three 125 μ, seem to be clipped in the low energy part of the signals. This could be related to the small size of the induced signal that is less than the discrimination level. Fig. 19 shows the pulse distribution for 275 μ, 425 μ, and six 125 micron sheets. There is not much improvement on the energy resolution of the signal, only for the 425 μ

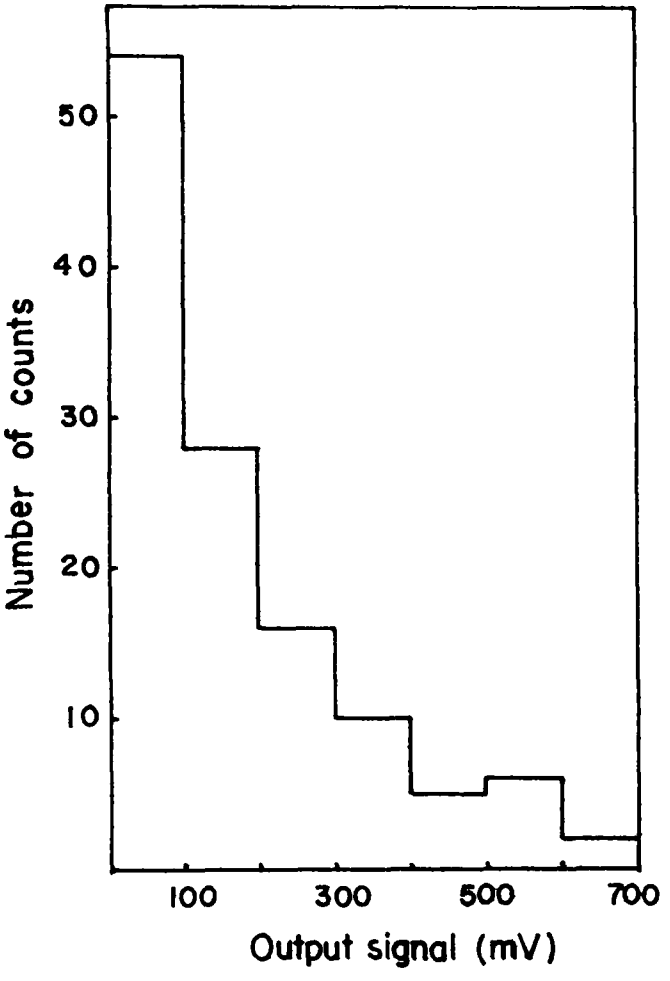

FIGURE (16)

Signal distribution for four 75 μ sheets, (3 cm x 3 cm). The background is removed.

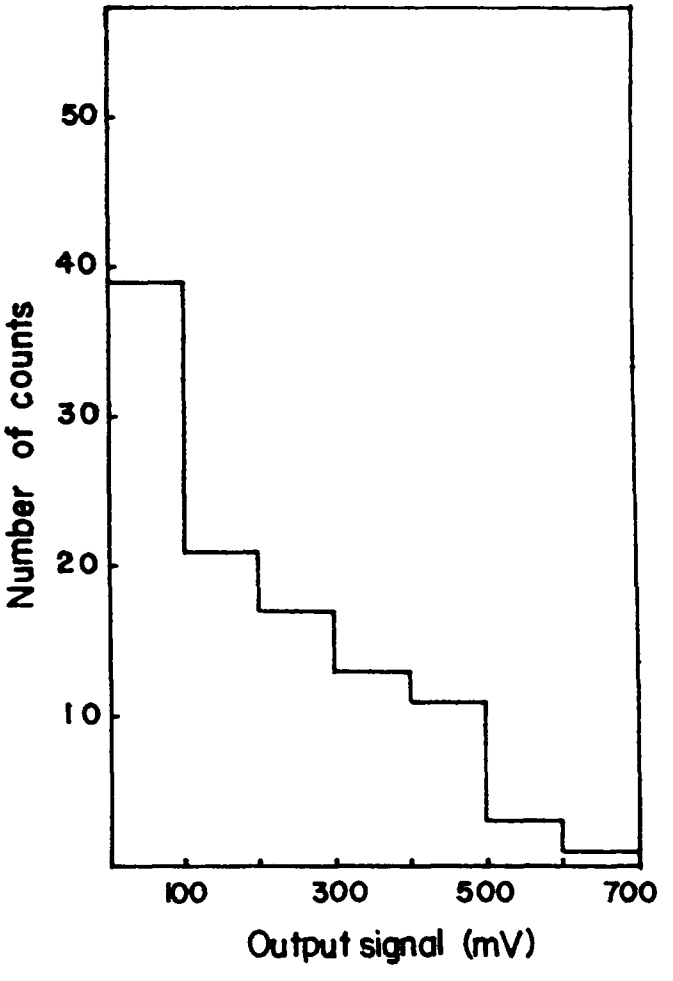

FIGURE (17)

Signal distribution for nine .75 μ sheets, (3 cm x 3 cm). The background is removed.

Figure (18)

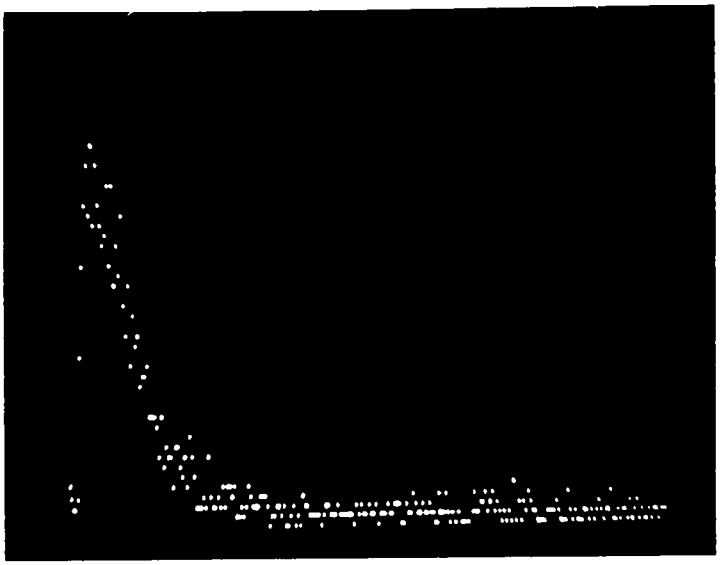

a.

Signal distribution for
one 125 μ sheet, 5 cm x 5 cm,
with 3-fold coincidence.

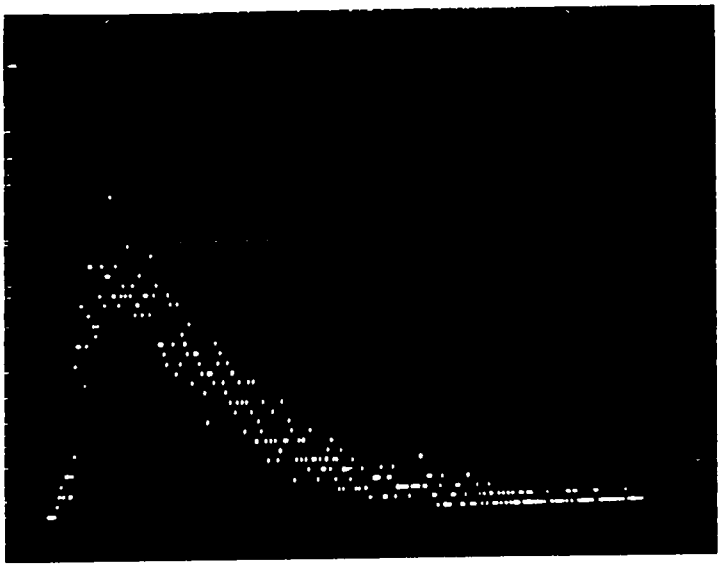

b.

Signal distribution for
two 125 μ sheets, 5 cm x 5 cm,
with 3-fold coincidence.

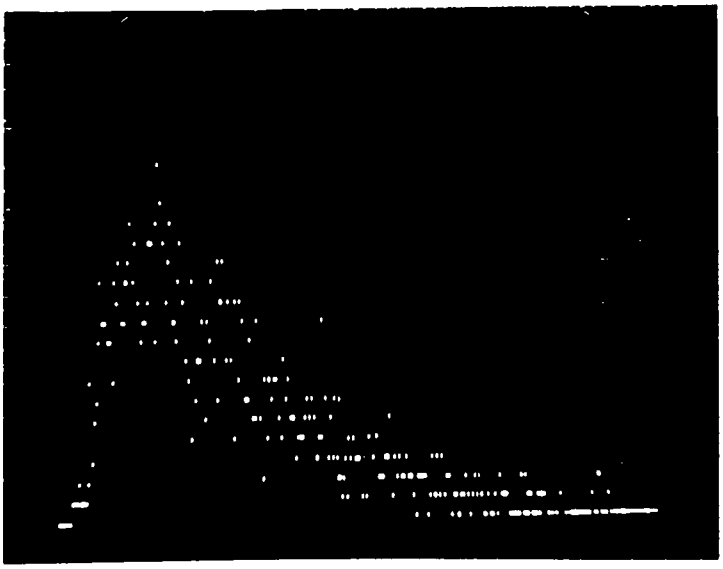

c.

Signal distribution for
three 125 μ sheets, 5 cm x 5 c
with 3-fold coincidence.

sheet which shows a more uniform signal. The results fail to show any improvement in the energy resolution with the multilayer scintillators over a similar scintillator of comparable thickness. This may be due to the high absorption of the light signals within the multilayer scintillators, caused by the grease layers that separate the scintillators.

1.2.5 Performance of thin scintillator strips

It is hoped that small strips of thin scintillators can be used as detecting elements in constructing a thin film detector that has better spatial resolution than one with a regular scintillator sheet form.

The induced signals, from the strips, are collected from both ends using a fiber optic coupling. Since the collected signal represents the fraction of light that is coming directly from the point of interaction to the edge, plus part of the light that is reflected (by total internal reflection) between the surfaces of the strip, there will not be much loss in the detection efficiency due to the reduction in the scintillator size. Fig. 20 show the set-up used to study the signal distribution from the scintillator strips. With a point source of Sr^{90} (1 μCu and 1 mm diameter opening), four 125 micron strips of $0.8mm \times 30mm$ size, mounted as in fig. 21, were tested. The strips are coupled by quartz fiber optics (1 mm diameter) to the photomutiplier tube. Fig. 22 shows the signal from both ends of single 125 micron strip with the source close to one of the two ends. The distribution shows sign of discrimination effect between the two ends, which seems to correspond to the position of the radioactive source. This has been checked later (by switching the PMT tubes) and found to be related to the characteristics of the photomultiplier tube, not the scintillator.

Fig. 23 and 24 show the signal from both ends of the same strip. The signal

Figure (19)

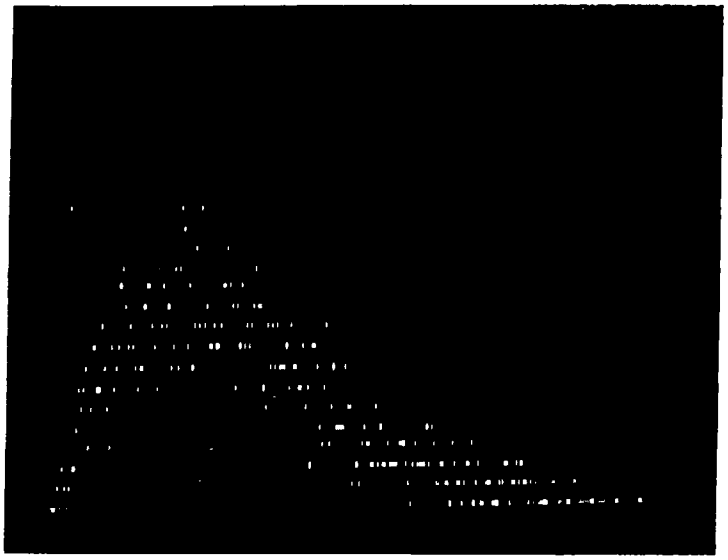

a.

Signal distribution for one 275 μ sheet, (5 cm x 5 cm), with 3-fold coincidence.

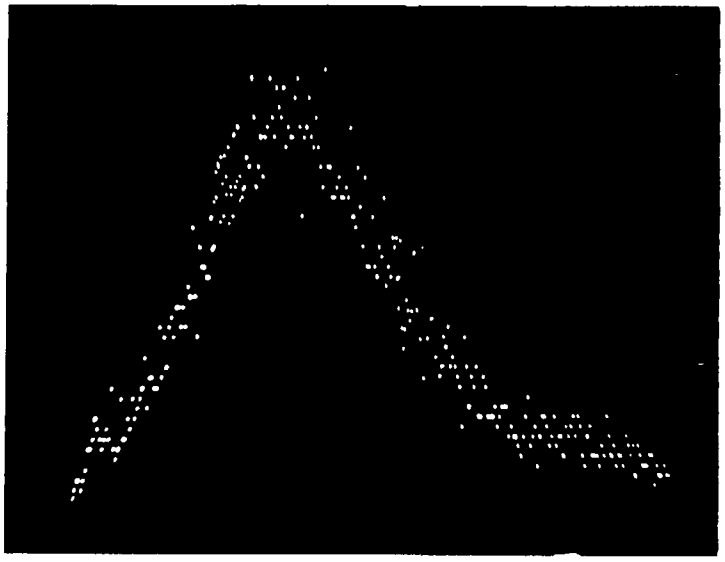

b.

Signal distribution for one 425 μ sheet, (5 cm x 5 cm), with 3-fold coincidence.

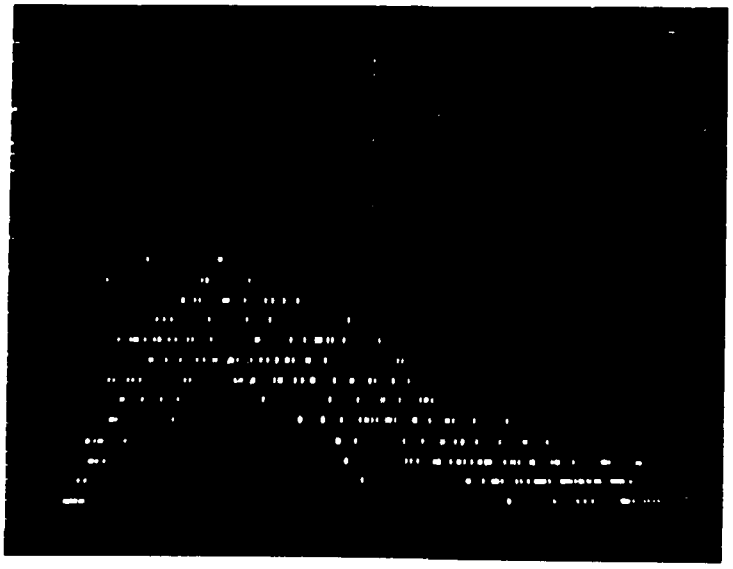

c.

Signal distribution for six 125 μ sheets, (5 cm x 5 cm), with 3-fold coincidence.

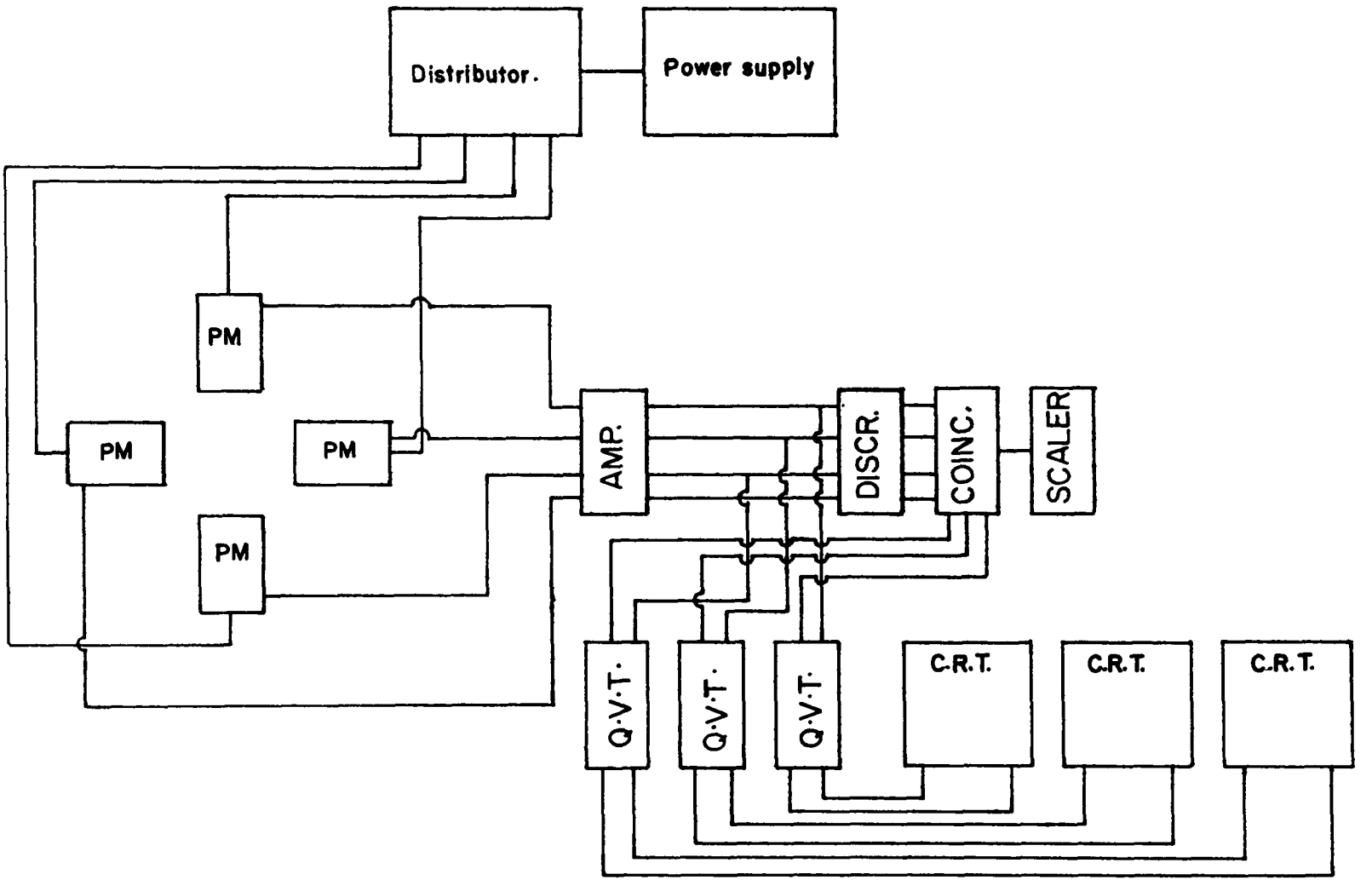

FIGURE (20)

The set-up used to study the signal distribution from the scintillator strips.

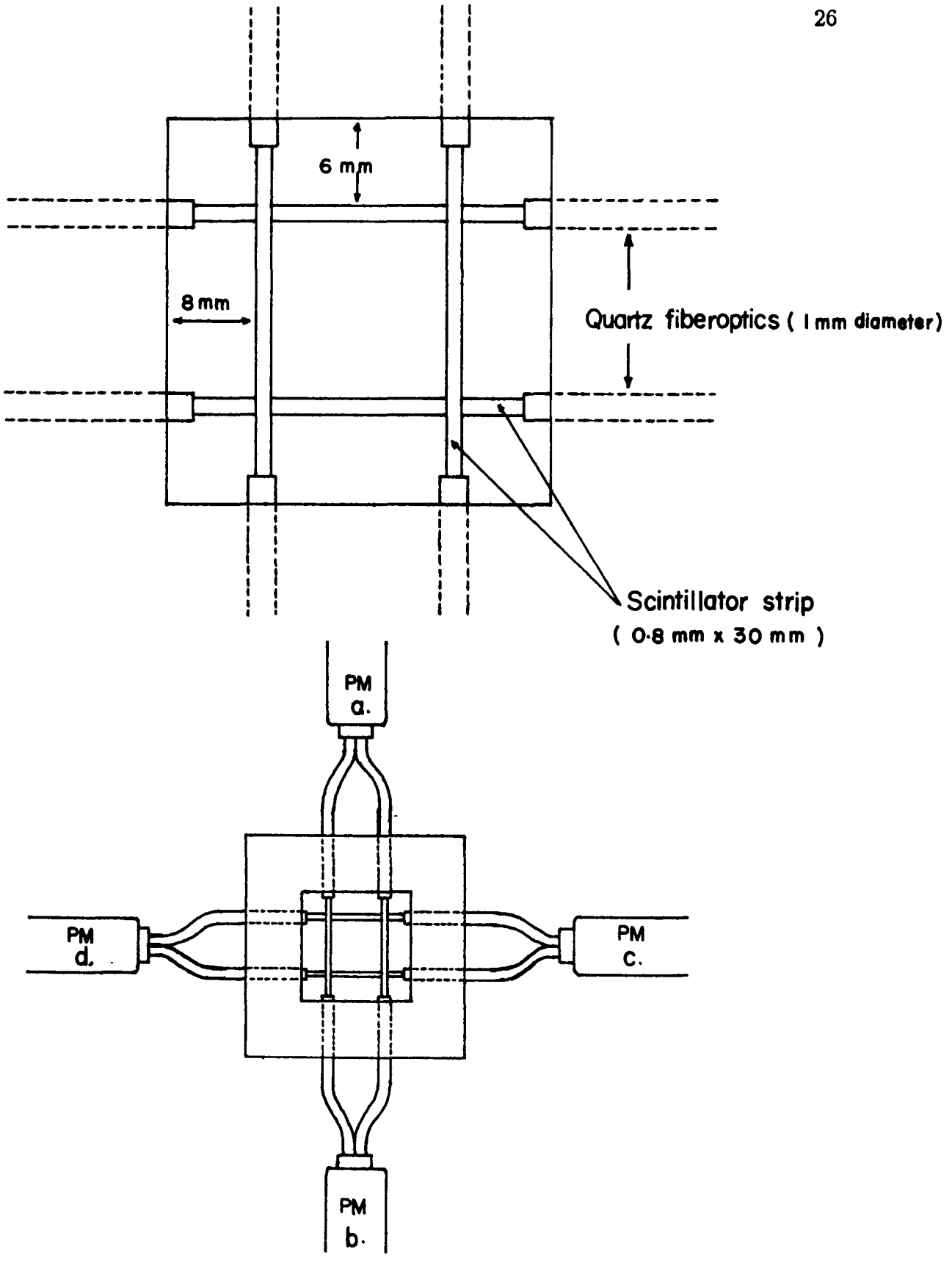

FIGURE (21)

The coupling of the scintillator strips.

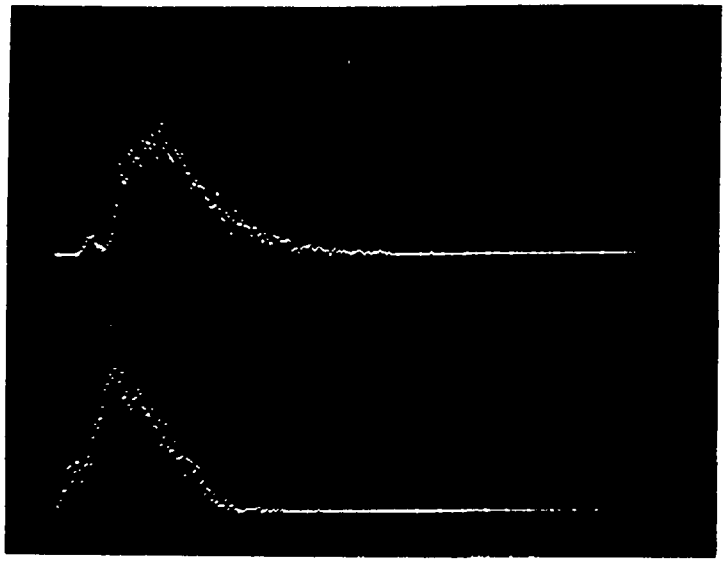

Figure (22)

Signal distribution from both ends of 125 μ strip , with S_r^{90} near the end A

top-end (A)
bottom-end (B)

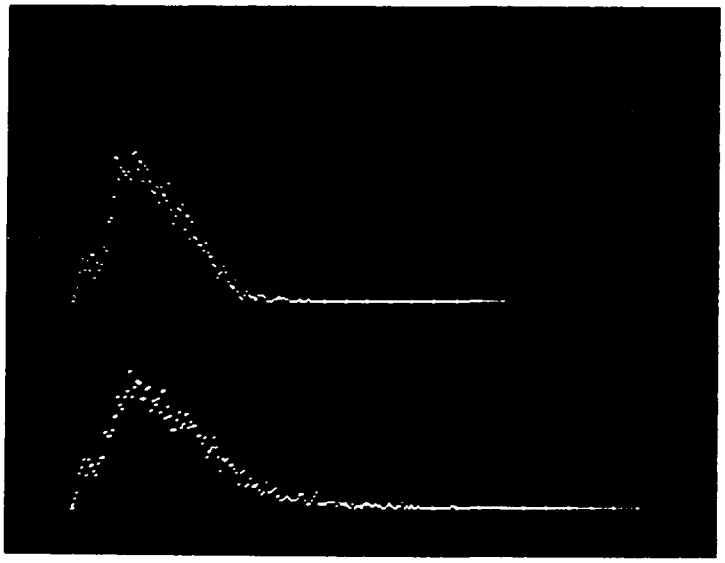

Figure (23)

Signal distribution from the end (B) of 125 μ strip, (0.8 mm x 30 mm).

Top-S_r^{90} near the end
bottom-S_r^{90} far from the end

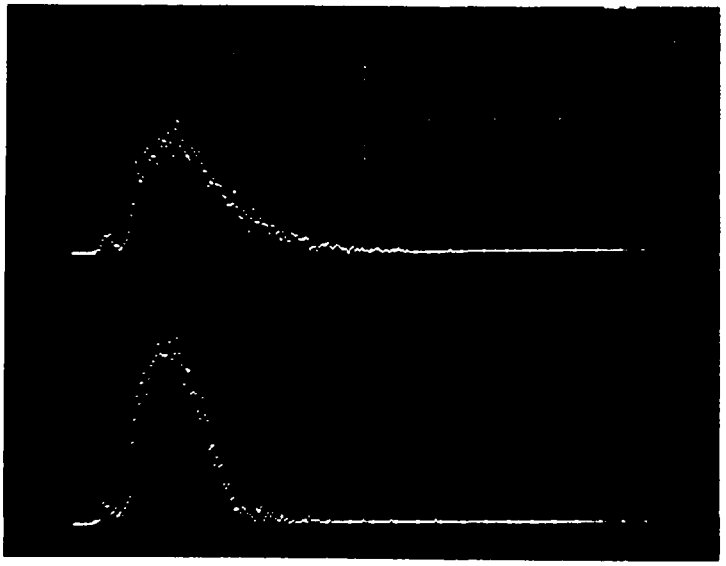

Figure (24)

Signal distribution from the end (A) of 125 μ strip, (0.8 mm x 30 mm).

Top-S_r^{90} near the end
bottom-S_r^{90} far from the end.

from ($0.6mm \times 30mm$) strip of a 125 micron thickness is shown in fig. 25(a,b) with the corresponding noise signal from the photomultiplier tube. Relative to such a thickness (125μ), the signal looks fairly good. This may be due to the uniformity of the strip and the good coupling.

Signals from a 125-micron strip were compared with those from a 275-micron strip; both are (1.5 mm×30 mm). The results are shown in fig. 26 . Figure 27 shows the signals from the same set-up with (0.8 mm × 20 mm) strips. The signal does not seem to be affected by the reduction of the strip size. The strips have also been tested with particles passing through it from the narrow edge. Fig. 28 shows the induced signal from 125-micron strips (0.4 mm × 20 mm) size, coupled by quartz fiber optics, exposed to beta-particles (from Sr^{90}) set to pass through its width (400μ) from the edge. From the figure, it is clear that the second peak corresponds to the particles passing across the total width of the strip (400μ), while the first peak corresponds to the particles taking shorter paths across the scintillator. To verify this result, the source has been removed and reset again in the same position (approximately). The result is shown in fig. 29 . It is fairly clear that the second peak (corresponding to a 400μ path) is still in the same position, but not so well defined. This may be related to the shift in the position of the source from the center of the strip. Fig. 30 shows the signal from the scintillator strip of five 125-micron laminations set in the same way with respect to the radioactive source.

The results indicate that scintillator strips can be stacked together and used to provide good detection efficiency and high resolution (relative to the thickness of the strips) in a detector that incorperate the newly developed imaging tubes.

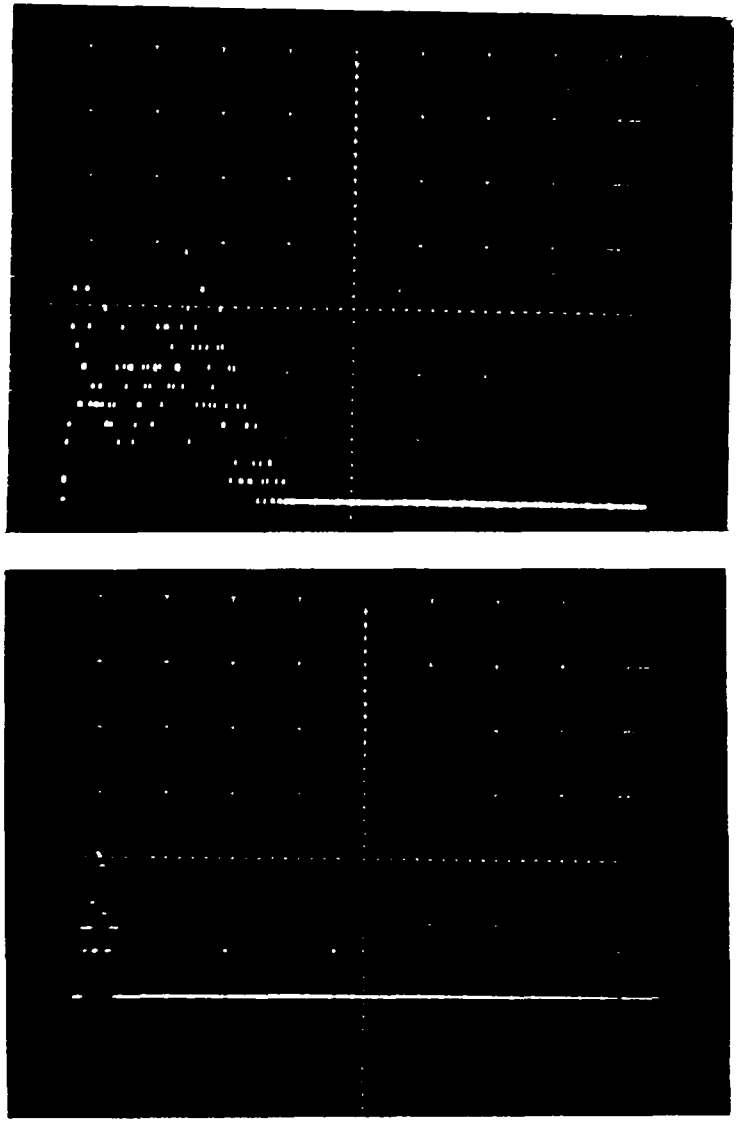

a.
Top- the signal from the end (B) of the strip
bottom - the corresponding noise signal

Figure (25)
Signal distribution for 125 μ strip, (0.6 x 30) mm^2, with 3-fold coincidence and Sr^{90} near the end (A).

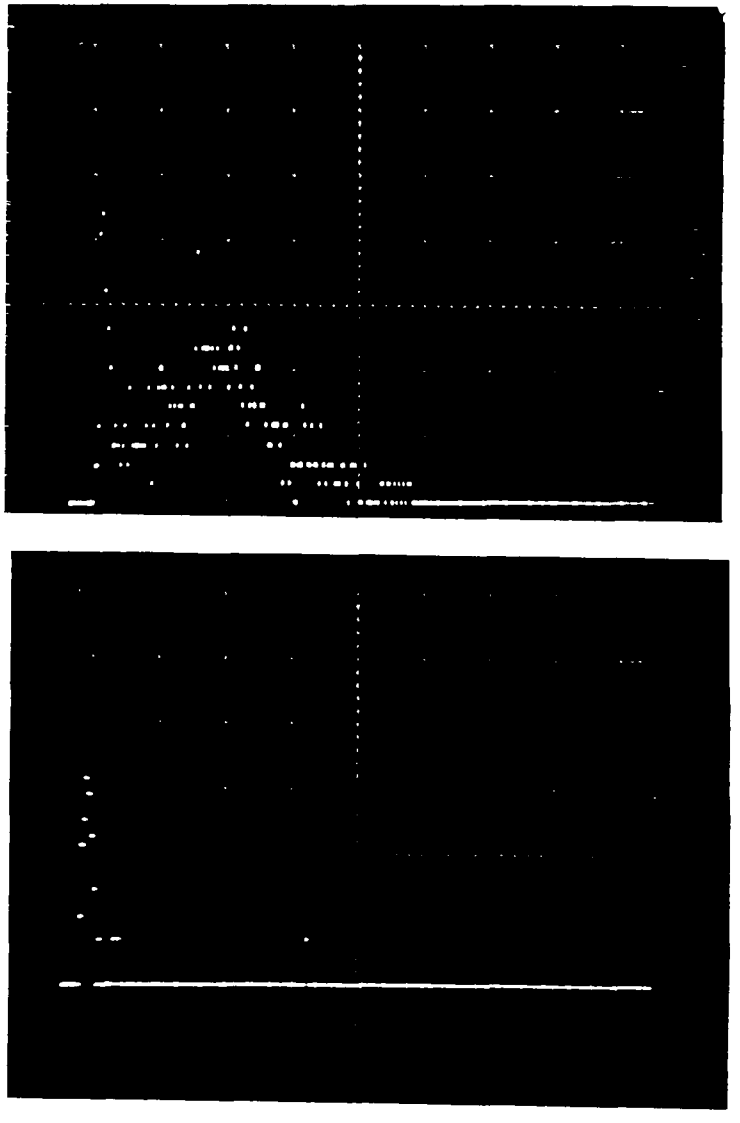

b.
Top- the signal from the end (A) of the strip
bottom- the corresponding noise signal

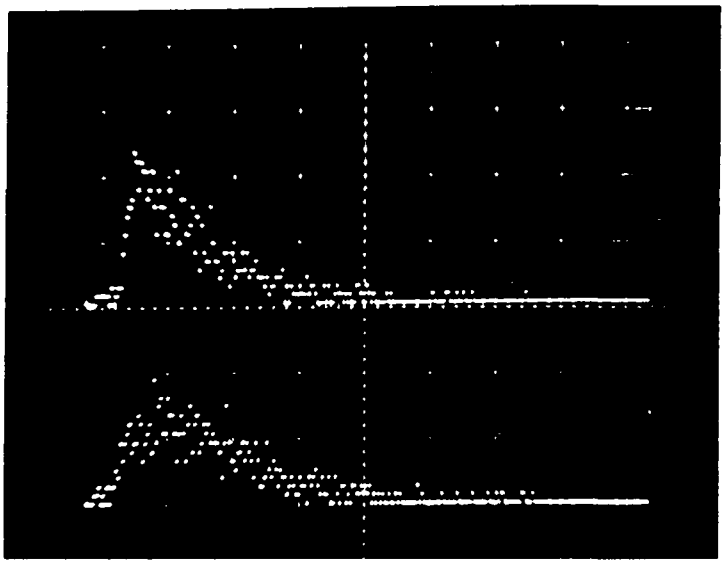

Figure (26)

Signal distribution (with 3-fold coincidence) for,
top - one 125 μ strip of (1.5 mm x 30 mm) size
bottom- one 275 μ strip of (1.5 mm x 30 mm) size

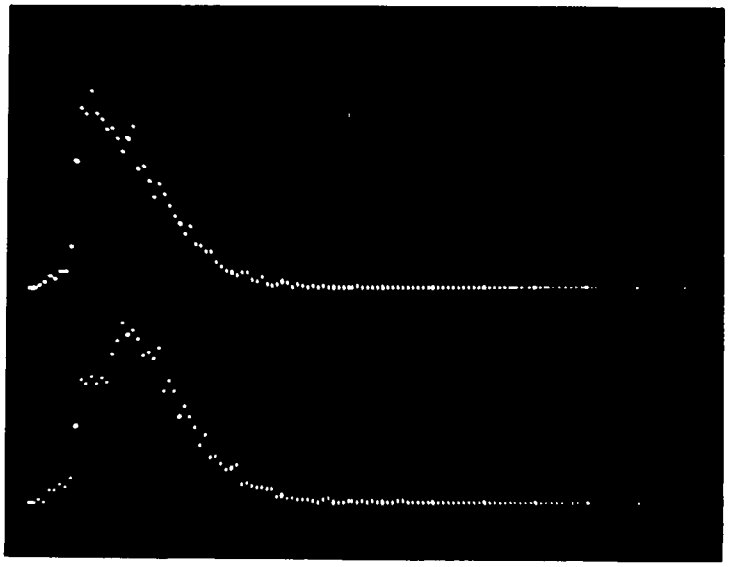

Figure (27)

Signal distribution (with 3-fold coincidence)
Top- one 125 μ strip of (0.8 mm x 20 mm) size
bottom- one 275 μ strip of (0.8 mm x 20 mm) size

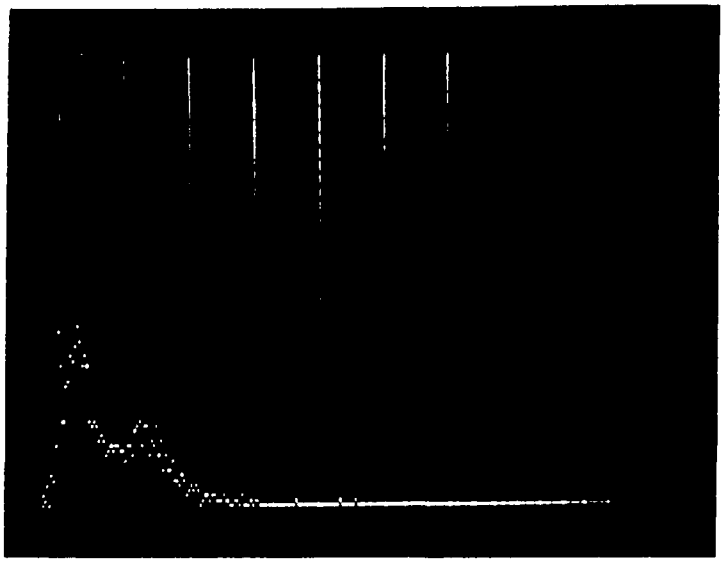

Figure (28)

Signal distribution for 125 μ strip, with S_r^{90} (set to face one of the edges) and 2-fold coincidence.

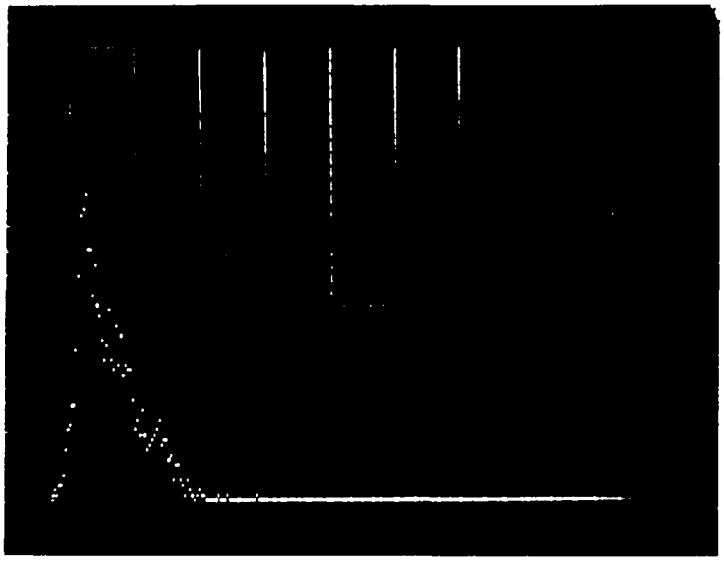

Figure (29)

Signal distribution for 125 μ strip, with Sr^{90} (set to face one of the edges) and 2-fold coincidence.

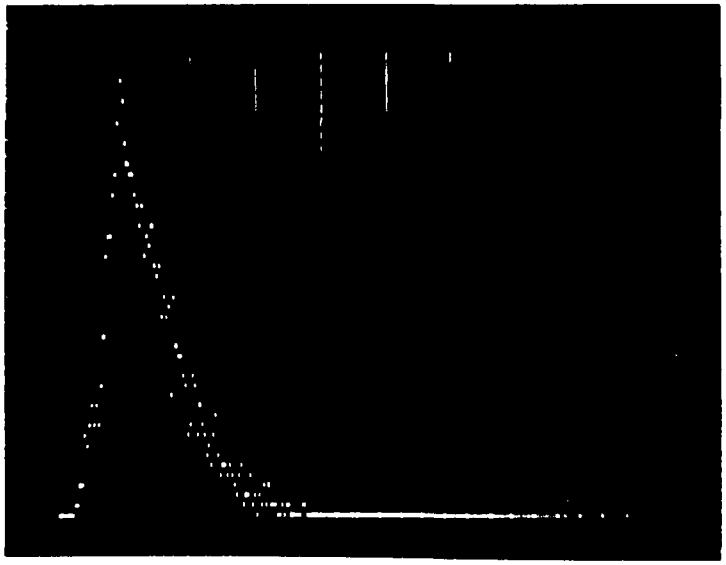

Figure (30)

Signal distribution for a strip of five 125 μ laminations with 2-fold coincidence.

1.3 The microstrip scintillator detector

The detector consists of small strips of thin scintillator coupled to an image intensifier device. Since the strips are thin and relatively small, damages were expected to appear within the scintillators due to the cutting effect by the razor blade. The main damage was from small cracks that developed along the sides of the strips as a result of the applied pressure during cutting. A special technique has been developed to cut the scintillator strips uniformly (without cracks) from a thin sheet (100 microns thick) of NE102 plastic scintillator which has a high light emission (65% of anthracene) and fast time response (2.4 ns). It requires cutting 5 cm long strips with width longer than the length of the microstrip by $\sim$ 1 mm, then taking thin slices between 50 and 100 microns from each side till the width reaches the desired length of the microstrip. The strips are examined under the microscope for cracks and exact width before polishing and final cutting. The polishing process is done by hand and involves using powders of different grain sizes ($10\mu - 0.05\mu$) to polish the edges of each strip. Thereafter, the long strips are cut into small microstrips with a final width of (400–425) microns, by using the same process of taking thin slices from the edges to eliminate any cracks that might be developed near the edges as a result of the cutting.

Two different sizes of the detector were built; the first one with an effective area of (1.2×1.2) cm^2, consists of 115 strips each being 1.4 cm long and (400–425) microns wide, held together by a brass frame as shown in fig. 31. The second one has an effective area of (2.4×2.4) cm^2, consists of 110 strips of 100 micron thickness in the center region of the detector and 23 strips of 250 micron thickness on each side of the central ones. The strips are separated by a thin layer of silicon grease (5–10 microns) to improve the light collection inside the strips and to help in holding the strips togther. A test was done on two sets, each of 30 strips of 100 micron

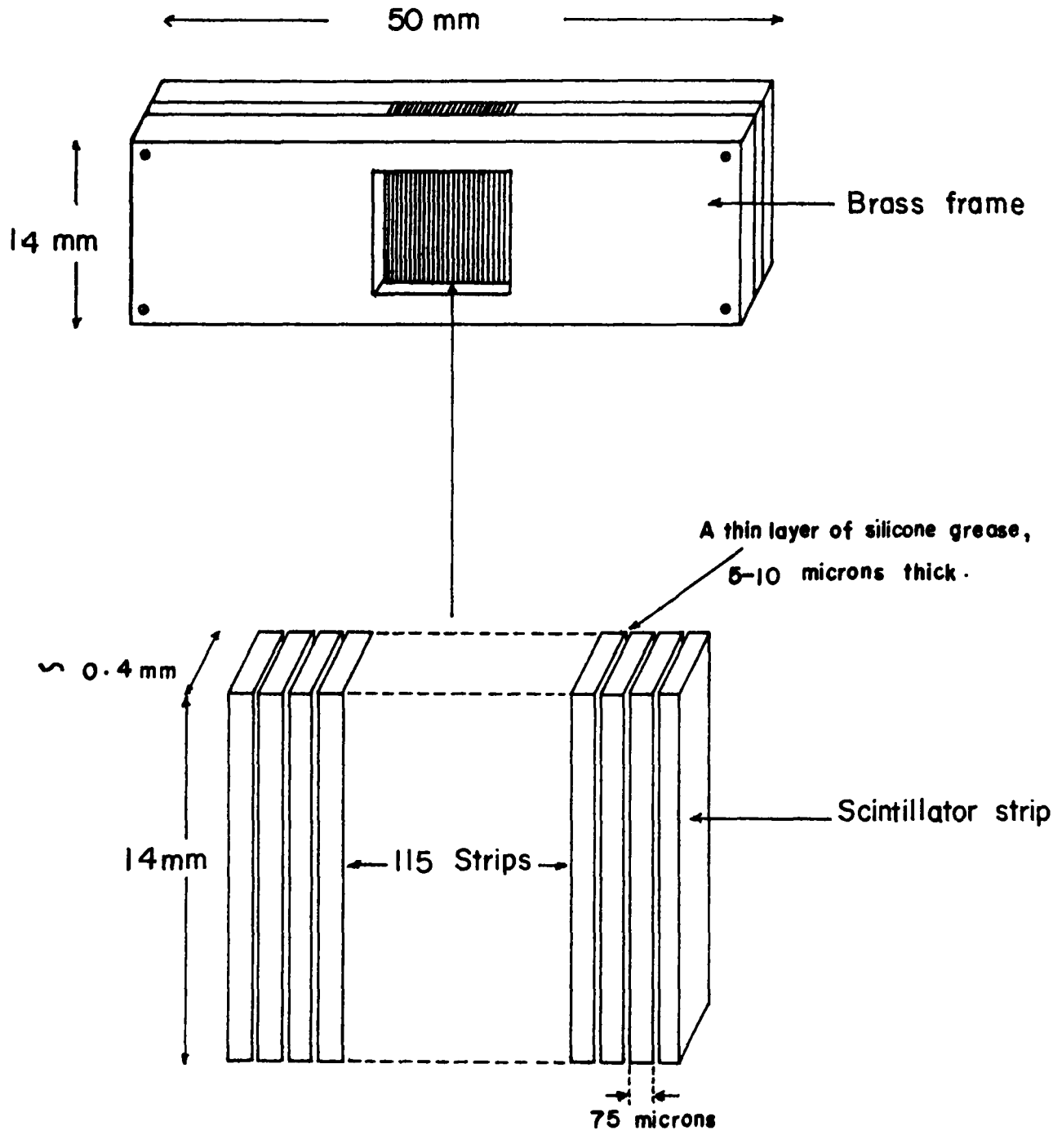

FIGURE (31)

The multistrip detector.

thickness, to see the effect of using silicon grease instead of air gap separation. The light output from the two sets was examined under the microscope, with a converging light spot of 50μ diameter, and it showed a good light collection with the silicone grease present, while most of the light seemed to scatter from the sides of the strips with the air separation.

The light transmitted from each strip was collected and transferred separately to the image tube by a coherent fiber optic ribbon (manufactured by Schott Fiber Optics) [19] ; it is 60 cm long, 15 mm wide, and 0.5 mm thick, and consists of small clad fibers each of 10 microns diameter. The ends of the ribbon are finely polished with very few defective fibers. The light signals transmitted from the scintillator strips, through the fiber optic ribbon, were detected by a new type of imaging instrument. It combines the advantage of the high gain- low noise microchannel plate device with the high sensitivity of the solid- state self- scanned array image sensor. The basic subassemblies of this instrument are:

– High gain proximity-focused microchannel plate image intensifier tube (CIT) for image preamplification,

– Self-scanned array (SSA) for electronic readout of the image,

– A video signal electronics system for the SSA.

The microchannel plate device is an ITT proximity-focused channel intensifier tube (F4145); a schematic diagram of the tube is shown in fig. 32. It consists of an input window, photocathode, dual MCP, phosphor screen and fiber optics output window. The fiber optics input window is 5 mm thick , made of small fibers each of 6 microns diameter, providing a high resolution for the input light signals. The high gain in the channel intensifier tube (CIT) is achieved by using a (V- shape) microchannel plate [20-22], which is composed of two MCP's placed in face- to- face contact (with each channel in the first MCP opened to three channels in the second one) in such a way that ion-feedback to the cathode is greatly reduced and the gain

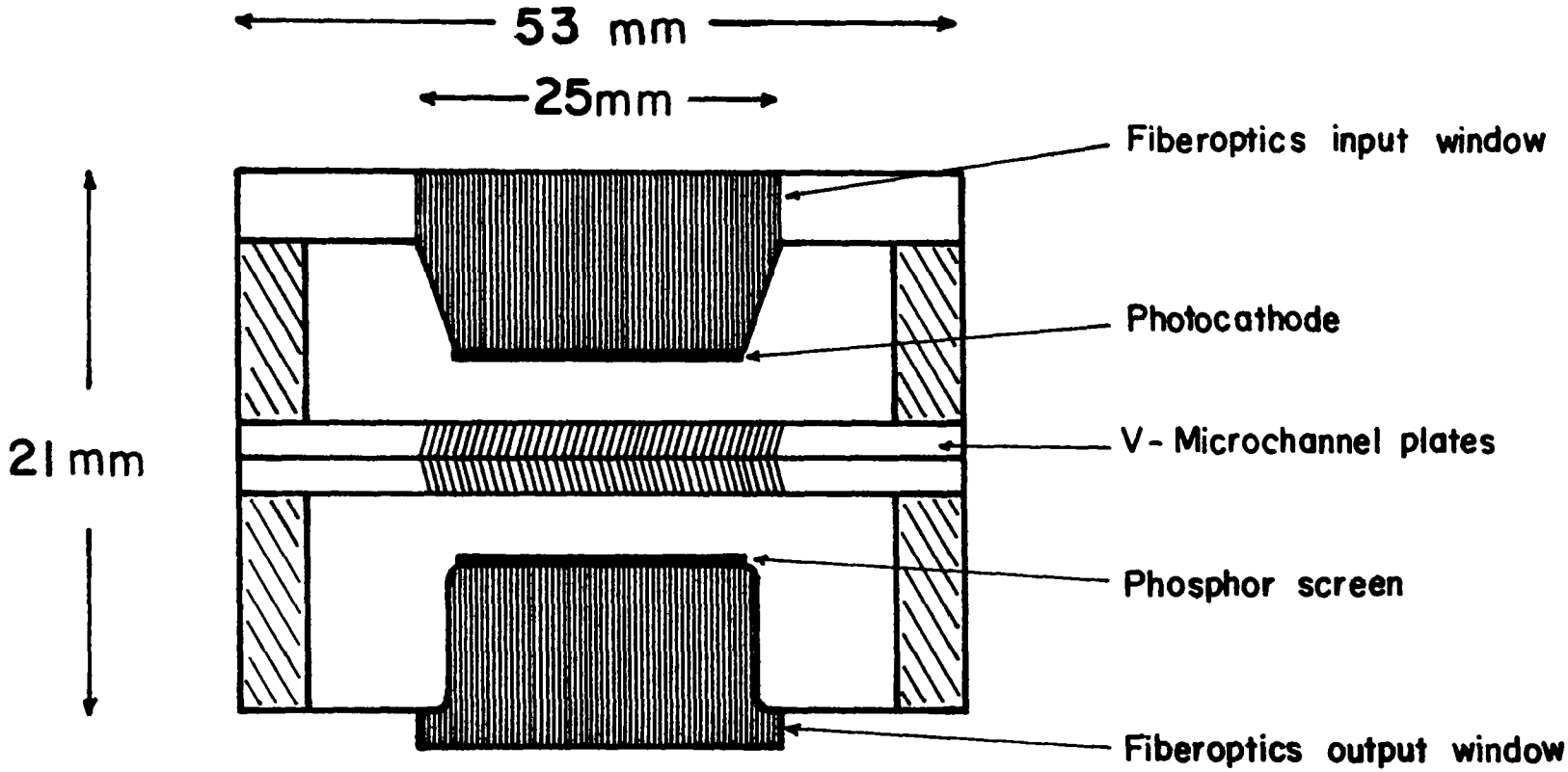

FIGURE (32)

Proximity focused channel intensifier tube.

increased. Each MCP consists of many small channels ($5.1 \times 10^5 channels/cm^2$) each of 12.5 micron diameter and 0.5 mm long with a bias cut angle of 5 degrees. In order to protect the photocathode, the MCP is covered with an ultra- thin, electron- penetrable, but ion- trapping, input film over the input MCP face. This ion- trap extends the useful life of the associated photocathode by two or more orders of magnitude. The VMCP provides a peaked differential gain pulsed height distribution which allows the use of threshold detection techniques in the video circuits. One important operating property of the MCP, is that the output currents are saturated, without charge spill-over into the broad surrounding areas of the image, so that localized bright objects within the field-of-view do not destroy the image over a large area.

The phosphor screen of the high gain (CIT) is chosen so that it has a short decay time (to prevent pulse pile- up during the readout per exposure period), and a spectral response within the high sensitivity region of the linear self- scanned image sensor. A (P-20) phosphor is used which has a (60–500) μ sec decay time (to 10%) which depends on the input current, and a 14% quantum efficiency at 560 nm. The phosphor screen is covered with a thin layer of aluminum to reflect the induced light signals into the output window. The output light produced by the phosphor screen is fiber optically coupled out of the tube, into the image sensor, by a coherent fiber optics window. It is 5 mm thick (similar to the input window), consists of small fibers each of 6 microns diameter.

One important characteristic of the channel intensifier tube is that it can be electronically gated in periods as short as about 5 ns to cut off noise caused by the thermionic emission from the photocathode. To achieve a maximum electron gain of 10^8 , two ITT tubes (F4145) were coupled together through an optical system consisting of two 50mm Pentax lenses (f/no =1.4) coupled directly to each other to achieve 1:1 image magnification. The photocathode and the phosphor screen

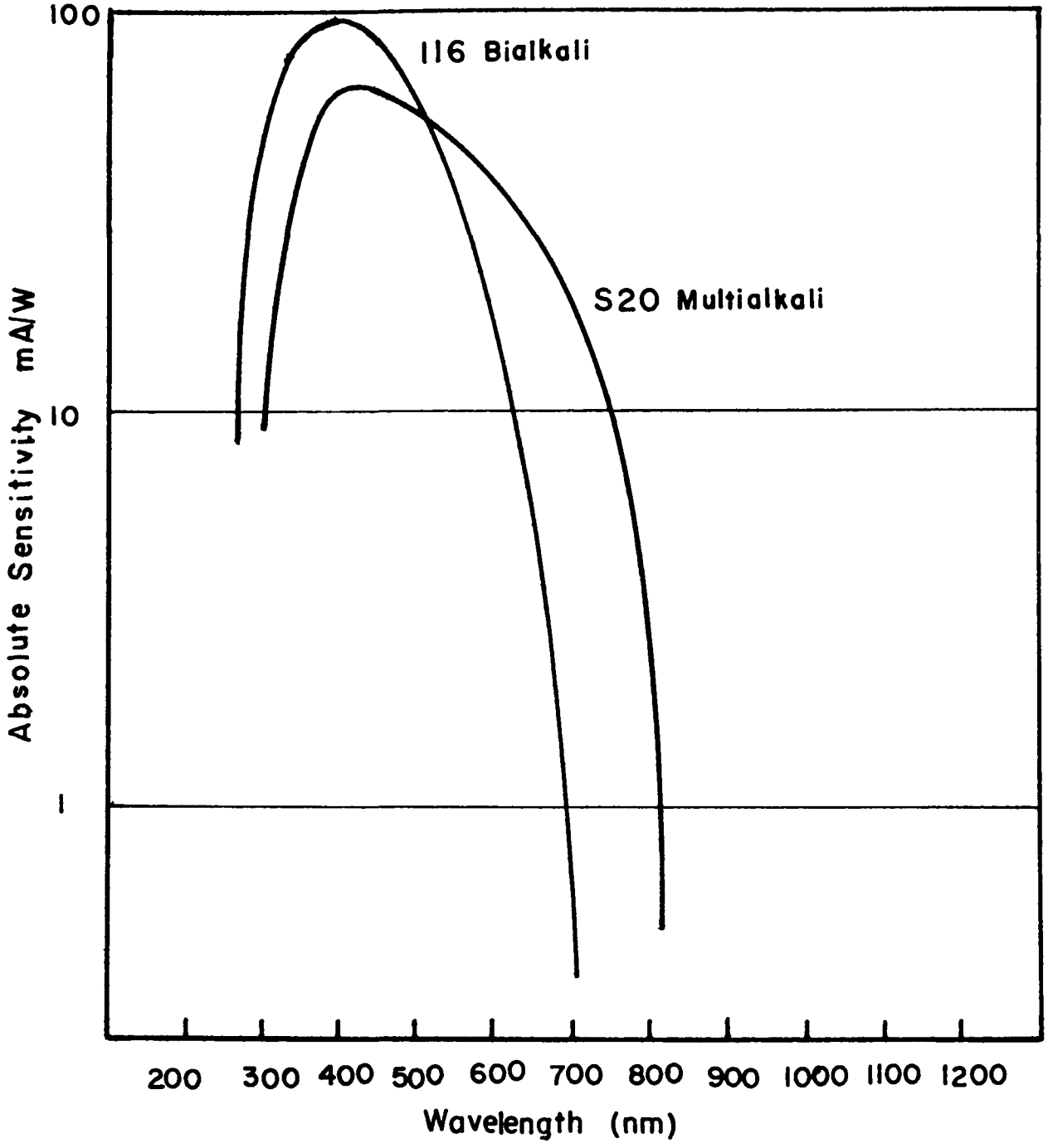

FIGURE (33)
The spectral response of ITT tubes photocathode.

used in the two tubes have been chosen to give the best detecting efficiency for the input and the output signals. The front tube, where the scintillators are coupled, has a bialkali photocathode of maximum quantum efficiency at the region of 425 nm (figure 33), which represents the peak emission of NE102 plastic scintillator, and (P–20) phosphor with peak emission at 560 nm (figure 34). The second tube has a multialkali (S20) photocathode which has maximum efficiency at 450 nm and high output current around 320μ amp/l. The phosphor screen of the second tube is made of (P–20 red) phosphor with peak emission at 650 nm falling within the region of maximum sensitivity of the silicon diodes.

To have an electronic readout of the image signals, the tube is coupled to the linear self- scanned array (SSA) image sensor through a coherent fiber optic ribbon for the optimum tube to SSA image transfer efficiency. The solid state (SSA'S) are high density monolithic linear arrays of silicon photodiodes with integrated scanning circuits for serial readout. In operation, a solid state image sensor converts incident light to electric charge which is integrated and stored until readout. The integrated charge is directly proportional to the intensity of the light impinging on the sensing elements. The charge information is then sequentially read out at a rate determined by pulses applied to the image sensor. The array used with the (CIT) was a Reticon RL256EC/17 linear array. It consists of 256 sensors on 50 micron centers and 425 micron aperture with a total chip size of $(2.3 \times 0.76)\ cm^2$. Sixteen of these arrays were used for the readout of the image signals from the different detectors. The diodes were purchased with plain unattached windows and a special technique has been developed to fit a specially made fiber optics windows (by Schott Fiber Optics) on each diode (appendix B). The detector assembly of an image intensified linear self-scanned array instrument is shown schematically in figure 35. In operation, the input optical image is focused onto the photocathode of the image intensifier tube, and the resulting photoelectrons are accelerated into the microchannel plate by an

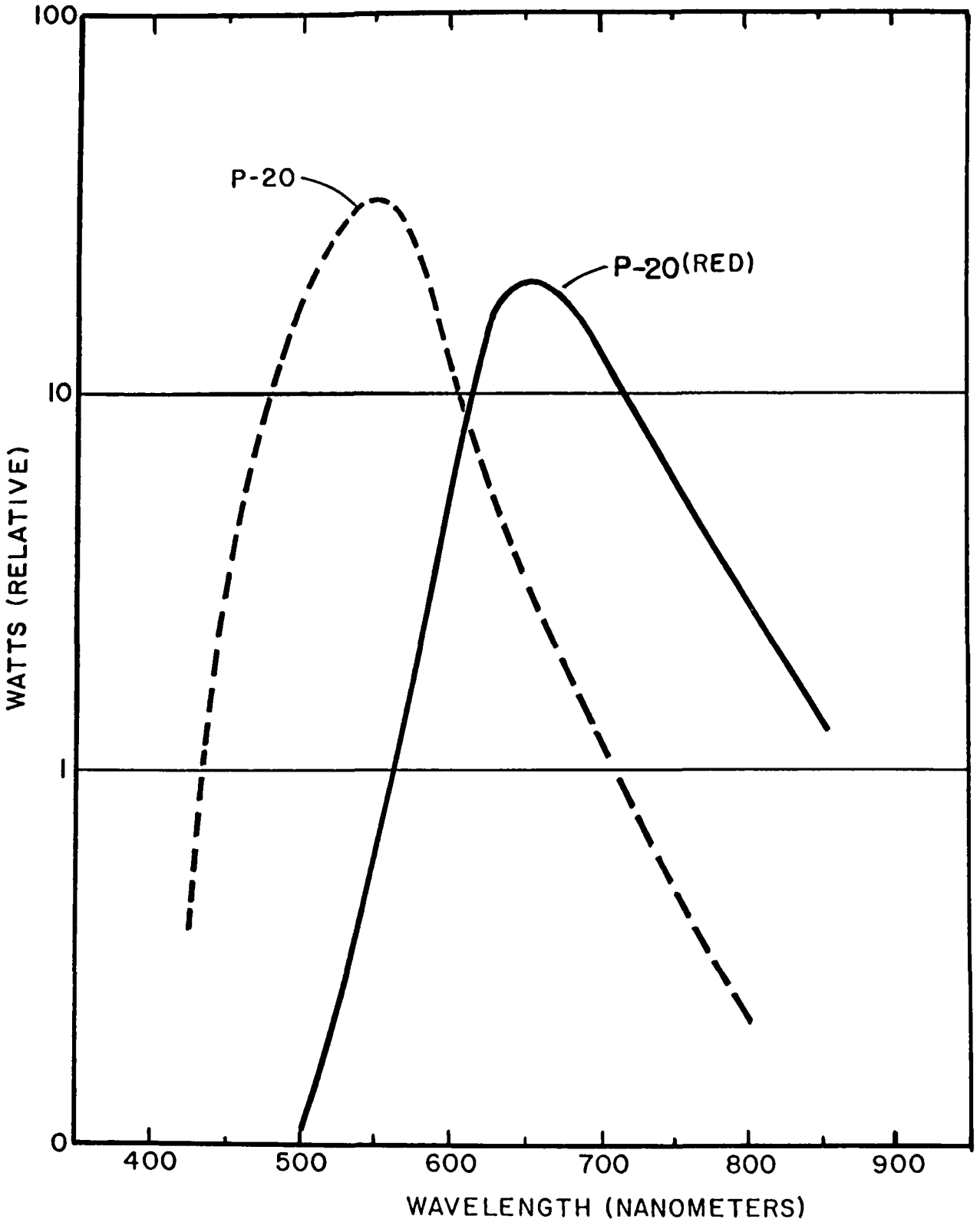

FIGURE (34)

The spectral response of P-20 phosphor.

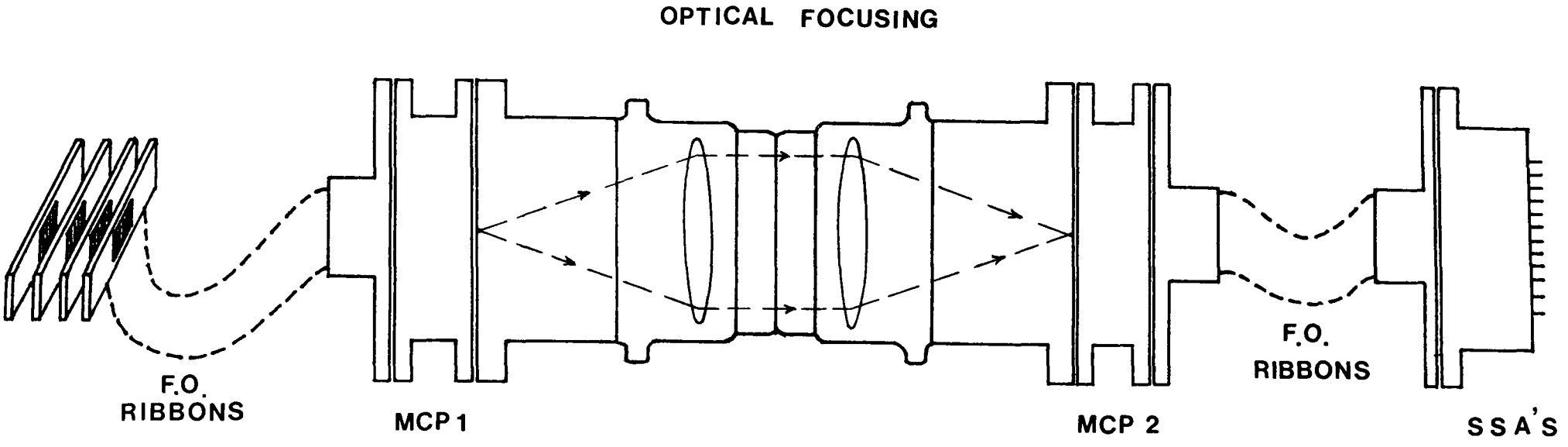

FIGURE (35)

The assembly of the multistrip scintillating detector.

applied voltage of 180 V. The input signal current is amplified a factor ($G = 1 \times 10^5$), for each tube, by application of a potential of 1500 V across the VMCP (see appendix C for detail measurement of gain model). When the electrons leave the VMCP, they are accelerated in the last stage by an applied potential of 6000 V, and strike the phosphor screen. The electronically induced output light from the screen is fiber optically coupled into the linear SSA. An output electronic signal is derived from the individual pixels in the SSA by connecting the SSA to an electronic circuit which provides the necessary drive pulses and which contains a charge amplifier circuit. A block diagram of the complete data recording and display system used with the digital image tube is shown in fig.36.

1.4 Experimental test and performance

To test the performance of the detector in reconstructing the events of in teractions and localizing its vertices within the target, an experiment at Lawrence Berkeley Laboratory was conducted using an Ar^{40} beam with 1.5 Gev/nucleon, on an emulsion target. Figure (37) shows the experimental set-up used. It consists of,

–a telescope of scintillating counters.

–mobile targets.

–microstrips scintillating detectors for tagging and vertex detection.

The telescope consisted of five scintillating counters, S_1 and S_2 each of an area $(5 \times 5)cm^2$, S_3 and S_5 $(10 \times 10)cm^2$, and S_4 has an area of $(3 \times 3)cm^2$ which has been used as a veto. The counters provide the needed information on the total beam flux , detect the shower particles from the primary and secondary vertices, and give the triggering signal for the readout system to start taking data on the selected events. Each counter was coupled to an amplifier circuit, discriminator unit to set the proper threshold for incoming signals, and to a coincidence module. All these

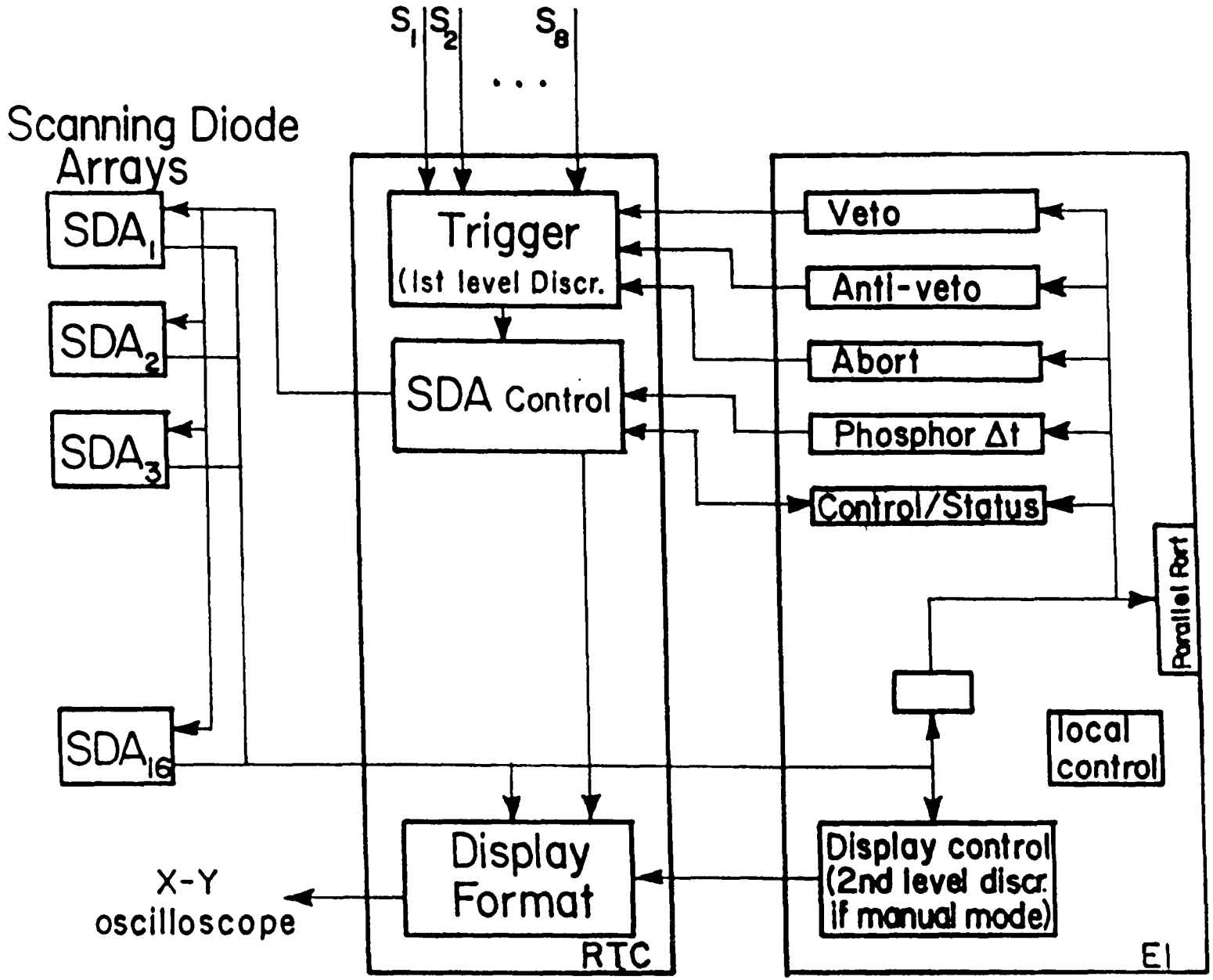

FIGURE(36)

Block diagram of data recording and display system.

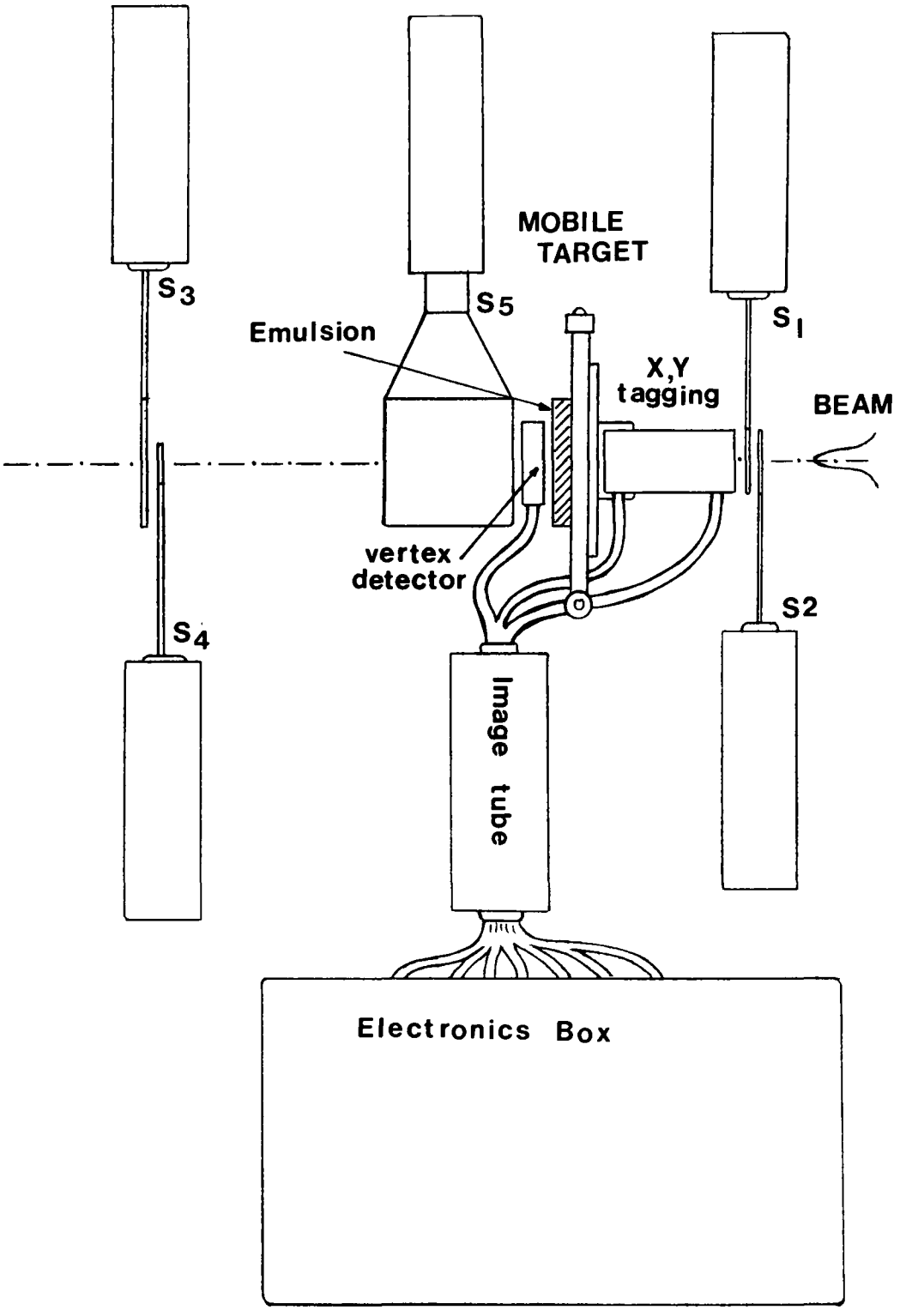

FIGURE (37)

The experimental set-up used to test multistrip detector at Berkeley.

electronic units have a very fast response time (within 10 ns). S_1, S_2 and S_3 were used in coincidence to give the total number of beam particles passing through the target and the detector. S_1, S_2, S_3 and the veto S_4 were used in coincidence to supply the triggering signal for the readout system. The use of the veto was to choose the events that involve a central collision only where no shower particles appear within a forward cone of six degrees. S_5 was used to give the total number of the wide angle shower particles coming from the primary or the secondary vertices. To obtain a more uniform exposure and to make full use of the volume of the emulsion stack, relative to the small area of the vertex detector $(2.4 \times 2.4)cm^2$, a mobile target with X–Y motion is needed. For that, a microscope stage with stepped- motors on both axes was used. A control unit with 8748 microcontroller was built to command the motion of the mobile target and keep a record of the position at all times. Also, it could output the information to the main computer through an RS-232 serial line. Three modules of emulsion were used. One vertical, $(10 \times 10 \times 0.6)cm^3$ in volume, consists of ten plates, each 600 microns in thickness, and two horizontal modules, each $(10 \times 10 \times 2)cm^3$ in volume, consisting of 123 plates each $(10 \times 2 \times 0.06)cm^3$ set horizontally with respect to its width of 2 cm in the beam direction.

Four microstrip scintillating detectors (figure 38), were set in front of the emulsion target to tag the events. Each detector has an effective area of $(1.2 \times 1.2)cm^2$ and consists of 115 strips each of 100 micron thickness. They determine the X and Y coordinates of the projectile nucleus, and they can be added with the X–Y coordinates of the mobile target drive to give the actual postion where the interaction should be found in the emulsion (within the resolution of the detector).

The vertex detector, which locates the vertices in the emulsion target, is made of six microstrip scintillating detectors. Each has an effective area of $(2.4 \times 2.4)cm^2$. The central region of each detector consists of 110 strips of 100 micron thickness

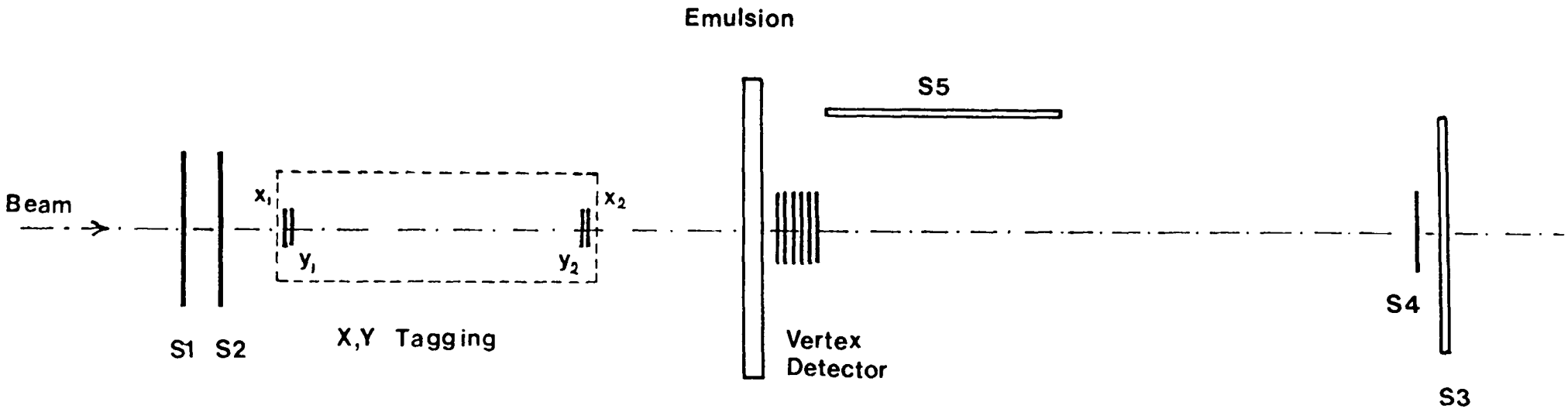

FIGURE (38)

Side view of Berkeley set-up shows the location of the tagging system and the vertex detector relative to the emulsion target.

Scale 2:1

5 Cm

and 23 strips, on each side, of 250 micron thickness.

All microstrip detectors (for tagging and vertex detection) were coupled to the imaging tube, for image amplification, through fiber optics ribbons. The final image was read , through the same kind of ribbon, by self-scanned array diodes. Sixteen of these diodes were used to detect the light signals emitted from each scintillating strip. A control unit based on the 6809 microprocessor was built to read the data from the diode arrays and control its transfer to the main computer.

Figures (39 and 40) show the Bevatron /Bevalac experimental area and beam-line 40 area, respectively.

The experiment was performed from midnight July 19th, 1984 to 4.00 am. The beam cycle was two seconds spill every six seconds period, ten times per minute. The flux per beam spill was varying between 100–1000 ions. At the end of the run, the total flux was in the excess of 100000, and 4000 events were tagged in the emulsion stack.

During the running period of the experiment, it was obvious that four out of the sixteen diodes were not functioning properly, which was indicated in the output data on the on-line screen. Although the diodes were checked and adjusted for the right threshold and sensitivity a few hours prior to the experiment, many diodes showed fluctuations in the output signals which might be related to heating effects or humidity condensation build-up. Another major mishap, discovered the following day, involved the coupling between the imaging tube and the fiber optics ribbon that transfers the light signals to the diodes. A gap of $\sim$ 1 mm was present in-between, caused by the shortness and the heavy weight of the ribbon, which caused the defocusing in the images received by the diodes and total loss of resolution. After analyzing the collected data, it was obvious that the registered information from the vertex detector was not reliable enough to provide a systematic search for secondary vertices. Figure (41 and 42) show a sample of the data recorded by the

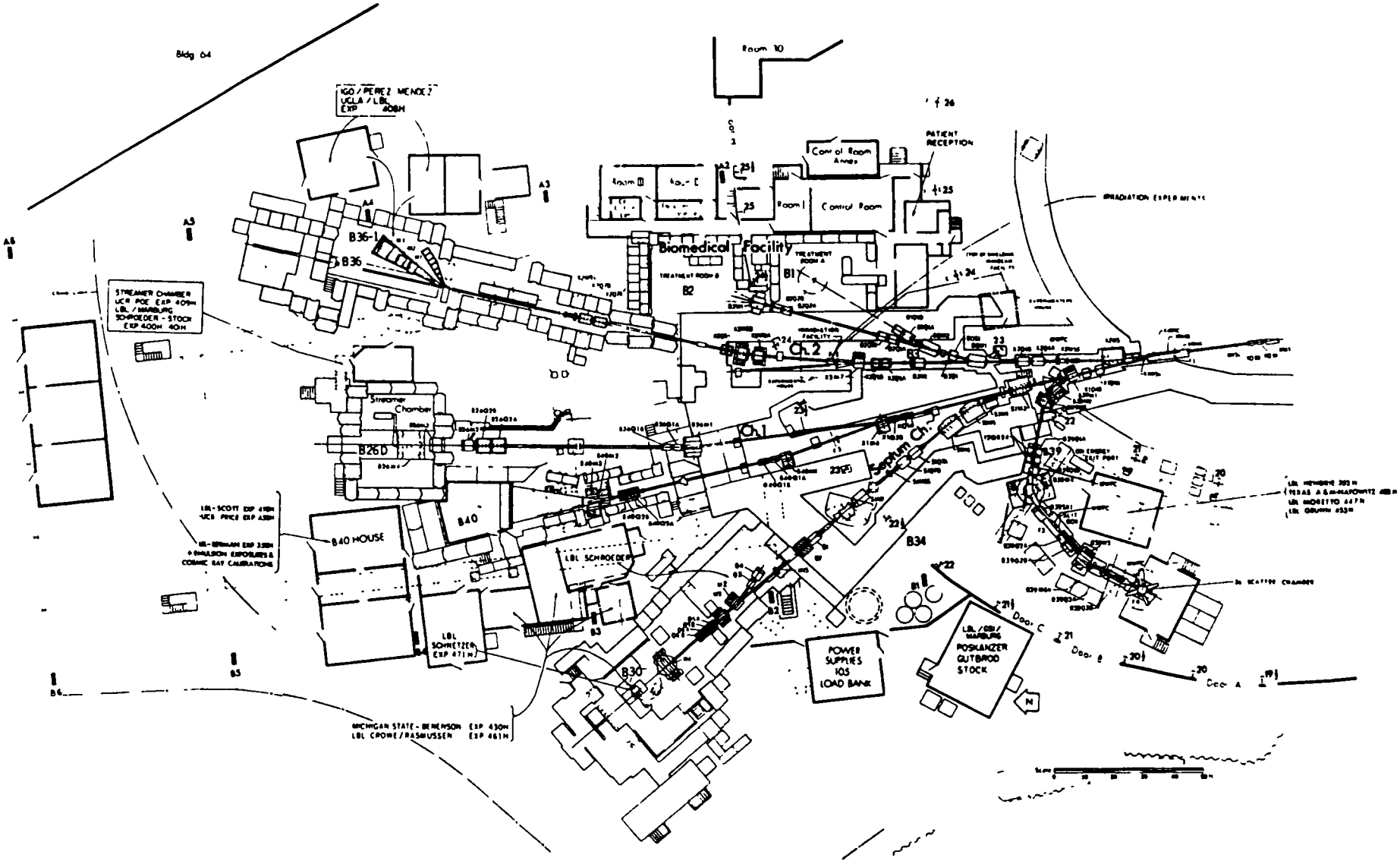

FIGURE (39)

Bevatron/Bevalac plan site.

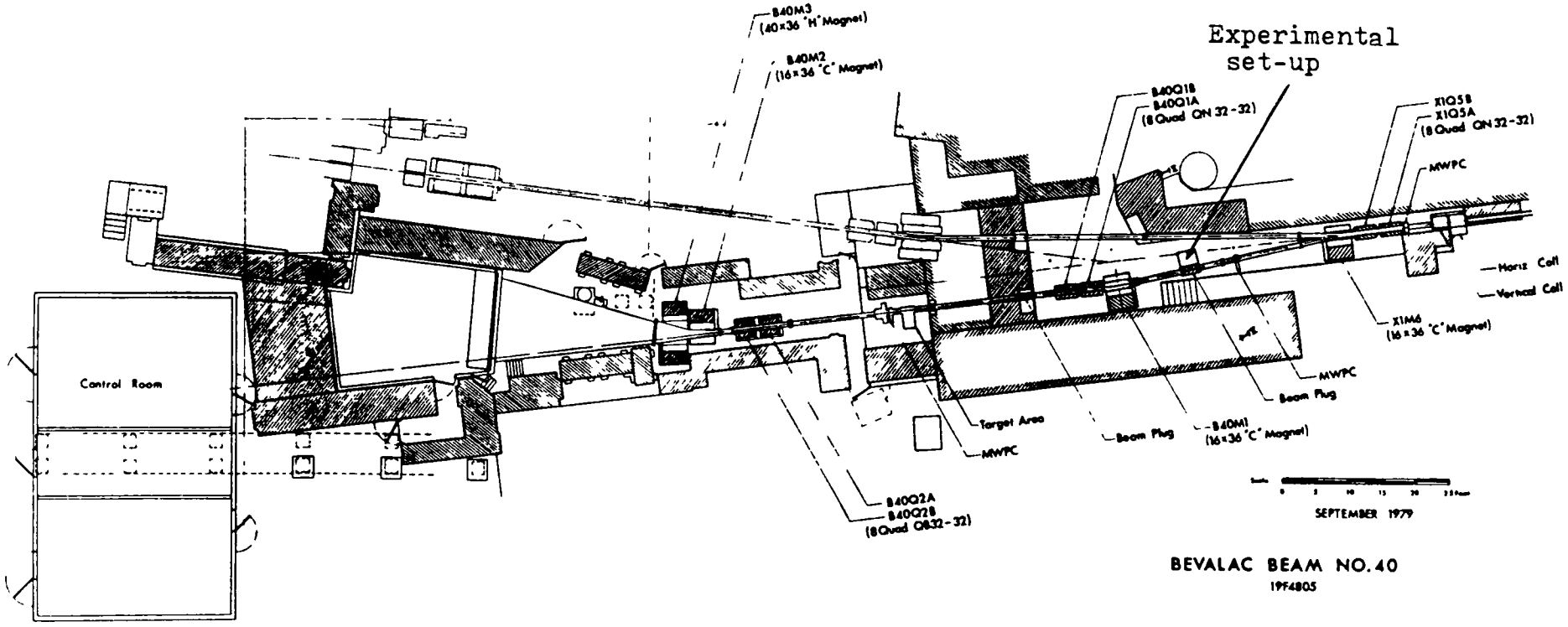

FIGURE (40)

Beam line 40 and the experimental area.

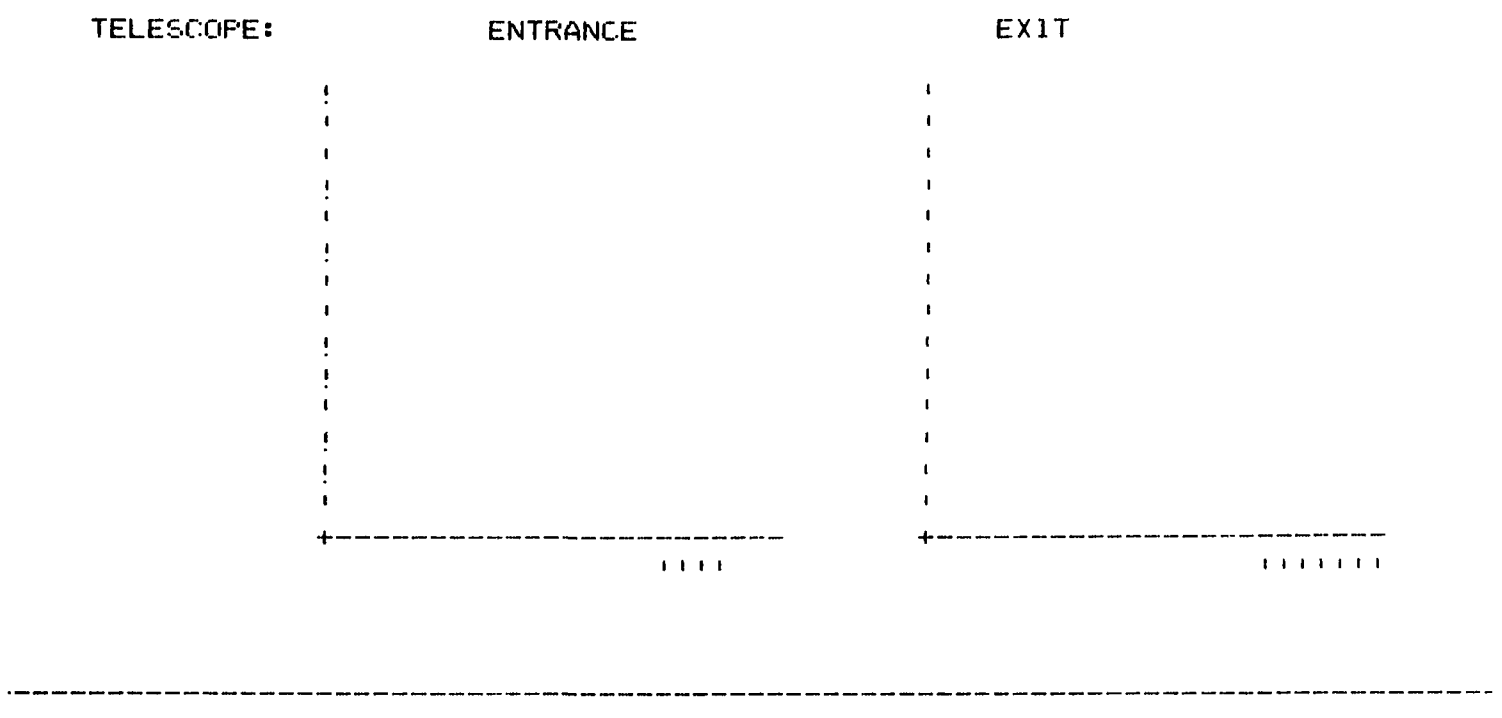

FIGURE (41)

Event #14 recorded by the vertex detector and found in the emulsion.

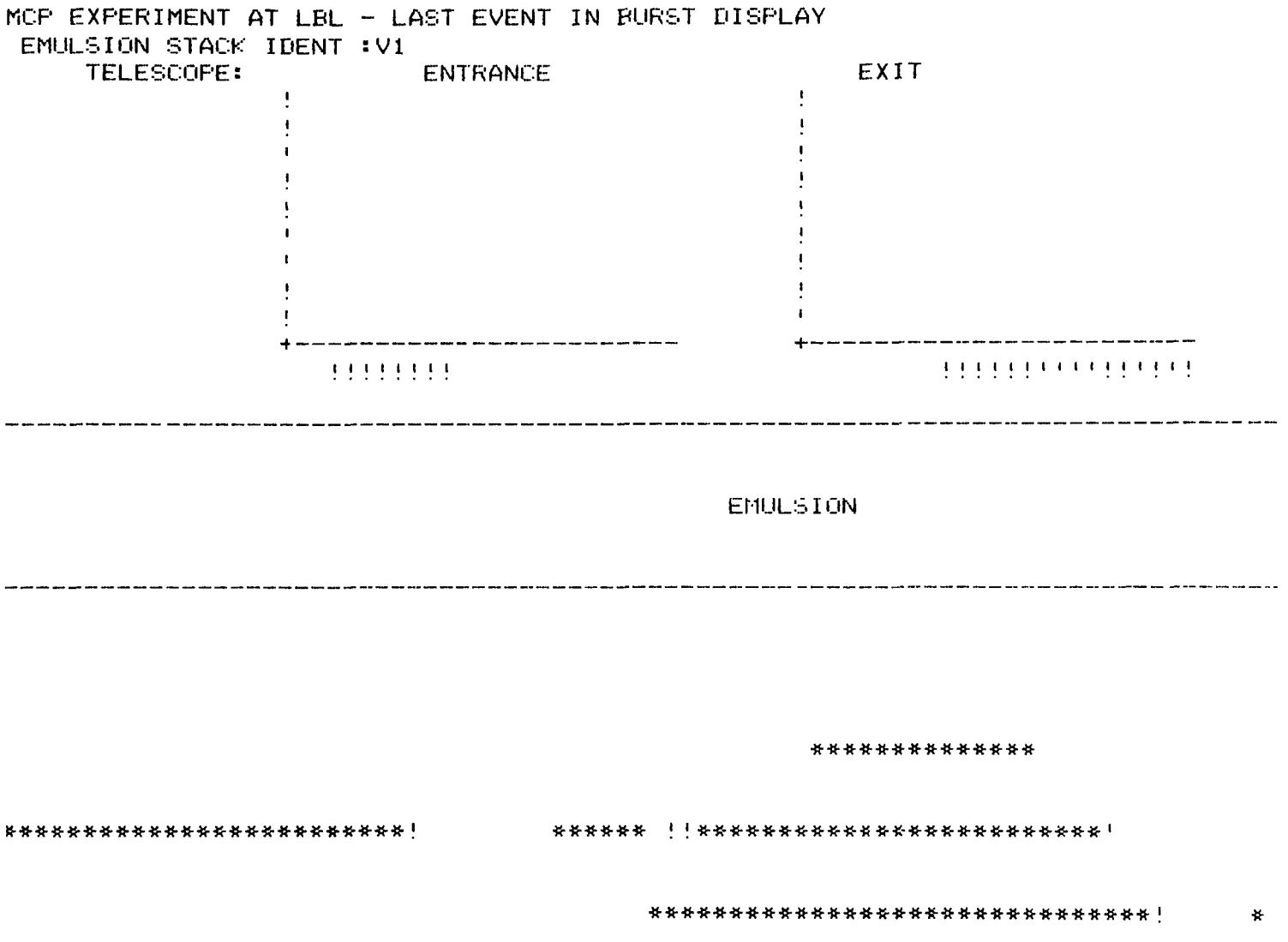

FIGURE (42)

Event #90 recorded by the vertex detector and found in the emulsion.

vertex detector for two events that have been found in the emulsion. The detection efficiency of the detector was estimated to be around 40% from the available data, and since the optical coupling between the image tube and the ribbon was poor, it is difficult to estimate the resolution of the detector although it was expected to be around 200 microns (considering the thickness of the scintillating microstrip, of 125μ, and the overall resolution of the imaging tubes, which is around 40μ for each tube).

Chapter 2

Scintillating Fiber Optics Detector

2.1 Introdution

The pioneering work on scintillating fibers and its possible use in detectors for elementary particle physics was performed during the late 1950's and early 1960's by Reynolds [23] and Ginther [24] in the United States, and independently by Anderson [25] in the United Kingdom, and by other groups [26–30]. Their work was limited by the then existing technology in fiber production techniques, image intensification, detector arrays, and computers. Recently, with the improvement of capabilities in these technologies, there has been a renewed interest in both cosmic rays [31–34] and high energy physics for the development of large arrays of both glass and plastic scintillating fiber detectors for electromagnetic calorimetry [35,36] and tracking applications [37–41].

Although plastic scintillating fibers are characterized by fast fluorescence time (few nanoseconds) , high efficiency (40%–80% that of anthracene), and long attenuation length ($\sim$ 2m), they do not fill the requirement on spatial accuracy which sets a natural upper limit of $\sim$ 25 microns for the fiber diameter, since narrow fibers would lose nearly 80% of its scintillation light because of insufficient trapping. However,

glass fibers possess the features of radiation hardness and the ability to be drawn into cladd fibers of very small cross-section ($\geq$ 5 microns), which make them competitive material for the fabrication of high spatial resolution vertex and tracking detector.

2.2 Characteristics And Properties

Among the various scintillating glasses which have been developed, cerium-doped and terbium-doped glasses are the most common. To date, cerium glass is the most widely used in active target experiments and in tracking applications for its fast decay time which makes it suitable for high interaction rate experiments. A detailed study of the characteristics and performance of cerium glass has been done by different groups [42–46] within the past few years. On the negative side, the studies show that the cerium glass has poor quantum efficiency (up to 4% depending on composition), poor attenuation length (22 $\pm$ 5 mm) and poor trapping efficiency within the fibers (3% only). Terbium-doped glass is also characterized by shortness in the radiation length (25 $\pm$ 5mm), but it has higher quantum efficiency (10%) compared with the cerium glass.

One of the disadvantages that limits the use of the terbium-doped glass is the long decay time (2-3 msec) which makes it suitable only for fixed target experiments with low flux beams. This limitation will not have a great impact if the readout system used has a long delay time, as is the case for our system where we use a CCD video camera with (30 Hz) recording rate.

From this perspective and since the terbium glass has a higher yield factor, it was suitable to use it as the detecting elements in the construction of a vertex detector.

All samples that have been used to test the properties of the terbium glass and

the ones used to build the vertex detector were supplied by Schott Fiber Optics [19].

Different tests have been conducted to study the different properties of such type of glass. The properties studied, included:

1–Absorption spectrum.

2–Emission spectrum.

3–Fluorescence decay time.

2.2.1 Absorption Spectrum

The set-up used to study the absorption spectrum consisted of a high pressure xenon arc lamp, a SPEX grating monochromator which has adjustable scanning range (depending on the grating used), and an Ealing silicon diode detector. The xenon lamp and the monochromator were used together to supply light beams at different wavelengths in the range between 300 nm to 750 nm. A voltmeter was used to record the output signals from the silicon detector. A block of terbium-doped scintillating fiber optics glass was used. It has the dimensions of $(1 \times 1)cm^2$ by 2.5 cm long, and consists of thin fibers each 20 microns in diameter and 2.5 cm long. The block was coupled directly to the silicon detector through one of the polished ends. The other end was set in front of the exit slit of the monochromator which has been adjusted to give a light beam of 1 mm width. With no sample on the detector, the light intensities between 300 nm and 750 nm were recorded to establish reference points for calibration. The same procedure was repeated with the sample coupled to the detector. The difference in the light intensities from the two cases represent the total absorption spectrum of the terbium-doped glass. Figure (43a) shows the final absorption curve which indicates very clearly the region of the maximum absorption (in the UV region around 380 nm).

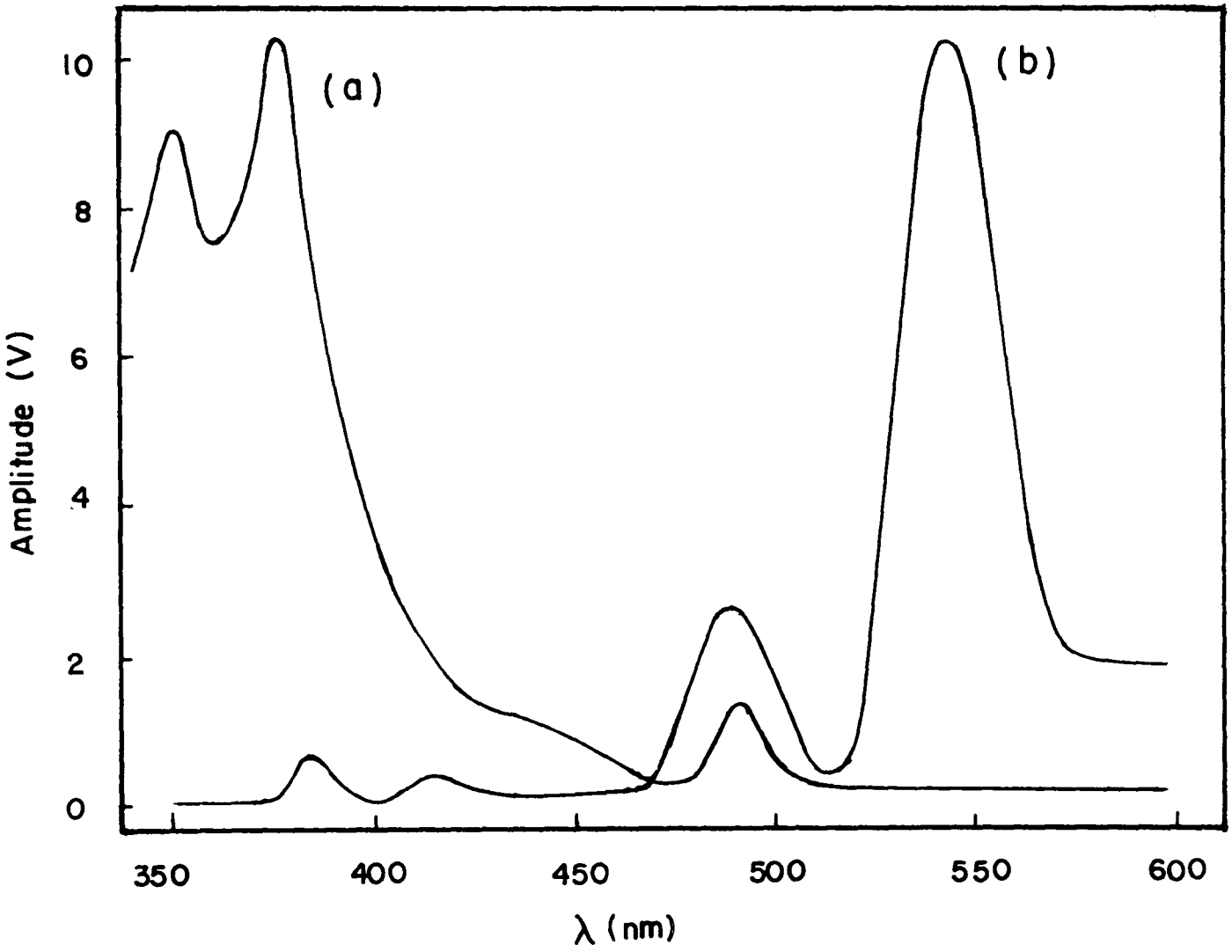

FIGURE (43)

a--The absorption spectrum of Tb_2O_3 glass.
b- The emission spectrum of Tb_2O_3 glass.

2.2.2 Emission Spectrum

The spectral emission of the terbium-doped glass was measured using the same block of scintillating fibers coupled to the entrance slit of a (ZEISS) prism monochromator which has a range between 300 nm and 800 nm. A Hamamatsu photomultiplier tube (R928), which has a multialkali photocathode, was used to detect the emitted light from the glass sample through the exit slit of the monochromator. Since the maximum absorption of the terbium-glass is in the UV region, a nitrogen-pumped dye-laser was used to excite the glass sample with a 337 nm light pulse of 10 ns width. The laser pulses were focused on the sample with a spot size of 5 mm in diameter passing through the fibers along the 2.5 cm length of the sample. With the nitrogen laser pulsing at 10 pulses/sec, the light output from the monochromator was scanned between the region of 300 nm to 750 nm with and without the glass sample mounted. In each case, the opening of the input slit of the monochromator was adjusted to give the same light intensity at the output for 470 nm wavelength (where both absorption and emission are minimum).

The emission spectrum shown in figure (43b) was deduced from the difference in the intensity of the transmitted light from the two cases. The graph shows a strong emission peak in the green region around 540 nm which is well separated from the absorption peak. This is quite different from the case of the cerium glass where the absorption and emission spectra overlap each other causing some internal absorption of the emitted light which leads to a poor quantum efficiency. To ensure that the emission spectrum found was generated by the terbium contained in the fibers and not from other elements in the glass, three samples of bulk glass each of $(2.5 \times 2.5 \times 1) cm^3$, were tested with the same set-up and under the same conditions. One sample consisted of all the basic elements used in the scintillating glass fibers but has no terbium in it, the other two samples are doped with terbium in different percentages. One has 10% by weight Tb_2O_3 and the other has 5.6% by weight

Tb_2O_3. Figure (44) shows the emission spectra from the three samples which shows without a doubt that the strong emission peak around 540 nm is caused by the terbium contained in the sample.

From the graph, one can notice that increasing the amount of the terbium in the glass from 5.6% to 10% increases the light output at the maximum emission peak by only 22%. This is probably due to a saturation effect within the fibers.

2.2.3 Fluorescence decay time

One of the main characteristics of the scintillating glass fibers, which has to be considered in building a detector from such materials, is the decay time of the scintillating process within the fibers, since it limits the response time of the detector.

The set-up used to measure the decay time of the terbium-doped glass consists of a block of scintillating glass fibers, a Hamamatsu (R928) photomultiplier tube, a Hewlett-Packard (1744A) storage scope, and a (VSL) nitrogen-pumped dye-laser. The scintillating block was coupled directly to the PMT and was masked from stray lights except for a pinhole opening in the front, left for the laser pulses to pass through the length of the sample. The signals received on the storage scope from the PMT indicate that the fluorescence decay time of the terbium glass from initial brightness to 10% decay point was approximately (3–5) msec.

The previous tests indicate that the terbium-doped glass is a scintillator which has several unusual properties compared with the conventional plastic and liquid scintillators. The emission spectrum is concentrated primarily in a yellow-green region at 545 nm. This means that it should be possible to propagate the scintillation light over long distances in light-guides or the material itself without the attenuation characteristic of blue-light transmission. Unlike plastic and liquid scintillators, in which the excitation and emission spectra are overlapping, the terbium glass has

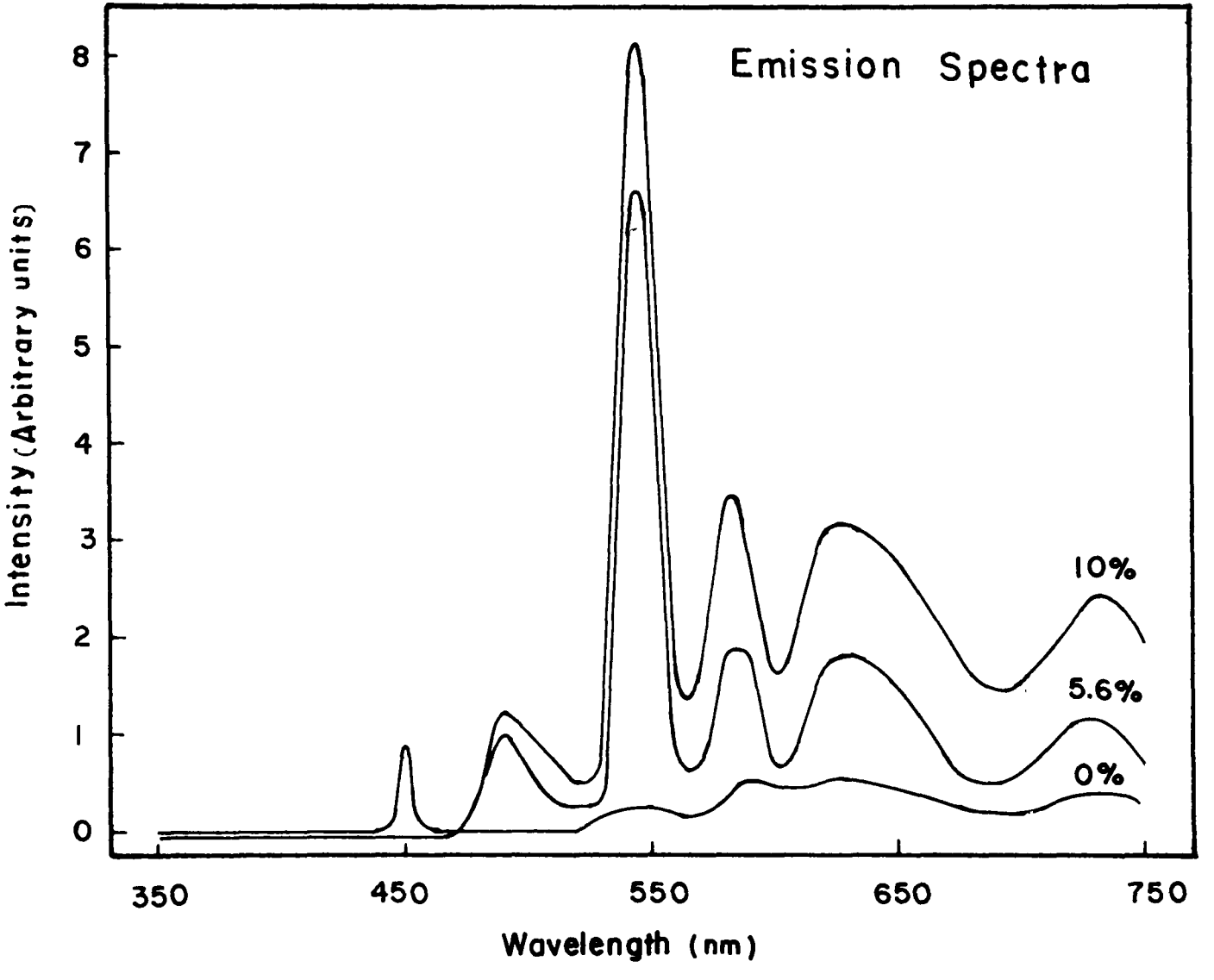

FIGURE (44)

Emission spectra for three samples with different concentrations of Tb_2O_3 .

well separated excitation and emission spectra.

The characteristic time constant for fluorescence in the glass is slow (3–5 ms) which makes the material unsuitable for high interaction rate experiments. However, this should not be a problem for experiments with high-energy e^+e^- colliders whose duty factor of effective interaction rate is low, and for fixed target experiments with low flux beams. Similar results were found by Ruchti et al. [47,48] in his study on small samples of terbium glass.

2.3 Detector Assembly

The first prototype of the scintillating fiber detector consisted of three main parts:

1– Scintillating glass fiber assembly, as the detecting elements.

2– Image intensifier system for image amplification.

3– CCD video camera, for image recording.

The glass assembly consists of 10 wafers of scintillating glass fibers (made by Schott Fiber Optics). Each wafer is $(1.5 \times 2.5) cm^2$ and 0.5 mm thick, made of small fibers each of 20 micron size. The fibers have square cross-sections and are stacked into a square matrix of (10×10) fibers (fig. 45). Individual fibers consist of a glass core, a glass cladding, and a thin layer of light absorbing material on the outer surfaces of the cladding called extramural absorber (EMA).

The glass core is composed of: SiO_2 ,K_2O ,Li_2O ,BaO and 10% by weight of Tb_2O_3. (The exact percentages of the different elements are considered proprietory by the manufacturer). As for the cladding, its compositions are: SiO_2, K_2O, Na_2O, MgO, B_2O_3, BaO, and Al_2O_2. The core glass constitutes 80% of the fiber volume. The refractive indices of the core and cladding are n=1.63 and n=1.48, respectively. Assuming these indices, roughly 7% of the produced scintillation light is trapped

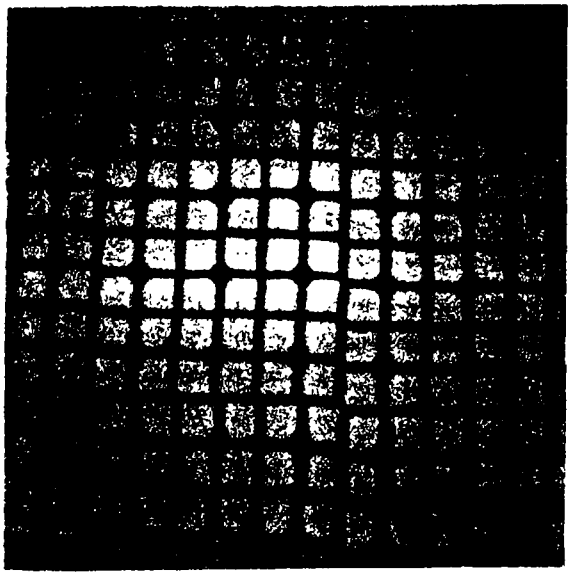

FIGURE (45)

Microscope image of fiber lattice of Tb_2O_3 scintillating glass.

within a given fiber [42, 46]. It is the purpose of the EMA to absorb the untrapped light (93% of total scintillation emission) before it can reach the detection system (the image tube).

Six of the wafers were stacked together in a solid pack, separated only by a thin layer of grease to keep holding them together, followed by two wafers on each side of the pack with a 0.5 mm plastic spacer (of the same dimensions) between each of them. The wafer assembly then was coupled directly to the fiber optics window of the image intensifier system through one of the narrow polished ends. A thin layer of silicon grease (Dow Corning 02–3067) was used in-between as optical couplant (to improve the light collecting efficiency).

The image intensifier system consists of ITT (F4145) proximity focused image tube, which has been described thoroughly in the previous chapter, and a VARO (3603–1) microchannel intensifier tube. Figure (46) shows the different parts of the VARO tube; it consists of a fiber optics input window, S20 photocathode, an electrostatic focusing lens, a microchannel plate, P36 phosphor screen, and a fiber optics output window. In the system, the output window of ITT tube is coupled directly to the input window of the VARO tube through a thin layer of silicon grease (as an optical coupler). The resolution of each tube, as quoted by the manufacturer, is 18 line pairs/mm for the ITT tube and 36 line pairs/mm for the VARO tube, which gives a total resolution for the system of 16 line pairs/mm.

To achieve maximum optimization between the first tube (ITT) phosphor screen and the second tube (VARO) photocathode, a multialkali photocathode (S20) was used on the VARO tube which has a high spectral response near the emission peak of (P20) phosphor. The two tubes combined have a total photon gain of 3×10^9 (including the optical coupling loss ~ 0.35) at maximum operating voltages. The tubes are each powered with its own power supply. A K&M 2059A gateable power supply was used to power the ITT, tube while the VARO tube has its own power

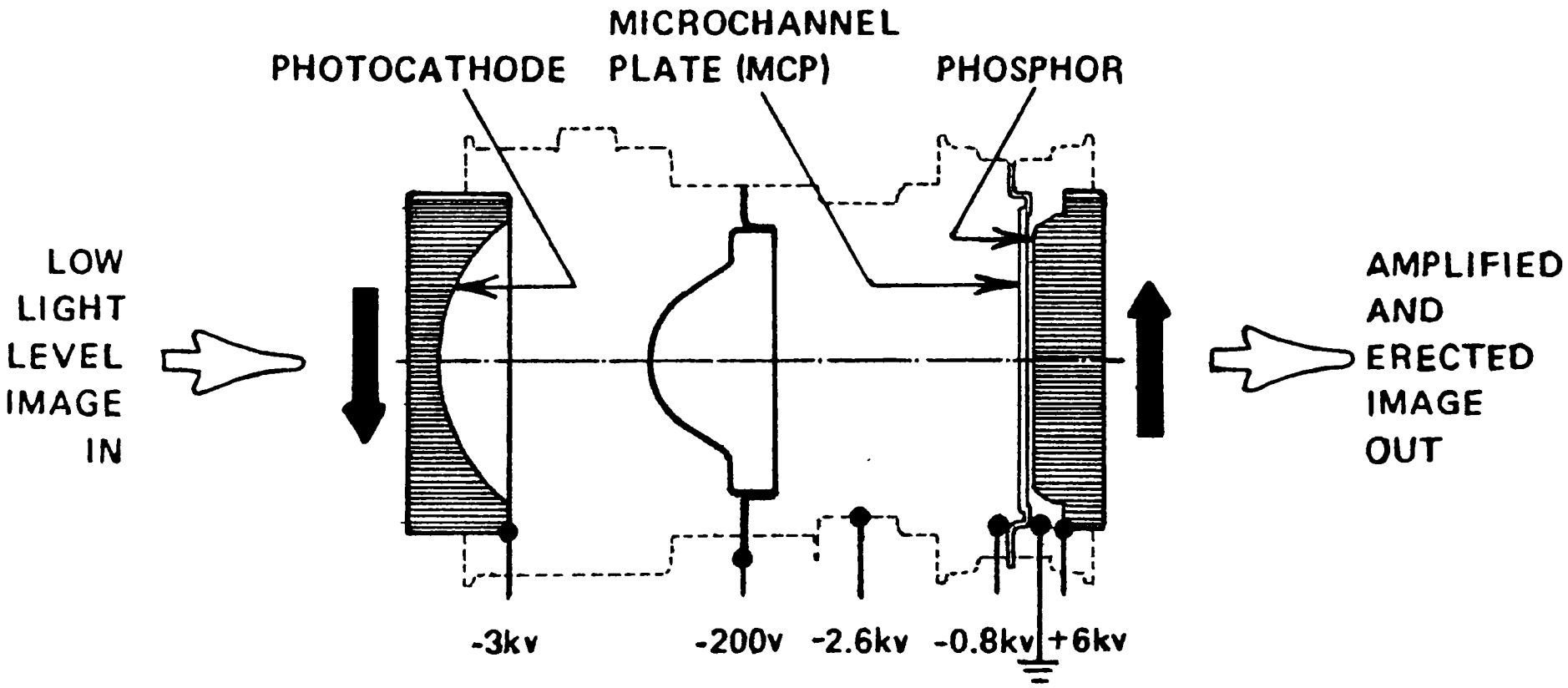

FIGURE (46)

VARO Microchannel Intensifier Tube.

supply inside the housing of the tube which requires only a 3 V battery to run it. A Sony V8 video camera was used to record the output images from the tube system. It incorporates CCD'S in its readout system which has the advantage of low-light level sensitivity and high resolution charged coupling devices. It has (256 × 256)pixels, each of 25 micron size. The collected data are recorded on 8 mm magnetic tape. All functions in the unit can be operated externally with a remote control. The complete assembly of the scintillating fiber detector is shown in figure (47).

2.4 Experimental Test

A test run at TRIUMF meson research facility (in Vancouver B.C.) was conducted between the 20–23 of February 1987, to establish:

1–The best working conditions for the detector with respect to the associated MCP's gain and coupling method.

2–The sensitivity of the system for minimum ionizing singly charged particles at different energies.

3–The minimum resolution of the detector.

The experiment was set in (M11) test area of the meson hall floor. A (π^+) beam was supplied to this area from the main beam line (A1) through two bending magnets and sets of quads. Figure (48) shows a site plan of TRIUMF and indicates the testing area where our experiment was placed. The beam was running in a continuous mode through (A1) line with total current of 5 nA. A total of four (8 hour) shifts of beam time were given to us to perform the different tests on the detector. The pion flux at the exit window was adjusted to be around 100 π^+ /sec using the vertical and horizontal sets of quads in front of the target area. The pions were supplied at three different energies, a maximum energy of 409 Mev/c,

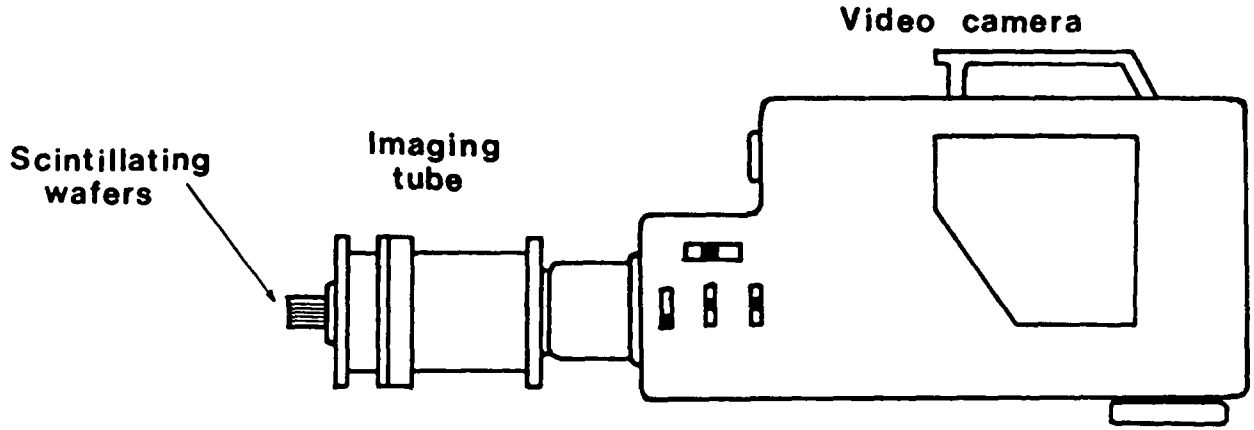

FIGURE (47)

The scintillating fiber detector assembly.

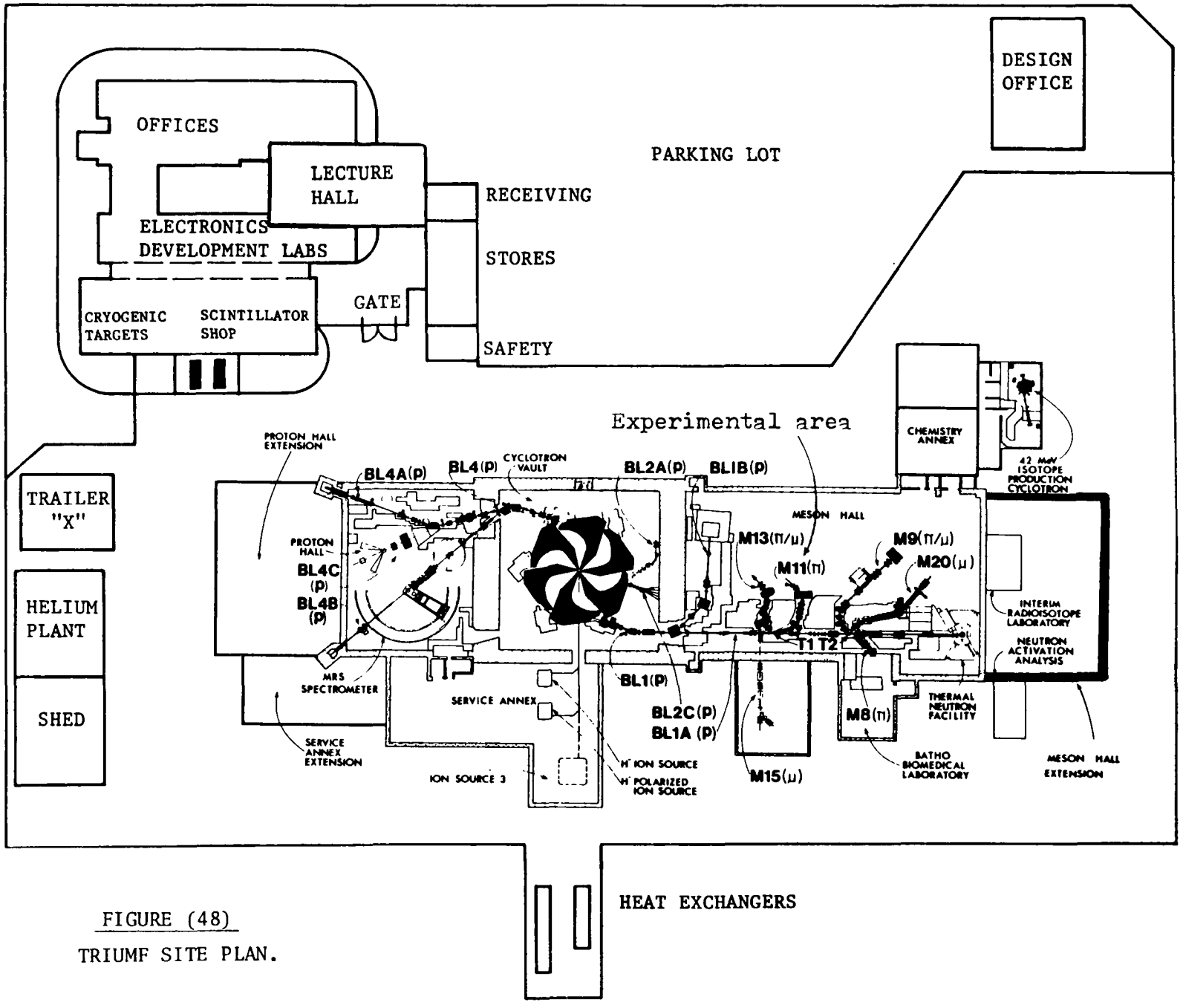

FIGURE (48)

TRIUMF SITE PLAN.

251 Mev/c, and 150 Mev/c. The beam compositions at these different energies are shown in figure (49). Most of the tests performed on the detector were done at maximum pion energy (409 Mev/c).

2.4.1 Experimental Set-up

Figure (50) shows the set-up used to test the performance of the scintillating fiber detector. It consists of four scintillating counters ($S1 - S4$) plus the tracking detector. $S1$ has an area of (3×3) cm^2, $S2$ (1×1) cm^2, $S3$ (3×3) cm^2, and $S4$ (15×15) cm^2. The four counters are made of NE102 plastic scintillator 3 mm in thickness, coupled to Philips 56AVP PMT's. All tubes were operated at 2100 V. The spacings between $S1, S2, S3$, and $S4$ were 7 cm, 50 cm and 28 cm, respectively. The tracking detector was set 5 cm behind the $S2$ counter to cover the (1.5×1.5) cm^2 sensitive area of the detector. The set-up was placed in front of the beam pipe, and all counters including the tracking detector were centered relative to the beam centre (the center of the beam pipe). The scintillating wafers were arranged in a horizontal position relative to the beam direction, in such a way that the pions will pass through the whole width of the wafers (1.5 cm). In the experiment, $S1, S3 and S4$ were used in coincidence to measure the total pion flux, while $S1, S2$ and $S3$ were used to measure the flux passing through the sensitive area of the detector. The beam spot size at the exit window was approximately 3mm in both directions, which is perfectly suitable for our testing conditions.

2.4.2 Tests and Results

1–Gain adjustment.

The initial tests involve adjusting the working conditions of the imaging system for optimum operation of the detector. This includes the setting of the total

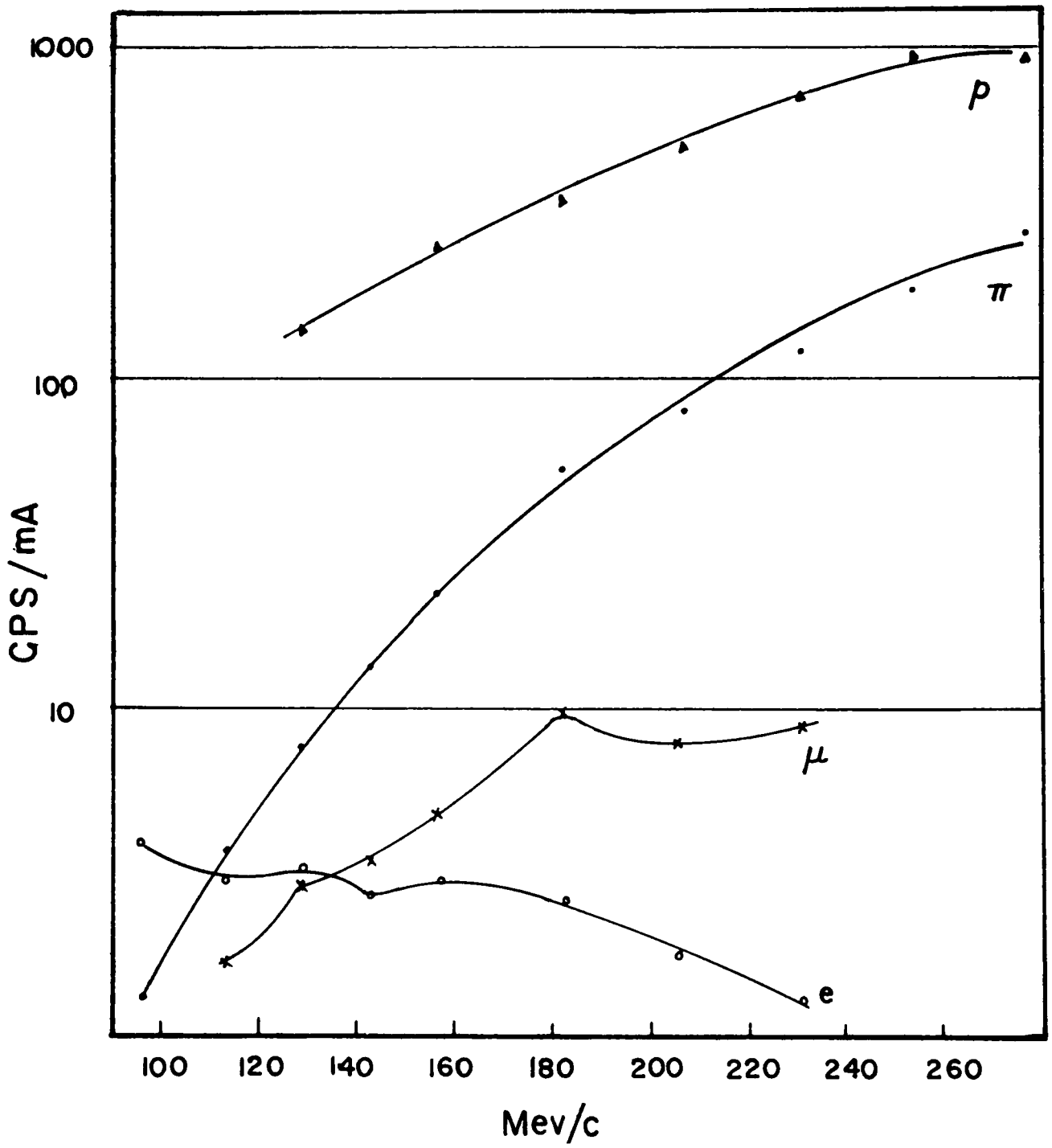

FIGURE (49)

Beam impurity at different energies for M11 test area at TRIUMF.

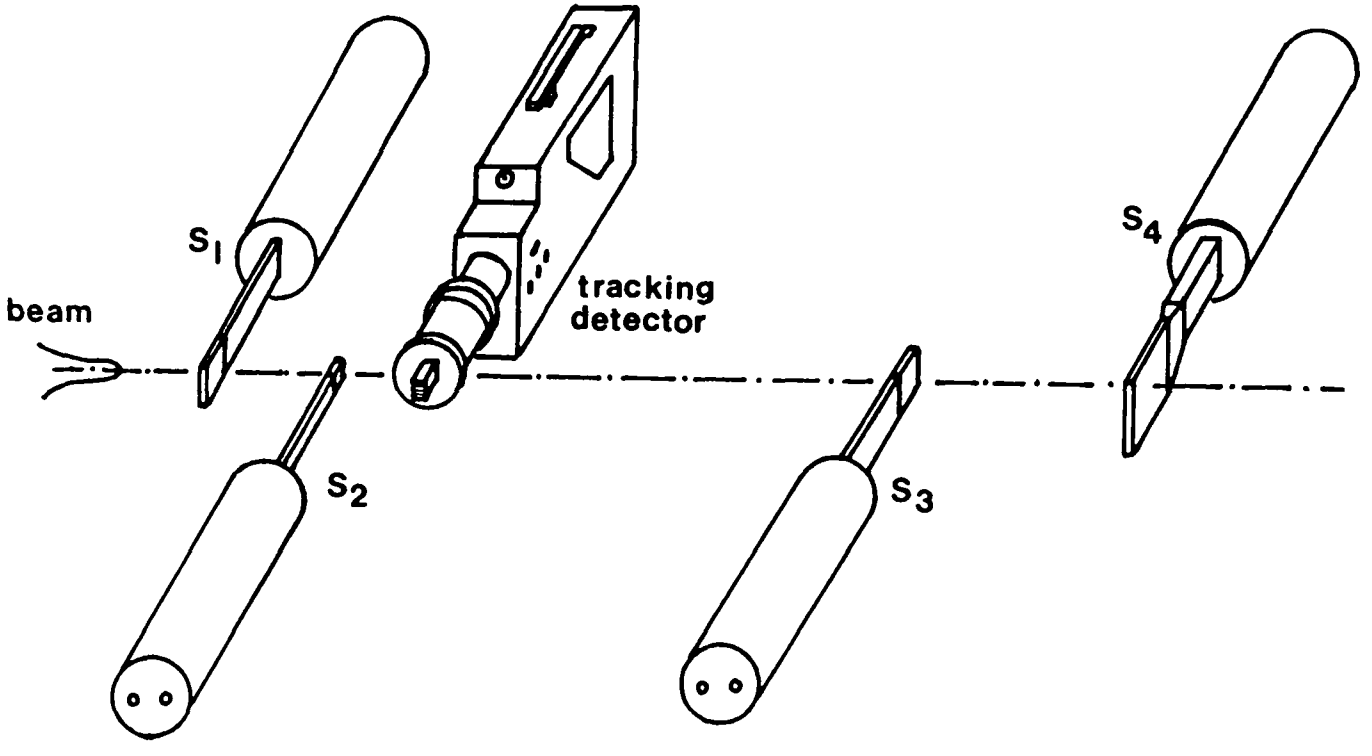

FIGURE (50)

The experimental set-up used at TRIUMF to test the scintillating fiber optics detector.

gain of both tubes (ITT and VARO) by adjusting the potential difference across the MCP and between the MCP and the phosphor screen separately in each tube. With the pion beam at maximum energy (409 Mev/c), the voltage setting on the ITT tube was varied from (1270–1325)V across the MCP which corresponds to an electron gain of (1000–2500) and from (4500–5000)V on the phosphor screen. For the VARO tube, the voltage across the MCP was kept at maximum value (800)V while the voltage between the MCP and the phosphor screen was varied between (5000–6000)V. By trying different voltage settings on both tubes, the most suitable arrangement was found to be 1270 V across the MCP and 5000 V between the MCP and the phosphor screen in the ITT mube, while keeping the voltage at maximum across the MCP in the VARO tube and 5000 V on the phosphor screen. As a result, the detector was sensitive enough to detect minimum ionizing particles and at the same time it showed a fine track resolution of 150 micron.

2–Response to Different Energies.

To establish a sensitivity of the detector to different ionizing particles and different energies, a 400 Mev/c proton beam and pion beam at energies (400, 250 and 150 Mev/c) were used. In the set-up, the scintillating wafers were arranged in a parallel position to the beam direction so that the crossing particles will show a continuous image through the full 1.5 cm width of the wafers (except at the crossing points between the wafers where a spacing gap exists). A half-hour run for each of the different beam energies was conducted and recorded for later analysis. The results show no difference in the response of the detector to the different pion energies (400, 250 and 150 Mev/c). The average hit density per crossing particle was around 20 hits/1.5 cm (1–2 hits/mm) for the pions. Protons appeared as continuous solid tracks when traversing the scintillating fibers. Figure (51) shows a cosmic ray track, a 400 Mev/c proton track and a 400 Mev/c pion track crossing

Table 3: Pion Mean Free Path

pion energy (Mev/c)	total pion flux (F)	N	λ (cm)
400	5000±250	218±15	34.40±3.14
250	5000±250	229±15	32.75±2.90
150	5000±250	106±10	70.75±7.90

the detector. Since the scintillating glass fibers contain a number of heavy elements (including terbium), they can be used as an active target for studying different beam interactions within the volume of the detector. Accordingly, the pion mean free paths (λ) at the different energies were calculated by counting the total number of pion interactions within the scintillating glass for a certain flux density. 5000 pion tracks were counted for each of the different pion energies and the total number of interactions were recorded for each case. Using the equation,

$$\lambda = \frac{FL}{N}$$

where

F—total pion flux

L—the distance travelled by the pions within the detector (1.5 cm).

N—total number of interactions.

The mean free paths were calculated and the final results are shown in table (3).

Figure (52) shows pion interactions in the scintillating glass fibers at 400 Mev/c.

2.4.3 Coupling Through a Fiber Optics Ribbon

Instead of coupling the scintillating wafers directly to the input window of the imaging tube, they were coupled through a two feet long coherent fiber optics

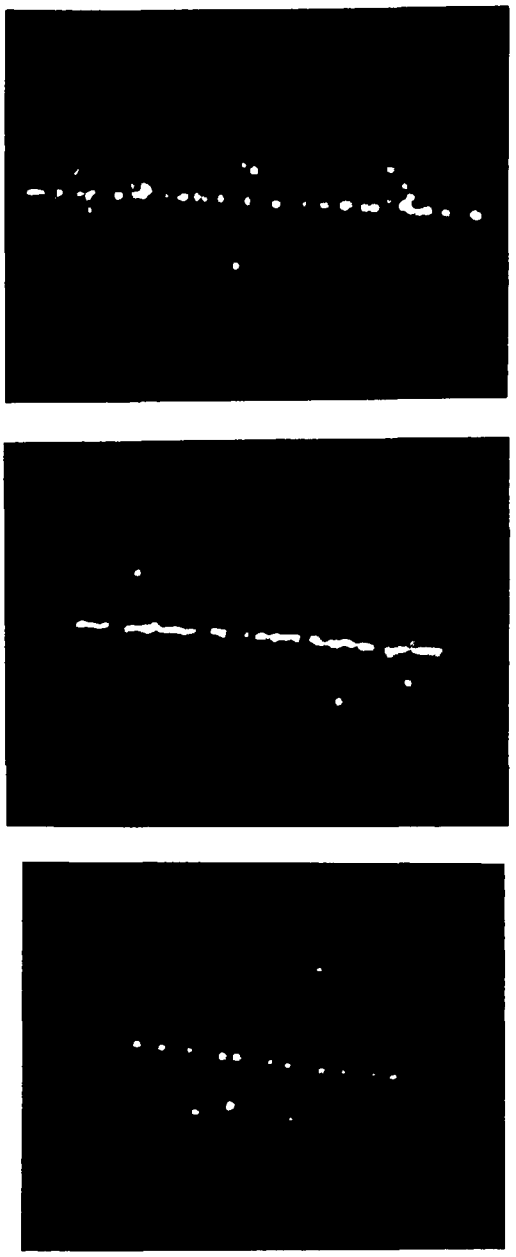

(a)- cosmic ray track

(b)- 400 Mev/c proton track .

(c)- 400 Mev/c pion track .

FIGURE (51)

Photographic image of different charged particles passing through the scintillating fiber detector .

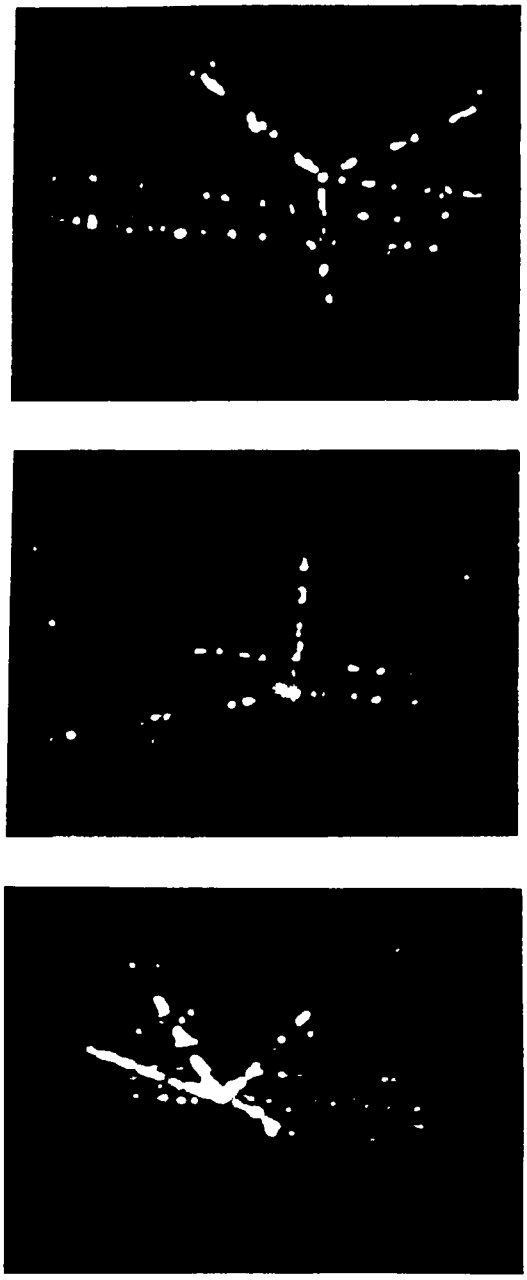

FIGURE (52)

Pion interactions at 400 Mev/c.

ribbon (previously described in chapter 1). Using the same set-up and repeating the same previous conditions, the detector was tested with 400 Mev/c pions. The recorded images show a 50% attenuation in the signal received by the imaging system. This was reflected by the number of hits recorded from the pions traversing the detector, which was around 10 hits/ 1.5 cm. Obviously, it was caused by the extra coupling through the ribbon and the insufficient trapping of the light signals in the fibers.

The ribbon was tested to ascertain the effect of scintillation light within the glass fibers caused by the traversing pion (or proton) beam. No effect was recorded except an increase (30%) in the background signals seen from the imaging tube (which is still negligible, considering the fact that the imaging tube used has a very low background signal). The imaging tube was tested for a similar effect by setting it directly in the beam. The recorded images showed a low hit density (around 13 hits/2.5 cm) for pions traversing the fiber optics window of the imaging tube. These tracks can be recognized easily from the ones generated in the scintillating fibers by its width (represented by the diameter of the face-plate of 2.5 cm), and its low hit density.

These light signals can be attributed to Cerenkov effect within the glass fibers of the input window. Figure (53) compares the light signals from a 400 Mev/c pion passing through a wafer of scintillating fiber, with and without a fiber optic ribbon.

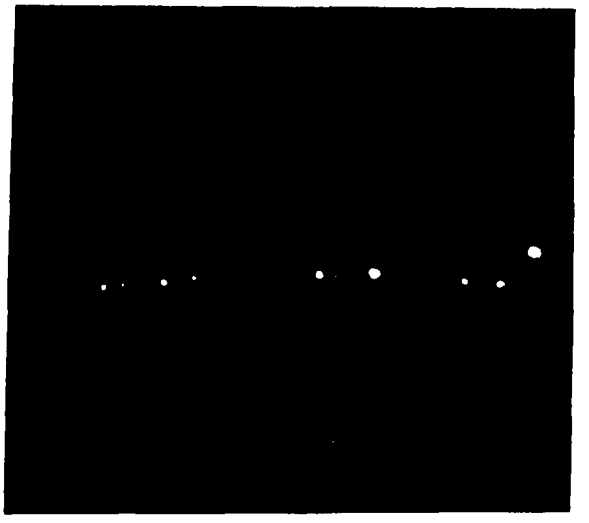

(a)

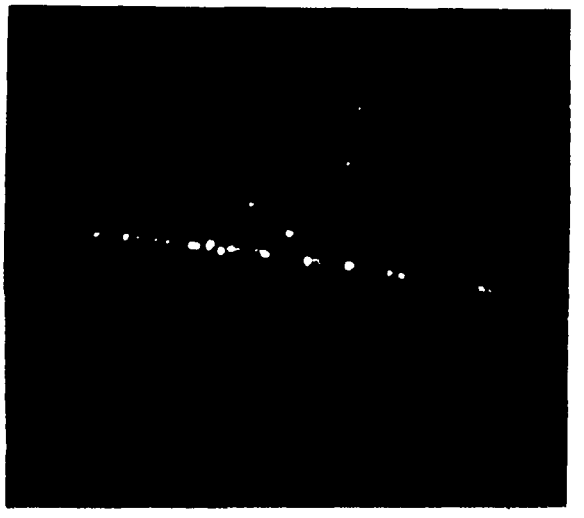

(b)

FIGURE (53)

Images of 400 Mev/c pions traversing the scintillating wafers,
a- with ribbon coupling.
b- without ribbon coupling.

Chapter 3

Detector Application to Heavy-Ion Physics

3.1 Introduction

In November 1986, Brookhaven successfully achieved the acceleration of oxygen 16 ions to 14.6 Gev per nucleon in its Alternating Gradient Synchrotron (AGS) ring. We had the opportunity to be among the few experiments which were given a running time on the beam when it started. The experiment was planned as a test run for the detector to evaluate its performance as a vertex detector within an experiment. At the same time we expected to collect enough data on the interactions of oxygen nuclei with different target materials, to estimate its cross-section, and if possible, measure the multiplicity of the secondary particles from the interactions in this range of energy. The experiment was set in the (MPS) testing area on beam line (A1), figure (54). The beam has a cycle of one pulse every 3.5 seconds with half a second pulse period and average intensity of 10^4 ions per pulse. The beam was quite divergent with the spot size of 5 cm long (in the x–direction) and 2 cm wide (in the y–direction). During the initial tuning of the beam, the detector proved to be

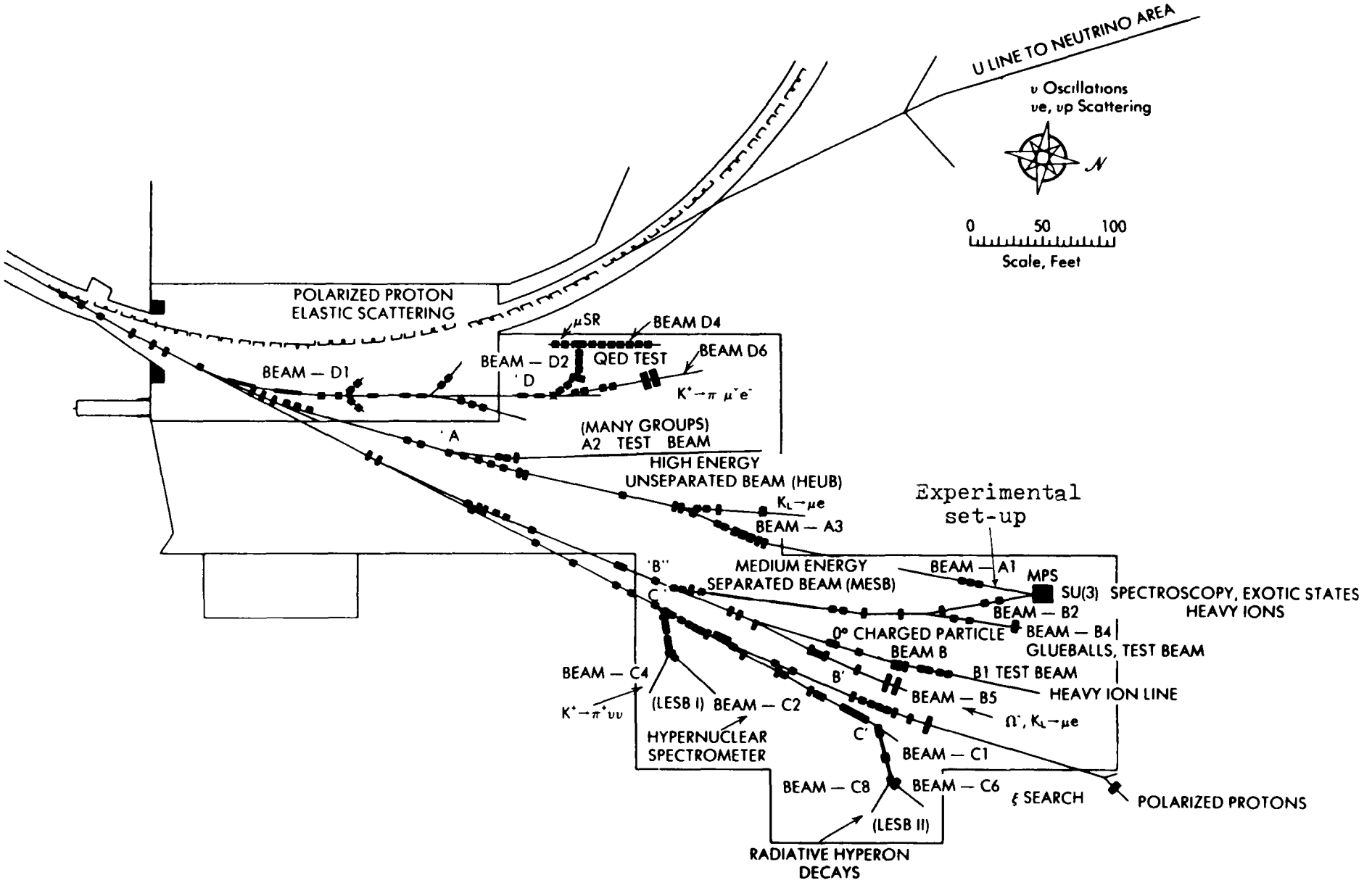

FIGURE (54)

The testing area of Brookhaven experiment.

quite useful in giving instantaneous visual information about the beam status, with respect to its divergence and purity which is of importance in focusing the beam and reducing its impurities. A total of 8 hours beam time (in parasitic mode) were used to perform the different tests on the detector. The outcome of these results are of importance, since for the first time interactions at this range of energy can be studied in the lab.

3.2 Experimental Set-up

The previously used set-up in the TRIUMF experiment was used also in this test run (figure 48). The scintillating counters $S1, S2, S3$ and $S4$ were used as a telescope for monitoring the beam intensity and recording the total flux crossing the active area of the detector.

The scintillating glass assembly (the detecting elements in the detector) consisted of two scintillating blocks (described previously in section 2.2); each has an area of $(1 \times 1) cm^2$ and is 2.5 cm long, coupled with six scintillating fiber optic wafers. Each wafer has the dimension of $(1.5 \times 0.05) cm^2$ and 2.5 cm in length. They were stacked together with brass shims of 270 microns thickness, spacing them. The blocks and the wafers were assembled together as in figure (55), and coupled to the input window of the imaging tube through one of the polished ends, via an optical coupler. In the assembly, the wafers were spaced from the two blocks by a piece of plastic of the same dimensions as the scintillating wafer. Since the intensity of the beam (at the center) was $\sim 10^4$ ions per pulse, the whole set-up was lowered by one inch below the beam center, where the intensity is low enough (few ions per pulse) to study the oxygen interactions in the detector.

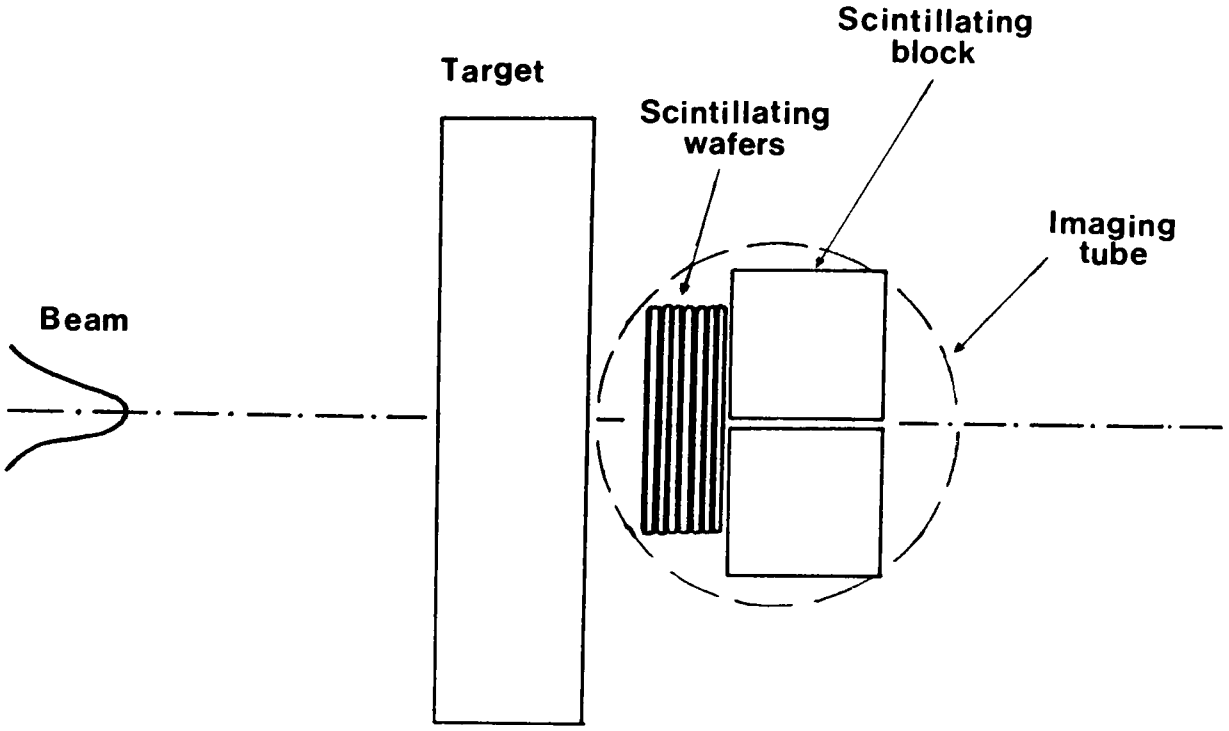

[SCALE 2:1]

FIGURE (55)

The scintillating fiber assembly.

3.3 Performance Tests

Three main tests were conducted within the given time period;

1— Gain Adjustment.

The gain of the imaging system has to be adjusted in such a way that the detector will be sensitive to both minimum ionizing particles and heavy fragments while maintaining good resolution at the same time. This was achieved (as previously described) through the adjustment of the potential differences across the MCP and the phosphor screen in both tubes, ITT and VARO. The final setting was 1375 V (electron gain of 4500e) across the MCP and 5000 V between the MCP and the phosphor screen,for ITT tube. For the VARO tube, the voltage was kept at maximum (800 V) across the MCP with 5000 V between the phosphor screen and the MCP .

2— Target Setting.

Three different target materials were used to study its interactions with the oxygen ions:

Aluminum–$(16 \times 16)mm^2 \times 13mm$,

Copper–$(17 \times 18)mm^2 \times 6.3mm$,

Iron–$(20 \times 17)mm^2 \times 6.3mm$.

Each target was set in front of the scintillating assembly covering the active area $(1.5 \times 1.5cm^2)$ of the detector, with a spacing of 5 mm from the scintillating wafers. A one hour run per target was conducted with a flux density $\sim$ 10 ions per pulse.

3— Fiber Bundle Coupling.

A new three feet long fiber optics bundle, made by Schott Fiber Optics, was coupled to one of the scintillating fiber optic blocks at one end and to the imaging tube at the other end. The ends of the bundle were epoxied in order to obtain a rectangular $(9 \times 11mm^2)$ cross–sections which were then highly polished. The fiber

optics bundle consists of 10 micron glass fibers with improved numerical aperture (N.A.) of 0.62. This enables the fibers to gather more light signals (since its acceptance angle will be larger), and improves its efficiency. The scintillating block was set in the beam direction, and a 15 minute run was recorded for comparisons with the direct coupling of the scintillating block to the tube. The results show attenuation of at least 30% in the transmitted light signals. This was probably attributable to the extra coupling through the fiber bundle rather than attenuation in the bundle itself.

3.4 Results and Analysis

3.4.1 Attenuation of the Light Signal Across the Scintillating Block

Looking through the recorded images of the oxygen ions traversing the scintillating block, one can notice clearly the difference in the track density between the crossing ions, and in the number of delta-rays associated with each track. This leads to the assumption that either the beam was not as pure as was predicted and contained a high number of lower (Z) fragments, or the intensity of the light signal from each track is a function of the location where the track crosses the scintillating block which is caused by the attenuation of the signal within the fibres itself. Studying the images more carefully, it was obvious that the second assumption is more likely the reason for the change in the light intensity between different tracks. This means that the intensity of the signals received on the imaging tube will depend primarily on the distance between the coupling point, of the fiber and the tube, and the position of the ion track. Accordingly, the ions that cross the scintillating block at points close to the tube will suffer less attenuation, and will show a dense

image. The farther from the coupling point to the tube the more the attenuation and the weaker the image. This effect can be noticed clearly when an ion crosses the block at a wide angle along its length. We can see the change in the intensity of the track and the change in the number of delta-rays as the ions pass through the block away from the imaging tube. To test this assumption, one has to tag the beam through different locations in the scintillating block, and study the relation between the intensity of the image received and the tagging location in the scintillating fiber. This was not possible, because of the difficulty of having a second run in the accelerator, and the validity of this assumption is hard to prove by any other method.

During the coupling of the scintillating wafers to the imaging tube, a few wafers were not in direct contact with the input window from one of the edge corners. There was a spacing of nearly 200 microns between the edge and the window. This caused the track images to be distorted in such a way that the light signals (from these wafers), are not in line with the center of the track. At the same time, the magnitude of deviation in these signals will depend on how far the crossing point of the ion is from the coupling edge. Accordingly, the tracks with no deviation in the wafers signal should appear dense and have a high number of delta-rays, while the tracks that show a certain deviation from the center will have a lower density and a low number of delta-rays associated with it. Looking through many different images, it was very clear that such correlations do exist, and this effect can be used to estimate the location where the ions traverse the scintillating fibers assembly. Figure (56) shows two oxygen tracks crossing the scintillating fibers at two different locations. This means that the closer the track is to the coupling edge, the less the deviation and vice-versa.

The horizontal sweep lines of the television screen were used as a reference to estimate the magnitude of deviation in the light signals from the centre of the track.

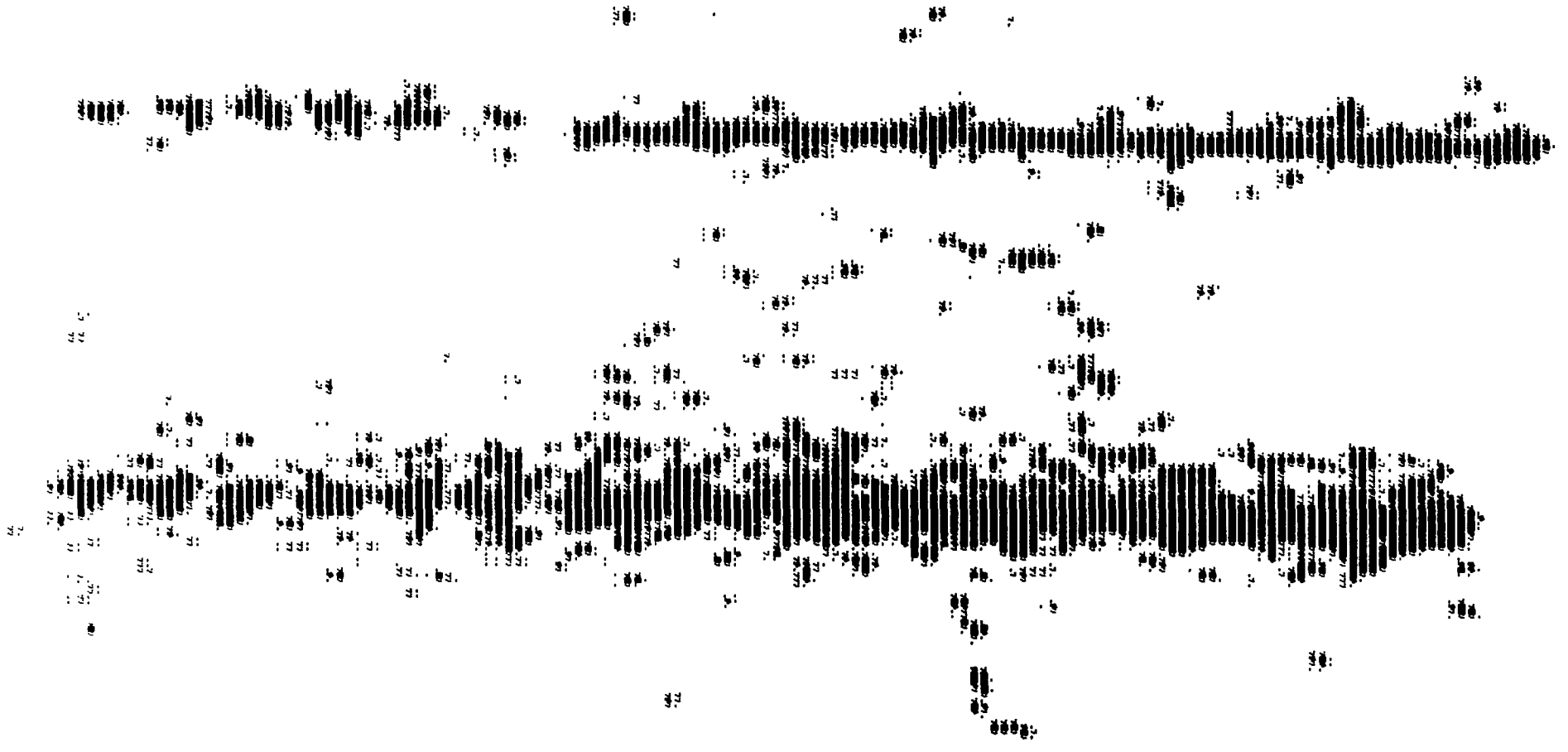

FIGURE (56)

Oxygen tracks crossing the scintillating fibers at different locations.

A 1000 oxygen tracks traversing the scintillating assembly have been scanned. For each track, the total number of delta-rays associated with the tracks were measured, and the magnitude of deviation (represented by the number of TV lines) in the wafers signals was noted.

The data was arranged in five groups relative to the number of deviated lines (from zero line to four lines of deviation). Then, each group was correlated to a segment in the scintillating assembly which represent a certain location within the scintillating fibers from the coupling edge with the tube. The 25 mm length of the scintillating assembly was divided equally into five segments representing the locations, (0–5), (5–10), (10–15), (15–20) and (20–25) mm from the coupling point. Following this arrangement, group one should include all tracks traversing the scintillating assembly between (0–5) mm from the coupling edge, and has a zero line deviation. Group two includes tracks traversing the segment (5–10) mm from the coupling edge and has a deviation of one line. The same sequence applies to the remainder of the groups. Figure (57–59) shows the distributions of the oxygen tracks relative to the number of delta-rays associated with each track for groups two, three and four respectively. As the oxygen ions traverse the assembly through segments located away from the coupling edge, their signals get weaker and the average number of observed delta-rays will decrease accordingly. This is evident from the shift in the peak location for the three groups.

From the total number of tracks that have been scanned, 4% show zero line deviation with an average number of delta-rays of 60–70, and 7% show a deviation of four lines with a delta-rays countof 30–35. This reflects the fact that the beam was fairly well centered relative to the scintillating assembly. The large drop in the count of delta-rays between the two groups indicates clearly the small attenuation length of the scintillating fibers. By considering the difference in the number of delta-ray counts between the five groups (especially group 1 and 5), the attenuation

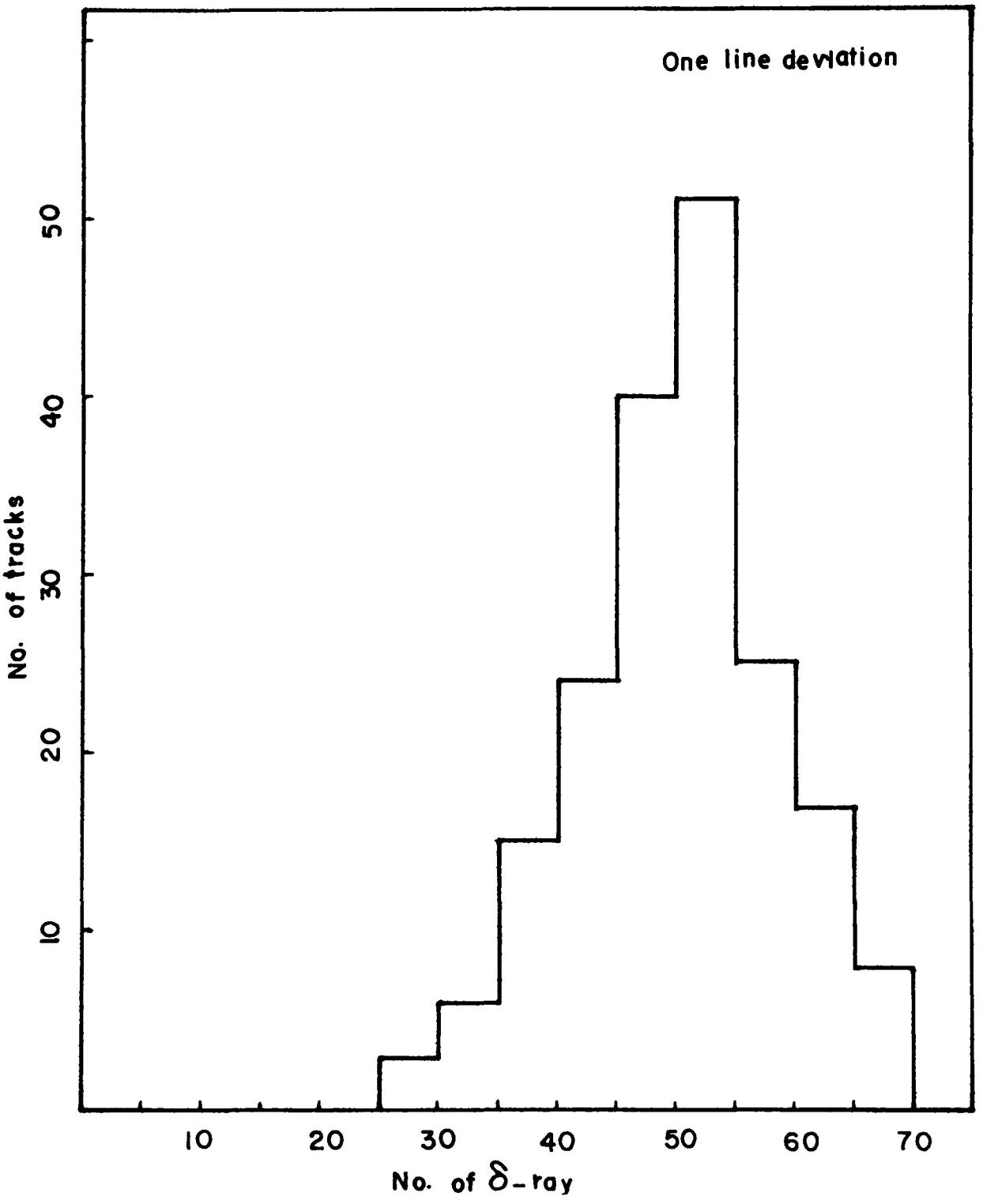

FIGURE (57)

Delta-ray distribution for tracks crossing the scintillating fibers at (5-10)cm from the coupling edge.

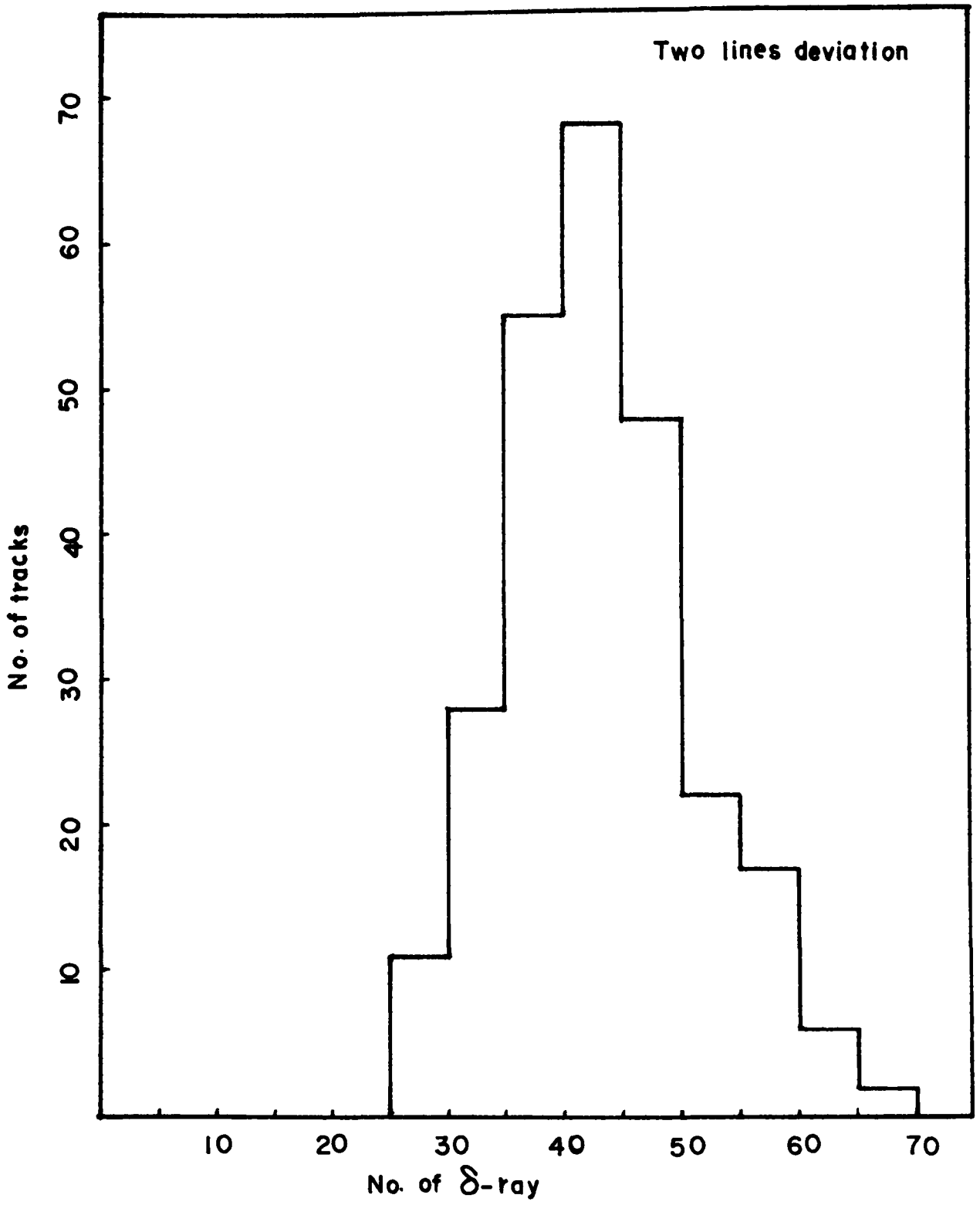

FIGURE (58)

Delta-ray distribution for tracks crossing the scintillating fibers at (10-15)cm from the coupling edge.

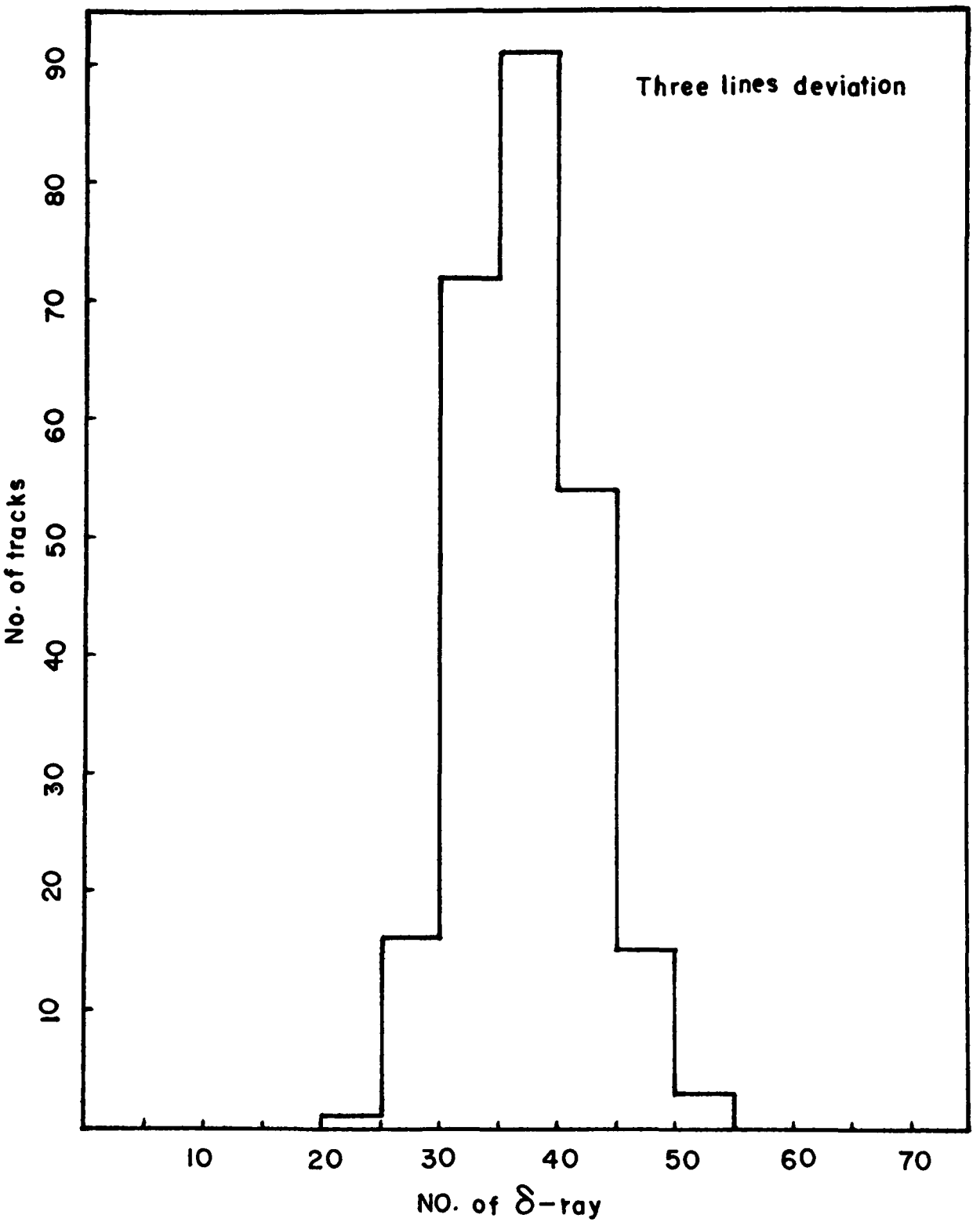

FIGURE (59)

Delta-ray distribution for tracks crossing the scintillating fibers at (15-20)cm from the coupling edge.

length of the scintillating fibers can be estimated to be around 2–3 cm. This is mainly due to the insufficient trapping of the light signals within the fibers, which is caused by the very small size of the fibers (~20 microns). The same results were found by (Atkinson *et al.*) [46] for the cerium doped glass. The shortness of the attenuation length is one of the main disadvantages that limits the use of the scintillating glass fibers in constructing particle detectors for high energy physics experiments because of the limitation that has to be applied on the size of the detector (which has to be small in this case). One definite advantage would be to use larger fibers (~50 microns in size).

3.4.2 Mean free path and cross-section measurements

The recorded images of oxygen interactions within the three targets (copper, iron, and aluminum) were scanned individually. A total of ~ 1800 O^{16}–nuclei were counted passing through each target. From the number of interactions in each target, the mean free path (λ) was measured using the formula,

$$\lambda = \frac{FT}{N}$$

where,

F–total O^{16}-flux.

T–target thickness.

N–total number of interactions.

The final results are shown in table(4).

Using these values, the interaction cross-section (σ) with each target can be calculated from the equation;

Table 4: Oxygen Mean Free Path at 14.6 Gev/nucleon.

target	total O^{16} flux (F)	N	λ (cm)
Cu	1742±41.7	137±14.9	8.01±0.89
Fe	1884±43.4	139±15.0	8.54±0.94
Al	1810±42.5	148±15.7	15.90±1.83

$$\sigma = \frac{A}{N\rho\lambda}$$

Where,

A–atomic weight.

N–Avogadro number.

ρ–target density.

λ–mean free path.

For copper, iron, and aluminum the cross-sections were 1.48 ± 0.16, 1.38 ± 0.15, and 1.04 ± 0.21 barn, respectively. Since there is no experimental data (up to date) on the interaction cross-section of O^{16}-nuclei at this range of energy, the results were compared with the predicted values calculated from Bradt and Peters [49] semi-empirical expression for the reaction cross section of beam and target nuclei, with mass number A_B and A_T, respectively, extensively tested with nuclear emulsion detectors using cosmic ray nuclei $2 \leq Z \leq 26$. The formula is;

$$\sigma_{BT} = \pi r_o^2 (A_B^{\frac{1}{3}} + A_T^{\frac{1}{3}} - \delta)^2$$

Where δ (the overlap parameter) represent the diffuseness and partial transparency of the nuclear surfaces, and r_o is a constant. Table(5) compares the results of both cross-sections (the calculated and the predicted one), and it shows a reasonable agreement between the two values within the given uncertainty.

Table 5: Oxygen Interaction Cross-Section at 14.6 Gev/nucleon.

target	σ (barn)	σ_{BP} (barn)
Cu	1.48±0.16	1.63
Fe	1.38±0.15	1.54
Al	1.04±0.21	1.14

Figure (60) show interactions of O^{16}-nuclei within the scintillating fiber detector which indicates the possibility of using the detector as an active target.

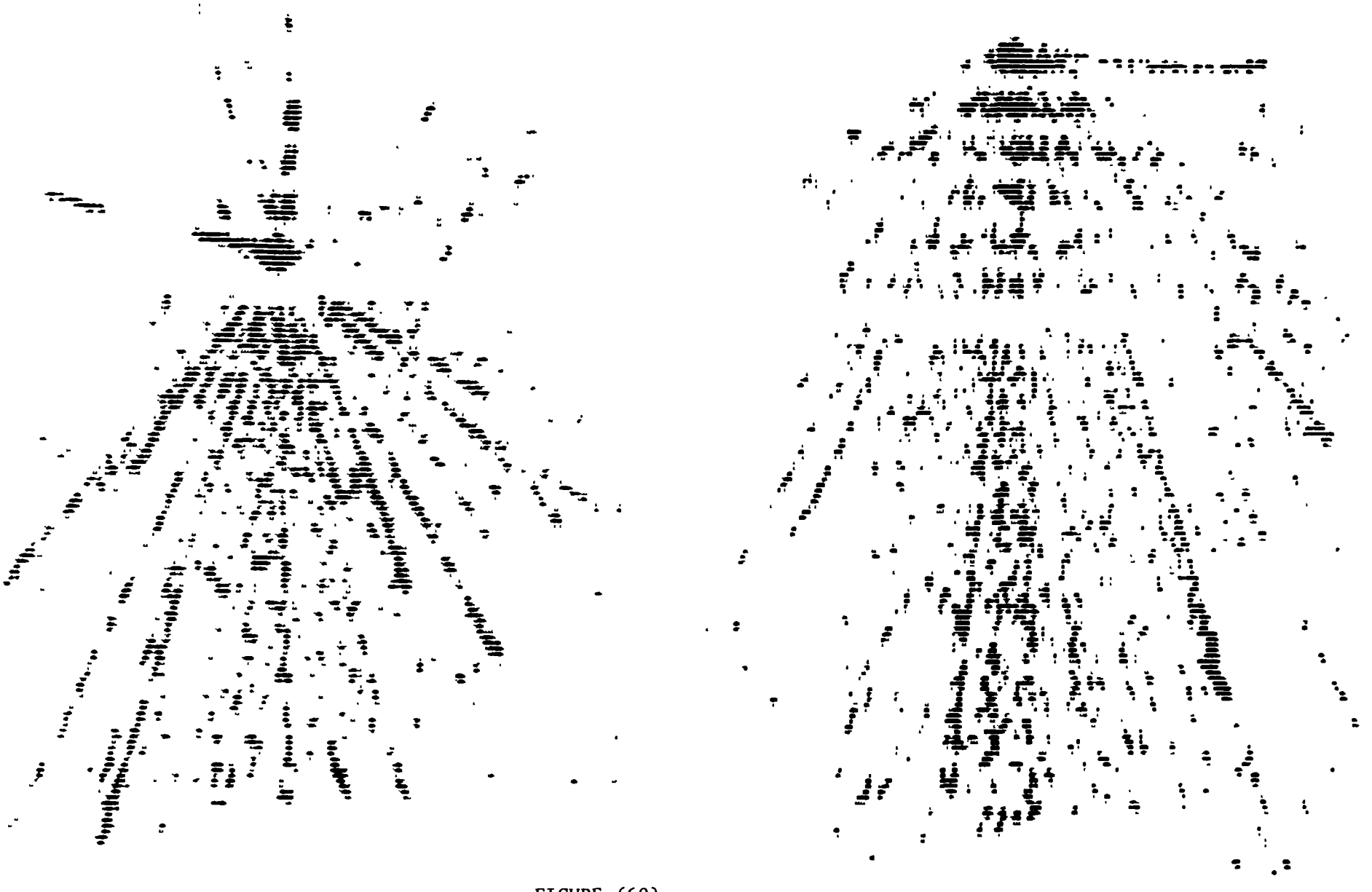

FIGURE (60)

Oxygen interactions in the scintillating detector.

Conclusion

The aim of this experimental project was to construct a vertex detector that can be associated with an emulsion (as a target) to study charm and beauty-particle decays. Although the preliminary results on the thin scintillators indicated the feasibility of using thin scintillating strips as the detecting elements in constructing a vertex detector, the experimental test-run on the first prototype (at Berkeley) with Ar^{40}-nuclei fail to establish the efficiency of the detector in constructing the secondary vertices within the emulsion target. This was mainly due to the mishap of bad coupling between the imaging tube and the coherent fiber optics ribbon. Accordingly, it was very difficult to estimate the efficiency and the resolution of the detector within normal working conditions. Also, we did not have the opportunity of testing the detector in a second experiment. From the collected data and the results of tests done with cosmic rays, the efficiency of the detector was estimated to be 50% with a maximum resolution of 200 microns, which is not feasible for studying the heavy-particle interactions.

At this point we had the choice of modifying the detector or building a second prototype that uses scintillating glass fibers as the sensitive elements. Modifying the detector involve improving the polishing of the scintillating strips and the coupling between the different parts of the detector. Also, it involves designing and building a new driving circuit for the diode arrays which were unstable most of the time during the run of the experiment. These modifications turns out to be more expensive than constructing a more compact and efficient detector that uses scintillating glass fibers as the detecting elements.

The new detector was tested at TRIUMF to establish the best working conditions and to verify its feasibility as a vertex detector. The results show a high efficiency for detecting minimum ionizing particles and a spatial resolution of 150μ.

By improving the coupling between the different parts of the detector, the resolution of the detector was improved to 100μ. In a test-run at Brookhaven National Laboratory, the detector was used to study the interactions of O^{16}-nuclei with different targets. From the recorded data, the mean free path and the interactions cross-sections were calculated for each target and found to be in agreement with the predicted value (using Bradt and Peters formula). During the experiment, the detector showed its main advantage as being a visual detector by helping in centering the beam and giving an instantaneous view of the beam status.

It was clear from the results of the experiment that the scintillating fibers suffers from short attenuation length which is mainly due to the small size of the fibers. Using larger fibers (50μ size) will improve the attenuation length by at least a factor two while keeping the same overall resolution of the detector. Also, it was apparent from the experiment that the slow decay time of the terbium glass is a limiting factor that makes the detector suitable only for fixed target experiments with low interaction rate.

It is obvious that more research is needed to improve the timing properties and the quantum efficiency of the scintillating glass to make it suitable for constructing tracking detectors that are efficient enough to be used in high rate experiments. Presently, there is some research effort going into the development of a new scintillating material called (Praseodymium) which has better quantum efficiency and shorter decay time than the cerium and terbium glass [51]. Meanwhile, the present detector is fairly suitable as a tracking system and/or vertex detector (especially with emulsion) in low interaction rate experiments. Besides that, its instantaneous visual output makes it useful for studing beam topology around accelerator facilities which gives the detector a certain commercial value.

Appendix A

Calculation of the solid angle

As cosmic rays were the main source for the high energy particles used in the different tests on thin scintillators, a calculation of the solid angle (for the set-up used) is needed to determine the count rate of the cosmic ray flux and to estimate the detection efficiency of the thin scintillators. The geometrical arrangement of the set-up was:

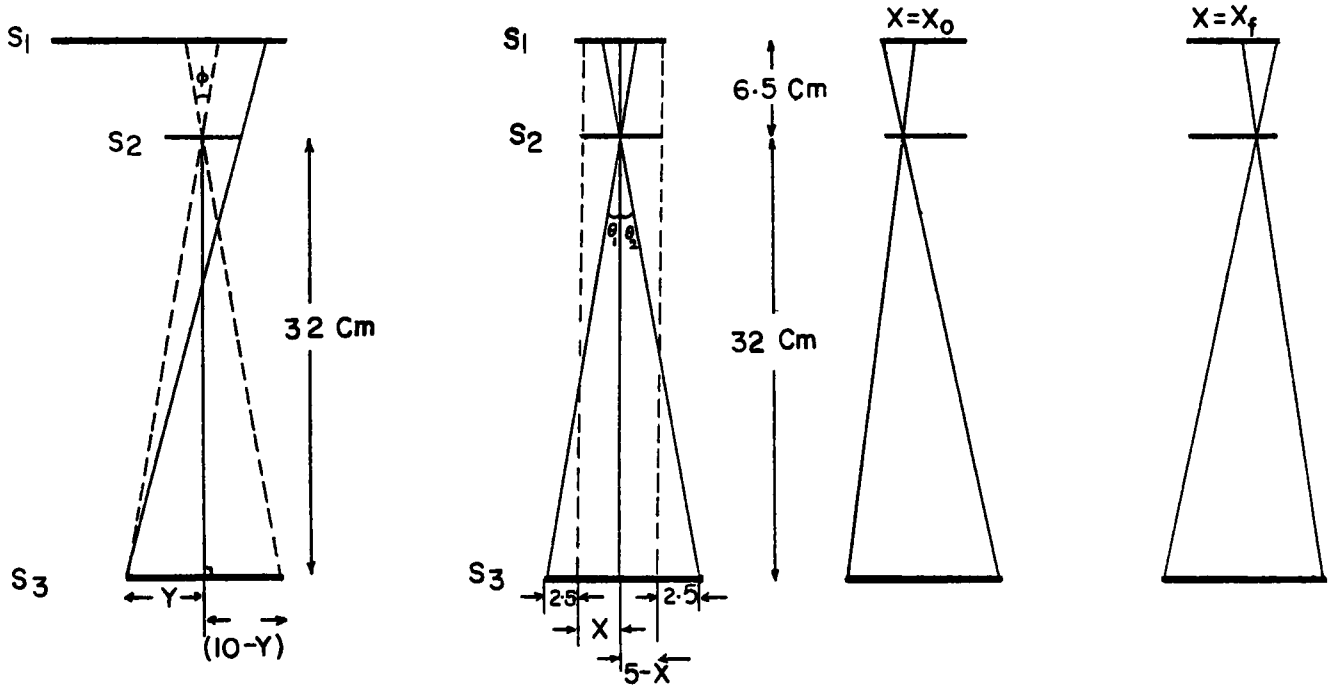

$$\phi = \tan^{-1}\left(\frac{y}{32}\right) + \tan^{-1}\left(\frac{10-y}{32}\right)$$

for $x_o \leq x \leq x_f$,

$$\Omega(x,y) = \phi(\theta_1 + \theta_2)$$

Where

$$\theta_1 = \tan^{-1}\left(\frac{2.5+x}{32}\right), \qquad \theta_2 = \tan^{-1}\left(\frac{7.5-x}{32}\right)$$

For $0 \leq x \leq x_o$,

$$\theta_1 = \tan^{-1}\left(\frac{2.5+x}{32}\right), \qquad \theta_2 = \tan^{-1}\left(\frac{x}{6.5}\right)$$

By symmetry, the contribution for ($x_f \leq x \leq 5$) is the same as that for ($0 \leq x \leq x_o$).

$$\therefore \int \Omega(x,y)\, dx\, dy = \int_0^5 \left[\tan^{-1}\left(\frac{y}{32}\right) + \tan^{-1}\left(\frac{10-y}{32}\right)\right] dy .$$

$$\left\{ \int_{x_o}^{x_f} \left[\tan^{-1}\left(\frac{2.5+x}{32}\right) + \tan^{-1}\left(\frac{7.5-x}{32}\right)\right] dx + 2\int_0^{x_o} \left[\tan^{-1}\left(\frac{2.5+x}{32}\right) + \tan^{-1}\left(\frac{x}{6.5}\right)\right] dx \right\}$$

$$x_o = \frac{6.5 \times 75}{38.5} = 1.27 \text{ Cm.}$$

$$x_f = 5 - x_o = 3.73 \text{ Cm.}$$

Let

$$\int \Omega(x,y)\,dx\,dy = A\,[\,B + 2C\,]$$

$$A = \int_0^5 \left[\tan^{-1}\left(\frac{y}{32}\right) + \tan^{-1}\left(\frac{10-y}{32}\right)\right] dy = \int_0^5 \tan^{-1}\left(\frac{y}{32}\right) dy + \int_0^5 \tan^{-1}\left(\frac{10-y}{32}\right) dy$$

as

$$\tan^{-1} x = x - \frac{1}{3}x^3 + \frac{1}{5}x^5 - \frac{1}{7}x^7 + \cdots\cdots$$

$$\therefore A = \int_0^5 \left[\left(\frac{y}{32}\right) - \frac{1}{3}\left(\frac{y}{32}\right)^3 + \frac{1}{5}\left(\frac{y}{32}\right)^5\right] dy + \int_0^5 \left[\left(\frac{10-y}{32}\right) - \frac{1}{3}\left(\frac{10-y}{32}\right)^3 + \frac{1}{5}\left(\frac{10-y}{32}\right)^5\right] dy$$

$$= \int_0^5 \left(\frac{y}{32}\right) dy - \frac{1}{3}\int_0^5 \left(\frac{y}{32}\right)^3 dy + \frac{1}{5}\int_0^5 \left(\frac{y}{32}\right)^5 dy + \int_0^5 \left(\frac{10-y}{32}\right) dy - \frac{1}{3}\int_0^5 \left(\frac{10-y}{32}\right)^3 dy + \frac{1}{5}\int_0^5 \left(\frac{10-y}{32}\right)^5 dy$$

$$A = \frac{10}{32}\int_0^5 dy - \frac{1}{3}\left(\frac{10}{32}\right)^3 \int_0^5 dy - \frac{10}{(32)^3}\int_0^5 y^2\,dy + \frac{10^2}{(32)^3}\int_0^5 y\,dy + \frac{1}{5}\left(\frac{10}{32}\right)^5 \int_0^5 dy$$
$$+ \frac{10}{(32)^5}\int_0^5 y^4\,dy - \frac{200}{(32)^5}\int_0^5 y^3\,dy + \frac{2000}{(32)^5}\int_0^5 y^2\,dy$$

$$\therefore A = 1.54$$

$$B = \int_{1.27}^{3.73} \left[\tan^{-1}\left(\frac{2.5+x}{32}\right) + \tan^{-1}\left(\frac{7.5-x}{32}\right)\right] dx = \int_{1.27}^{3.73} \tan^{-1}\left(\frac{2.5+x}{32}\right) dx + \int_{1.27}^{3.73} \tan^{-1}\left(\frac{7.5-x}{32}\right) dx$$

$$= \int \left[\frac{2.5+x}{32} - \frac{1}{3}\left(\frac{2.5+x}{32}\right)^3\right] dx + \int \left[\frac{7.5-x}{32} - \frac{1}{3}\left(\frac{7.5-x}{32}\right)^3\right] dx$$

$$= \frac{2.5}{32}\int dx - \frac{1}{3}\cdot\frac{15.625}{(32)^3}\int dx - \frac{2.5}{(32)^3}\int x^2\,dx - \frac{6.25}{(32)^3}\int x\,dx + \frac{7.5}{32}\int dx$$
$$- \frac{1}{3}\cdot\frac{421.875}{(32)^3}\int dx - \frac{7.5}{(32)^3}\int x^2\,dx + \frac{56.25}{(32)^3}\int x\,dx$$

$$\therefore \quad B = 0.741$$

$$C = \int_0^{1.27} \left[\tan^{-1}\left(\frac{2.5+X}{3.2}\right) + \tan^{-1}\left(\frac{X}{6.5}\right) \right] dX = \int_0^{1.27} \tan^{-1}\frac{2.5+X}{3.2}\, dX + \int_0^{1.27} \tan^{-1}\frac{X}{6.5}\, dX$$

$$= \int \left[\left(\frac{2.5+X}{3.2}\right) - \frac{1}{3}\left(\frac{2.5+X}{3.2}\right)^3 \right] dX + \int \left[\frac{X}{6.5} - \frac{1}{3}\left(\frac{X}{6.5}\right)^3 \right] dX$$

$$= \int_0^{1.27} \frac{2.5+X}{3.2}\, dX - \frac{1}{3}\int_0^{1.27} \left(\frac{2.5+X}{3.2}\right)^3 dX + \int_0^{1.27} \frac{X}{6.5}\, dX - \frac{1}{3}\int_0^{1.27} \left(\frac{X}{6.5}\right)^3 dX$$

$$\therefore \quad C = 0.247$$

$$\int \Omega\,(x, y)\, dx\, dy = 1.54 \left[0.741 + 2(0.247) \right]$$

$$= 1.9 \text{ cm}^2.\text{Sr}$$

As the vertical component of the cosmic ray flux crossing a horizontal area $= 1.8 \times 10^{-2}$ $\text{sec}^{-1}.\text{cm}^{-2}.\text{Sr}^{-1}$

The 100% efficiency $= 1.9 \times 1.8 \times 10^{-2} \times 3.6 \times 10^{3}$

$\simeq$ 123 counts/hour.

Appendix B

Gain and Noise Measurement of the MCP Device

A - GAIN MODEL MEASUREMENT

The photon gain by the channel intensifier tube (CIT)

$$A(\lambda_1, \lambda_2) = T_1(\lambda_1).S(\lambda_1).\ G(V_2).(V_3 - V_d).\ \int\ P(\lambda_2)\ d\ \lambda_2.\ T_2(\lambda_2)$$

where $T_1(\lambda_1)$ - transmission loss of the input window at (λ_1 = 425 nm)

$\simeq 0.55$

$S(\lambda_1)$ - sensitivity of the photocathode at (λ_1 = 425 nm)

$\simeq 70 \times 10^{-3}$ A/W for bialkali (K-cs-sb) photocathode.

$$= 70 \times 10^{-3}\ \frac{C}{J} \times \frac{1\text{-}24 \times 10^{-6}}{425 \times 10^{-9}} \times 1.6 \times 10^{-19}\ \frac{J}{eV} \times \frac{1\ e}{1.6 \times 10^{-19}\ C}$$

$$= 0.21\ \ e/photon$$

$G(V_2)$ - gain of the (VMCP) as a function of the applied voltage (V_2).

$$\simeq \left(\frac{V_2}{710}\right)^{16} = \left(\frac{1500}{710}\right)^{16}$$

$$= 1 \times 10^5$$

V_3 - microchannel plate to phosphor voltage

$\simeq$ 6000 V

V_d - phosphor screen dead voltage $\simeq$ 3000 V

$\int P(\lambda_2)\, d\lambda_2$ - sensitivity of the phosphor at (λ_2)

$\simeq$ 0.06 photon/eV

$T_2(\lambda_2)$ - transmission factor of the output window at $(\lambda_2 = 650)$

$\simeq$ 0.55 (for 5 mm thick fiber optics output window).

$$A(425, 650) = 0.55 \times 0.21 \frac{e}{\text{photon}} \times (1 \times 10^5) \times (6000 - 3000)\text{V} \times 0.06 \frac{\text{photon}}{\text{eV}}$$

$$\times 0.55$$

$$\simeq 1 \times 10^6 \ \frac{\text{photon out } (\lambda = 650 \text{ nm})}{\text{photon in } (\lambda = 425 \text{ nm})}$$

The total gain of the channel intensifier tube with the self-scanned array is given by the total charge stored in a single pixel of the (SSA) which is equal to,

$$Q = A(\lambda_2) \cdot S_2(\lambda_2) \cdot T_3 \cdot T_4$$

where

$A(\lambda_2)$ - the total photon gain by the (CIT) at $(\lambda = 650$ nm)

$\simeq 1 \times 10^6$

$S_2(\lambda_2)$ - absolute sensitivity of the SSA at $(\lambda_2 = 650$ nm)

$= 0.3752$ A/W

$$= 0.3752 \frac{C}{J} \times \frac{1.24 \times 10^{-6} \text{ eV.m}}{650 \times 10^{-9} \text{ m.photon}} \times 1.6 \times 10^{-19} \frac{J}{eV} \times \frac{1 \text{ e}}{1.6 \times 10^{-19}}$$

$$= 0.716 \frac{e}{\text{photon}}$$

T_3 - tube to SSA coupling loss = 0.8

T_4 - the transmission loss by the SSA fiber optics coupler = 0.8

$$Q = 1 \times 10^6 \frac{\text{photon}(\lambda_2)}{\text{photon}(\lambda_1)} \times 0.716 \frac{e}{\text{photon}} \times 0.8 \times 0.8$$

$$= 4.58 \times 10^5 \quad e/\text{photon} \ (\lambda = 425)$$

For NE102 plastic scintillator, the energy loss by a minimum ionizing particle is 2.5 MeV/1 cm or 25 keV/100 micron.

$$E_\gamma = \frac{hc}{\lambda} = \frac{6.625 \times 10^{-27} \text{ erg. sec} \times 2.997 \times 10^{10} \text{ cm/sec}}{425 \times 10^{-7} \text{ cm}}$$

$$= 4.67 \times 10^{-12} \text{ erg}$$

$$= 4.67 \times 10^{-12} \times 6.24 \times 10^{11} \text{ eV}$$

$$= 2.9 \text{ eV} \quad \text{at } (\lambda = 425 \text{ nm})$$

As only 2% of the energy loss is converted to fluorescence,

$$\text{the number of photons emitted per (100)micron} = \frac{25 \times 10^3 \text{ eV} \times 0.02}{2.9 \text{ eV}}$$

$$= 172 \text{ photons}$$

The minimum thickness needed to get 100% efficiency is 250 micron,

the number of photons emitted (per 250 μ) = 430 photons

Assuming that only 10% of the total number of photons will reach the collecting edge of the scintillator plus a 50% loss across the fiber optics ribbon,

the number of photons reaches the input window of the (CIT) per a single scintillator strip $\simeq$ 21 photon

the total charge stored in a single pixel of SSA is,

$$Q = 4.58 \times 10^5 \ \frac{e}{(\text{photon } \lambda = 425)} \times 21 \ (\text{photon } \lambda = 425)$$

$$= 9.6 \times 10^6 \text{ electrons}$$

$$= 9.6 \times 10^6 \times 1.602 \times 10^{-19} \text{ C}$$

$$= 1.54 \text{ picocoulomb}$$

The saturation charge (Q_{sat}) of the wide aperture linear self-scanned array (EC/17) with an area of (430 micron x 50 micron) is

$$Q_{sat} = 3.2 \text{ picocoulombs}$$

$$= 2 \times 10^7 \text{ electrons}$$

B - NOISE MEASUREMENT

The noise per unit area of the channel intensifier tube is given by the equation,

$$N_{(T)} = (I_e + I_m).\ G(V_2).\ (V_3 - V_d).\ P(\lambda_2).\ T_2(\lambda_2)$$

where

$I_c(t)$ - the number of electrons emitted from the photocathode per second per cm^2 at temperature (t)

$= 2 \times 10^3 \ \frac{e}{\text{sec. cm}^2}$ for bialkali at ($t = 23^oC$)

N.B. (I_c) goes down by a factor (10) for every 15^oC lowering .

$I_m(t)$ - equivalent input noise current per cm^2 of the microchannel plate at an applied voltage (V_2)

$$I_m(V_2) \simeq 10\% \text{ of } (I_c)$$

$$= 2 \times 10^2 \text{ e/sec.cm}^2$$

$$N(23^oC) = \frac{(I_c(t) + I_m(V_2)}{T_{1(\lambda_1)} \times S_{(\lambda_1)}} \times A_{(\lambda_1, \lambda_2)}$$

$$= \frac{(2 \times 10^3 + 2 \times 10^2) \text{ e/sec.cm}^2}{0.55 \times 0.21 \text{ e/photon } (\lambda_1)} \times 4.58 \times 10^5 \frac{\text{photons } (\lambda_2)}{\text{photons } (\lambda_1)}$$

$$= 8.7 \times 10^9 \text{ photons/sec.cm}^2$$

If the device is read out at intervals of (1 ms),

the noise per readout = 8.7×10^6 photons/cm^2.read

As the area of the readout pixel is (430 x 25) micron square,

the noise per readout per pixel = $8.7 \times 10^6 \times 1.07 \times 10^{-4} \frac{\text{cm}^2}{\text{pixel}}$

$\simeq 9.3 \times 10^2$ photons/pixel.read

The typical sensitivity of a pixel is $\simeq$ 0.5 e/photon

the noise per readout per pixel = $9.3 \times 10^2 \times 0.5$ e/pixel.read

$= 4.65 \times 10^2$ e/pixel.readout

As the saturation level of one (430 micron x 25 micron) pixel is,

$$Q_{sat} = 3.2 \text{ pcoul} = 2 \times 10^7 \text{ electrons}$$

thus the image intensifier noise is insignificant as the noise level of the photodiode pixel will dominate.

At a readout interval of (1 ms), the photodiode pixel noise is 5% of the saturation charge,

$$2 \times 10^7 \times 0.05 = 1 \times 10^6 \text{ e/pixel.readout}$$

$$= 1 \times 10^6 \times 1.6 \times 10^{-19}$$

$$= 1.6 \times 10^{-13} \text{ coulomb}$$

$$= 0.16 \text{ picocoulomb}$$

Appendix C

Faceplate Mounting Technique

To cut costs and save on purchasing photodiodes with fiber optics windows, they were purchased with plain unattached windows. Special fiber optics faceplates were designed (within the requirements of the manufacturing company) and fabricated by Schott Fiber Optics. The size of each faceplate is $(19.3 \times 5.4 \times 3.2)mm^3$ with a central step of $(13.8 \times 1 \times 0.56)mm^3$, consist of small fibers each of 5 microns in diameter (figure 60). The face of the stepped part and the viewing face of the window are very finely polished with a minimal number of damaged fibers. The windows were sealed on the diodes with Ablefilm 517A adhesive manufactured by Ablestick Laboratories [50]. It is a glass cloth supported tack-free epoxy film with a rectangular dye-cut of $(19.3 \times 5.4 \times 0.15)mm^3$ and $0.8mm$ width which has to be cured at a certain temperature and for a certain period of time. The film reaches a minimum (after curing) of 50 microns (depending on the applied pressure). The main requirement specified by the manufacturer (EG&G Reticon) in mounting the fiber optics window on the diodes was that the face of the stepped part of the window (which covers the sensitive area of the diodes) has to be within 25 microns from the diode sensors to maintain the required resolution.

The depth of the stepped part in the 16 windows was not as specified in our

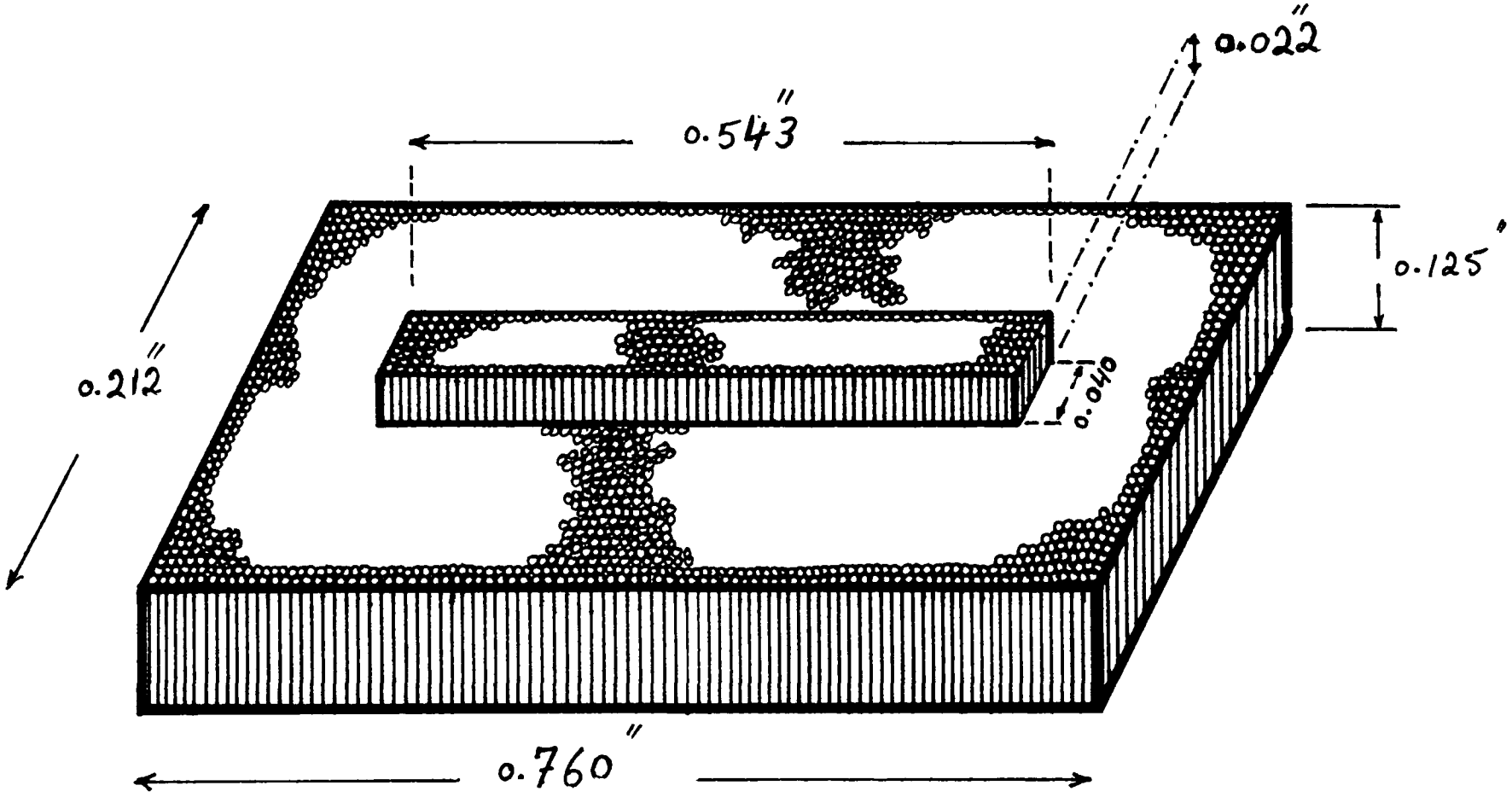

FIGURE (61)

The design of the fiber optic faceplate mounted on the diode array.

design, a difference of (25–75) microns existed within the different windows. To overcome this problem, a correction factor had to be used to achieve the 25 microns limit on the depth. This was done by controlling the cured thickness of the ablefilm using different applied pressures. In some cases where the stepped depth is quite long, a double film was used; the applied pressure was accomplished by using weights of 20–100 grams on top of the faceplates. Different tests were carried out to find the relation between the applied weight and the final thickness of the ablefilm after curing. From these tests, using the weight of the window itself reduces the thickness of the ablefilm to ~100 microns, and weights between (50–100) grams would reduce the thickness to (75–50) microns respectively. Accordingly, a certain weight was chosen for each window depending on the depth of the stepped part and how much it deviates from the required value. The windows were cured at $165°F$ over three hours period to protect the electronic circuits of the diodes from being damaged. A Dow Corning (02-3067) silicon grease was used as an optical couplant, filling the gap between the polished face of the stepped part and the diode sensors.

All 16 windows were mounted successfully on the diodes with no damage to the silicon sensors and no occurance of air-bubbles within the optical grease.

References

1. See, for example, the review by C.W. Fabian and H.G. Fischer, Rep. Prog. Phys. 43(1980)1003; K. Kleinknecht, Phys. Rep. 84,No.2(1982)85.
2. S.R. Amendolia et al. Nucl. Inst. Meth. 176(1980)457.
3. E.H.M. Heijne et al. Nucl. Inst. and Meth. 178(1980)331.
4. J.B.A. England et al. Nucl. Inst. and Meth. 185(1981)43.
5. E. Sakai, Nucl. Inst. and Meth. 196(1982)121.
6. M.L. Muga et al. Nucl. Inst. and Meth. 83(1970)135.
7. M.L. Muga, Nucl. Inst. and Meth. 95(1971)349.
8. T. Batch and M. Moszynski, Nucl. Inst. and Meth. 125(1975)231.
9. G.G. Kelly et al. Nukleonics 14,No.4(1956)53.
10. J.R. Prescott and P.S. Takhar, IEEE Trans. Nucl. Sci. NS-9,No.3(1962)36.
11. C.K. Gelbke, K.D. Hildebrand and R. Bock, Nucl. Inst. Meth. 95(1971)397.
12. M.L. Muga and G. Griffith, Nucl. Inst. and Meth. 109(1973)289.
13. R. Bren and G.D. Sprouse, Nucl. Inst. and Meth. 115(1974)57.
14. W.J. McDonald et al. Nucl. Inst. and Meth. 115(1974)185.
15. P.B. Lyons and J. Stevens, Nucl. Inst. and Meth. 114(1974)313.
16. T. Batch and M. Moszynski, Nucl. Inst. and Meth. 123(1975)341.
17. M.L. Muga and J.D. Bridges, Nucl. Inst. and Meth. 134(1976)143.

18. H. Geissel et al. Nucl. Inst. and Meth. 144(1977)465.

19. Schott Fiber Optics, 122 Charlton st. Southbridge, MA 01550.

20. C.E. Catchpole and C.B. Johnson, Publication of the Astro. Soc. of the Pacific 84(1972)134.

21. G. R. Riegler and K.A. More, IEEE Trans. Nucl. Sci. NS-20(1973)102.

22. G. Timothy, Appl. Opt. 14(1975)1632.

23. G.T. Reynolds and P.E. Condon, Rev. Sci. Inst. 28(1957)1098.

24. R.J. Ginther and J.H. Schulman, IRE Trans. Nucl. Sci. NS-5(1958)92.

25. D.G. Anderson, J. Dracass and T.P. Flanagan, Proc. 5th Int. Instruments and Measurements Conf. Stockholm (1960)616.

26. L.W. Jones and M.L. Perl, Int. conf. on high energy accelerators and instrumentation, CERN(1959)561.

27. R.J. Potter and R.E. Hopkins, IRE Trans. NS-7(1960)150.

28. M.L. Perl and L.W. Jones, Nucleonics 18(1960)92.

29. L. Reiffel and N.S. Kappany, Rev. Sci. Inst. 31(1960)1136.

30. L.W. Jones and M.L. Perl, Nucl. Inst. and Meth. 10(1961)348.

31. W.R. Binns et al. Nucl. Inst. and Meth. A251(1986)402.

32. W.R. Binns, M.H. Isreal and J. Klarmann, Nucl. Inst. and Meth. 216(1983)348.

33. W.R. Binns, M.H. Isreal and J. Klarmann, Proc. of 18th Int. cosmic ray conf. Bangalore, 8(1983)89.

34. W.R. Binns, M.H. Isreal and J. Klarmann, Proc. of 19th Int. cosmic ray conf. La Jolla, 3(1985)272.

35. H. Blumenfeld, M. Bourdinaud and J.C. Thevenin, IEEE Trans. Nucl. Sci. NS-33(1986)54.

36. H. Blumenfeld et al. Nucl. Inst. and Meth. A257(1987)603.

37. S.R. Borenstein, R.B. Palmar and R.C. Strand, IEEE Trans. Nucl. Sci. NS-28(1981)458.

38. J.M. Gaillard et al. (UA2 collaboration), Proc. DPF conf. Eugene, Oregon(1985).

39. A. Konaka et al. Nucl. Inst. and Meth. A256(1987)70.

40. L.R. Allemand et al. Nucl. Inst. and Meth. 225(1984)522.

41. H. Burmeister et al. Nucl. Inst. and Meth. 225(1984)530.

42. R. Ruchti et al. IEEE Trans. Nucl. Sci. NS-32(1985)590.

43. R. Ruchti et al. IEEE Trans. Nucl. Sci. NS-33(1986)151.

44. R. Ruchti et al. IEEE Trans. Nucl. Sci. NS-34(1987)544.

45. A. Bross, Nucl. Inst. and Meth. A247(1986)319.

46. M. Atkinson et al. Nucl. Inst. and Meth. A254(1987)500.

47. R. Ruchti et al. IEEE Trans. Nucl. Sci. NS-30(1983)40.

48. R. Ruchti et al. IEEE Trans. Nucl. Sci. NS-31(1984)69.

49. H.L. Bradt and B. Peters, Phys. Rev. 77(1950)54.

50. Ablestick Laboratories, 833 west 182nd st. Gardena, CL. 90248.

51. A. Rogers and B. Kinchen, IEEE trans. Nucl. Sci.NS-34(1987)541.